

Stigmatic and Astigmatic Gaussian Beams in Fundamental Mode

—

Impact of Beam Model Choice on Interferometric Pathlength Signal Estimates

Von der Fakultät für Mathematik und Physik
der Gottfried Wilhelm Leibniz Universität Hannover
zur Erlangung des Grades

Doktorin der Naturwissenschaften
– Dr. rer. nat. –

genehmigte Dissertation
von

Dipl.-Math. Evgenia Kochkina

geboren am 10. Mai 1987 in Voronezh, UdSSR

2013

Referent: Prof. Karsten Danzmann (Leibniz Universität Hannover)
Korreferent: Dr. Andreas Freise (University of Birmingham)
Tag der Promotion: 3. Juli 2013

Abstract

In precision interferometry, the cross coupling of angular beam jitter into the path-length readout can be an important effect. One possibility to minimize the resulting noise is to use imaging optics systems. The simplest imaging optics system that can be used for this purpose consists of two spherical lenses. In the process of investigating such systems it was found that they can transform Gaussian beams in fundamental mode from stigmatic into simple and even general astigmatic. Effectively, it means that, for instance, the spot shape of a Gaussian beam can change from circular (stigmatic) to elliptical (astigmatic) after transmission through a lens system, and the spot ellipse might even rotate (general astigmatic) along the beam path.

This thesis provides a study of the stigmatic, simple astigmatic and general astigmatic models of a Gaussian beam in fundamental mode. Each model is suitable for the procedure of simulating interferometer signals, which is also described in this thesis. The most general, and thus the most accurate model of a Gaussian beam in fundamental mode is the general astigmatic beam model. However, this model is also the most complex, and to the author's knowledge the least discussed in literature. The general astigmatic model presented in this thesis comprises the previously available information from different sources, together with a derivation of the equations that allow beam transformation at a surface.

In order to prove reliability of the general astigmatic beam model an experimental verification has been performed. Within this verification the evolution of the intensity ellipse of a general astigmatic beam has been studied. This general astigmatic beam was obtained by transmitting a simple astigmatic beam through an optical system consisting of two cylindrical lenses, both experimentally and in a simulation. The results obtained were compared and showed very good agreement.

In this thesis the impact of the beam model choice on the pathlength readout has been studied using the designs of imaging optics systems for the test mass interferometer in a LISA-like mission. In order to estimate the impact of the use of simplified beam models, a set of realistically misaligned setups was analyzed, and the results obtained with different models were compared. This investigation has shown that within the current measurement uncertainties of the parameters of the lens system, and of the initial beams, the choice of model does not affect the range of the possible cross

coupling. However, for each particular misaligned two lens system with well-known parameters the results obtained with the different models can vary considerably.

Keywords: interferometry, Gaussian beams, general astigmatism

Kurzzusammenfassung

In Präzisionsinterferometern kann die Kreuzkopplung von Laserstrahl-Winkelrauschen in das Pfadlängensignal ein wichtiger Effekt sein. Eine Möglichkeit, um das resultierende Rauschen zu minimieren, ist, optische Abbildungssysteme zu verwenden. Das einfachste System für einen solchen Zweck besteht aus zwei sphärischen Linsen. Im Laufe der Untersuchungen solcher Abbildungssysteme stellte sich heraus, dass diese Systeme Gauß-Strahlen in fundamentaler Mode von stigmatisch zu einfach astigmatisch und sogar allgemein astigmatisch transformieren können. Das bedeutet beispielsweise, dass sich die Intensitätsverteilung des Strahls von rund (stigmatisch) zu elliptisch (astigmatisch) nach Transmission durch ein Linsensystem verändert und dass die Intensitätsellipse sogar während der Propagation rotieren kann (allgemein astigmatisch).

In dieser Arbeit wurden Modelle stigmatischer, einfach und allgemein astigmatischer Gauß-Strahlen in fundamentaler Mode untersucht. Alle Modelle können zur Simulation von Interferometersignalen verwendet werden, wie ebenfalls in dieser Arbeit beschrieben ist. Das allgemeinste und damit exakteste Modell zur Beschreibung Gaußscher Strahlen in fundamentaler Mode, ist das Modell allgemein astigmatischer Strahlen. Dieses Modell ist jedoch auch das komplexeste sowie das am wenigsten in der Literatur diskutierte, soweit die Autorin weiß. Das in dieser Arbeit beschriebene allgemein astigmatische Modell umfasst die vorher in der Literatur vorhandenen Informationen zusammen mit einer Herleitung der Gleichungen, die Strahltransformationen an einer Grenzfläche ermöglichen.

Um die Zuverlässigkeit des allgemein astigmatischen Strahlmodells zu zeigen, wurde eine experimentelle Verifizierung durchgeführt. In dieser Verifizierung wurde die Entwicklung der Intensitäts-Ellipse eines allgemein astigmatischen Strahls studiert. Dieser allgemein astigmatische Strahl wurde durch Transmission eines einfach astigmatischen Strahls durch ein optisches System bestehend aus zwei Zylinder-Linsen experimentell wie auch in einer Simulation erzeugt. Die resultierenden Ergebnisse wurden verglichen und zeigten gute Übereinstimmung.

In dieser Arbeit wurde der Einfluss der Wahl des Strahlmodells auf die Pfadlängen-Auslesung untersucht anhand von Designs von optischen Abbildungssystemen für das Testmassen-Interferometer einer LISA-ähnlichen Mission. Um den Einfluss vereinfach-

ter Strahlmodelle abzuschätzen, wurde eine Auswahl realistisch ausgerichteter Aufbauten analysiert und die Ergebnisse verglichen, die mit verschiedenen Strahlmodellen erzeugt worden waren. Diese Untersuchung hat gezeigt, dass mit den aktuellen Messungenauigkeiten der Strahl- und Linsen-Parameter, die Wahl des Strahlmodells nicht den Bereich der möglichen Kreuzkopplung verändert. Hingegen können die Ergebnisse für jedes einzelne imperfekt ausgerichtete System mit wohlbekannten Parametern mit den verschiedenen Modellen erhebliche Abweichungen zeigen.

Schlüsselwörter: Interferometrie, Gauß-Strahlen, allgemein Astigmatismus

Acknowledgements

First and foremost, I express my deepest gratitude to Karsten Danzmann. He made this wonderful experience possible for me, coming from a very different field of expertise and having a very basic understanding of gravitational wave astronomy and laser interferometry at the time when I started my work at Albert Einstein Institute. I am very grateful for his trust and confidence, for his support and encouragement, for his incredible ability to motivate, inspire and to think positively. It is truly amazing how he values his employees and how he always finds great solutions for complex problems. It is a pleasure and honor to be a part of the Albert Einstein Institute, a fantastic place with a perfect working environment.

I would also like to say a big thank you to Gerhard Heinzl, who could answer seemingly every question that ever arose in the Space Interferometry group. Each discussion with him resulted in a bunch of new ideas, solutions and approaches that deepened my knowledge and widened my field of view. Being enormously busy with different projects, he could always find a bit of time to answer questions, discuss problems and provide important hints, or even detailed explanations.

Another very special thanks goes to Gudrun Wanner, my closest colleague and a good friend. We have spent endless hours discussing all kinds of problems starting with the simulation results and ending with my never ending issues with german formalities. I admire her meticulous attention to quality and detail and perfectionism that have been a great help for me along the entire long way of thesis-writing.

I am also grateful to Michael Tröbs who was always there to answer all my experiment-related questions. He is also an amazing proof-reader, whose comments are not only particularly helpful, but also magically encouraging.

Thanks to Dennis Schmelzer, who chose the experimental investigation of general astigmatism as his bachelor project and thus helped me to test my work and to see the fancy rotating ellipses not only in formulae, but also in the experiment. It was absolutely fantastic feeling to see that the model I've been working on indeed predicts the real-life phenomena.

I would also like to thank Andreas Freise, who kindly agreed to be my referee and stay in Hannover for my defense. It is an honor for me to be evaluated by someone with such a wealth of experience in laser interferometry simulations.

Thanks to Heather Audley, a wonderful friend, kind proof-reader and great personality.

I would like to express my gratitude to all colleagues in the institute. It has been a great experience and a great time! I've learnt a lot from all of them and become good friends with many of them. It is a pleasure and honor to work with so many truly amazing people, who are so passionate about their work.

Last but not least, I want to say a big thank you to my family. Without their support I would never even have dared to move to Germany and start my PhD. Even more than that, I am very grateful to my dad, the experienced engineer, who has helped me to produce so many beautiful 3D pictures. A very special thanks to my dear husband. He did not only bear with me and my total immersion in the thesis within the last months, but also helped me to enhance my programming skills and to catch the most tricky bugs in the code. I am hugely indebted to my family for all their kindness, understanding and love.

Contents

Abstract	i
Kurzzusammenfassung	iii
Acknowledgements	v
1. Introduction	1
1.1. Gaussian beams in fundamental mode	2
1.2. This thesis	3
2. Simulating laser interferometers	5
2.1. Beam tracing	6
2.2. Interferometer signals	8
2.2.1. Photocurrent on the detector	8
2.2.2. Signal computation on a single element photodiode	11
2.2.3. Signal computation on a quadrant photodiode	12
2.2.4. Interferometer signals outlook	13
2.3. Choice of the beam model	14
3. Stigmatic Gaussian beam	17
3.1. Complex amplitude of the electric field	18
3.2. Intensity distribution	20
3.3. Phase distribution	22
3.4. Beam propagation	24
3.5. Beam transformation	25
4. Simple astigmatic Gaussian beam	27
4.1. Complex amplitude of the electric field	28

4.2.	Intensity and phase distribution	30
4.3.	Beam propagation	31
4.4.	Beam transformation	33
4.4.1.	Reflection	36
4.4.2.	Refraction	37
5.	General astigmatic Gaussian beam	39
5.1.	Complex amplitude of the electric field	40
5.2.	The law of propagation	43
5.3.	Intensity and phase distribution	44
5.3.1.	Beam parameters	44
5.3.2.	Beam evolution	47
5.4.	Beam transformation	50
6.	Experimental verification of the general astigmatic Gaussian beam model	57
6.1.	General setup	58
6.1.1.	Cylindrical lenses	60
6.1.2.	Charge-coupled device (CCD) camera	63
6.2.	Comparison of experimental and simulated results	64
6.3.	First measurements with manually defined setup	65
6.3.1.	Characterization of the initial beam	65
6.3.2.	Manually defined lens configuration	66
6.3.3.	Measurement results	67
6.3.4.	Fit of the intensity ellipse angle evolution	68
6.3.5.	Analysis of the impact of individual parameters	73
6.3.6.	Comparison of the intensity ellipse semi-axes	75
6.3.7.	Comparison of intensity distributions	76
6.3.8.	Conclusion	76
6.4.	Optimal setup search	77
6.4.1.	Criteria of optimal setup	77
6.4.2.	Optimal lens configuration	78
6.5.	Measurements with the nearly optimal setup	79
6.5.1.	Nearly optimal lens configuration	80
6.5.2.	Measurement results	81
6.5.3.	Fit of the intensity ellipse angle evolution	81
6.5.4.	Comparison of the intensity distributions	81
6.5.5.	Conclusion	85
6.6.	Measurements with improved initial beams	85
6.6.1.	Characterization of the improved initial beams	85
6.6.2.	Lens configuration	88
6.6.3.	Fit of the intensity ellipse evolution	88
6.6.4.	Comparison of intensity distributions	89
6.7.	Conclusion and outlook	92

7. The implication of beam model choice on a pathlength readout	93
7.1. Imaging optics	94
7.2. Designs of the imaging optics systems	96
7.3. Analysis of pathlength readout	97
7.3.1. Aligned imaging optics systems	100
7.3.2. Transversal shift of the second lens	101
7.3.3. Realistically misaligned imaging optics	108
7.4. Conclusion	114
8. Summary and outlook	117
A. Curvature matrix of second order surface	119
A.1. Curvature matrix of ellipsoidal surface	119
A.2. Curvature matrix of spherical surface	122
B. Algorithm of the optimal setup search	123
B.1. Possible two lens configurations	123
B.2. Algorithm description	124
B.3. Code listing	127
Publications	146
Project Documents	147
Curriculum Vitae	148

List of Figures

1.1.	LISA constellation.	2
1.2.	The example of color-coded intensity ellipses of a general astigmatic Gaussian beam at different positions along the beam axis.	3
2.1.	The transformation of the beam-fixed coordinate system of the incident beam into the beam-fixed coordinate systems of the reflected and the refracted beams.	7
2.2.	Quadrant photodiode (QPD) with four quadrants, separated by the insensitive slit.	12
2.3.	A non-orthogonal optical system consisting of two spherical lenses. . .	15
3.1.	The evolution of beam radius of a stigmatic Gaussian beam.	21
3.2.	Gouy phase jumps at the interface.	23
3.3.	The evolution of radius of curvature of wavefront of a stigmatic Gaussian beam.	24
4.1.	The principal coordinate system of a simple astigmatic Gaussian beam tilted with respect to its beam-fixed coordinate system.	29
4.2.	The evolution of beam width of a simple astigmatic Gaussian beam. .	31
4.3.	The evolution of beam widths and of radii of curvature of wavefront of a simple astigmatic Gaussian beam.	32
4.4.	Reflection and refraction of a simple astigmatic Gaussian beam at an ellipsoidal surface.	34
5.1.	A Gaussian beam (or Collins) chart.	48
5.2.	The evolution of beam width of a general astigmatic Gaussian beam. .	49
5.3.	The evolution of beam widths and of radii of curvature of wavefront of a general astigmatic Gaussian beam.	51

5.4. Reflection and refraction of a general astigmatic Gaussian beam at an ellipsoidal surface.	52
6.1. A simplified schematic of experiment.	58
6.2. Cylindrical lens and its geometrical parameters.	60
6.3. Characterization of the initial beam.	65
6.4. Intensity profile of the initial beam at a position close to the waist. . .	66
6.5. Lab photograph of the manually defined setup.	67
6.6. The measured evolution of orientation and major and minor semi-axes of intensity ellipse as beam propagates behind the second lens of the manually defined setup.	68
6.7. The evolution of intensity ellipse of the general astigmatic beam produced by the manually defined setup. Snapshots from the CCD camera. . .	70
6.8. The evolution of intensity ellipse of the general astigmatic beam produced by the manually defined setup. Snapshots from the simulation.	71
6.9. The evolution of intensity ellipse orientation as beam propagates behind the second lens of the manually defined setup.	72
6.10. Variation of individual parameters of the manually defined setup in equidistant steps.	74
6.11. The evolution of principal radii of intensity ellipse of the general astigmatic beam as it propagates behind the second cylindrical lens of the manually defined setup.	76
6.12. The performance of the optimal lens configuration found by the simulation for the optimal setup search.	79
6.13. Lab photograph of the nearly optimal setup.	80
6.14. The evolution of intensity ellipse of the general astigmatic beam produced by the nearly optimal setup. Snapshots from the CCD camera.	82
6.15. The evolution of intensity ellipse of the general astigmatic beam produced by the nearly optimal setup. Snapshots from the simulation.	83
6.16. Evolution of the intensity ellipse orientation as the beam propagates behind the second lens of the nearly optimal setup.	84
6.17. Characterization of the first improved initial beam.	86
6.18. Intensity profile of the improved beam at a position close to the waist.	86
6.19. Characterization of the second improved initial beam.	87
6.20. Intensity ellipse evolution as beam propagates behind the second lens of the nearly optimal setup. The initial beam is the first improved nearly circular beam.	89
6.21. Intensity ellipse evolution as beam propagates behind the second lens of the nearly optimal setup. The initial beam is the second improved nearly circular beam.	90
6.22. The evolution of intensity ellipse of the general astigmatic beam produced from the first improved initial beam by the nearly optimal setup.	91
7.1. The simplified not to scale schematic of the imaging optics system as it is implemented in the simulation.	95

7.3. The tilt of the test mass by an angle α results in the tilt of the measurement beam by an angle 2α	97
7.2. The imaging optics systems for the test mass interferometer.	99
7.4. The LPS for perfectly aligned imaging optics systems.	103
7.5. The LPS ^{L_{PF}} on the QPD for the imaging optics systems with the second lens shifted orthogonally to the plane of the measurement beam tilt in 10 equidistant steps from 0 μm to 10 μm	105
7.6. The LPS on the SEPD for the imaging optics systems with the second lens shifted orthogonally to the plane of the measurement beam tilt in 10 equidistant steps from 0 μm to 10 μm	107
7.7. The LPS ^{L_{PF}} on the QPD for 100 realistically misaligned variations of each of the imaging optics systems.	111
7.8. The LPS on the SEPD for 100 realistically misaligned variations of each of the imaging optics systems.	113
7.9. The LPS for the QPD and SEPD for the single instance of the realistically misaligned imaging optics system TMIO-M1-EP426-01.	114
A.1. Coordinate transformation for an ellipsoidal surface.	120
B.1. The flowchart of the algorithm of the optimal setup search.	125
B.2. The flowchart of the algorithm of the local best result search with the two specific cylindrical lenses.	126
B.3. The flowchart of the algorithm of the local best result search with the specific configuration of the two cylindrical lenses.	126

List of Tables

6.1. The list of parameters of the initial beam.	59
6.2. Parameters of a cylindrical lens.	61
6.3. Linear sizes of cylindrical lenses.	61
6.4. Measured focal lengths of cylindrical lenses and tolerances of these measurements.	62
6.5. The list of parameters of the CCD camera.	63
6.6. The values of the parameters of the CCD camera and their tolerances.	63
6.7. The parameters of simple astigmatic beam obtained by fitting Gaussian curves into the measured beam radii.	66
6.8. The parameters of the manually defined lens configuration.	67
6.9. Measured and fitted parameters of the manually defined setup.	73
6.10. The parameters of optimal lens configuration, found by the simulation for the optimal setup search.	78
6.11. Measured and fitted parameters of the nearly optimal setup.	84
6.12. The list of parameters of the first improved initial beam.	86
6.13. The list of parameters of second improved initial beam.	87
6.14. The parameters of nearly optimal lens configurations that were used in the measurements with the improved beams.	88
6.15. Measured and fitted parameters for the measurement with the first improved initial beam.	90
6.16. Measured and fitted parameters for the measurement with the second improved initial beam.	91
7.1. The requirements for the imaging optics systems for the test mass interferometer.	95
7.2. The parameters of the imaging optics systems for the test mass interferometer.	97

7.3. The uncertainties of the parameters of the imaging optics systems in the test mass interferometer.	109
7.4. The uncertainties of the beam parameters in the test mass interferometer.	109
7.5. The parameters of the single instance of the realistically misaligned imaging optics system TMIO-M1-EP426-01.	115
B.1. Possible combinations of two cylindrical lenses.	124

List of Symbols

$(\hat{d}_1, \hat{d}_2, \hat{n})$	local coordinate system of a surface at the point of incidence
$(\hat{x}, \hat{y}, \hat{z})$	beam-fixed coordinate system
$(\hat{x}_i, \hat{y}_i, \hat{z}_i)$	beam-fixed coordinate system of the incident beam
$(\hat{x}_r, \hat{y}_r, \hat{z}_r)$	beam-fixed coordinate system of the reflected beam
$(\hat{x}_t, \hat{y}_t, \hat{z}_t)$	beam-fixed coordinate system of the refracted (transmitted) beam
$A(\mathbf{r}, z)$	real valued amplitude of the electric field
C	complex amplitude of the heterodyne power
$C(z)$	matrix that represents the phase ellipse
C_s	curvature matrix of a surface
$E(\mathbf{r}, z)$	complex amplitude of electric field
$E(\mathbf{r}, z, t)$	complex wavefunction or electric field
$E_0(z)$	normalisation constant of electric field
F	ellipse flattening
$I(\mathbf{r}, z)$	optical intensity
$J(t)$	photocurrent
K_i, K_r, K_t	coordinate transformation matrices between the beam-fixed coordinate systems of incident, reflected and transmitted beams and the local coordinate system of a surface
M^2	beam propagation factor
O'	point of incidence
P	beam power
P_0	beam position
P_S	power on a detector surface
P_m	sensed power of the measurement beam on photodiode
P_r	sensed power of the reference beam on photodiode
$Q(z)$	complex radius of curvature tensor for generalized Gaussian beams
Q_i, Q_r, Q_t	complex radius of curvature tensors of incident, reflected and transmitted beams

$R(z)$	radius of curvature of a wavefront
R_I	radius of curvature of the surface in the plane of incidence
R_S	radius of curvature of the surface in the sagittal plane
$S(\theta)$	rotation matrix
$W(z)$	matrix that represents the intensity ellipse
Z	impedance of the medium
Δs_m	measured pathlength difference
Δz	propagation distance
Δ_{fitted}	fitted normalized sums of the average differences between measured and simulated values of both intensity ellipse semi-axes and orientation
$\Delta_{\text{fitted}}^\varphi$	fitted average difference of the angles of the intensity ellipse obtained in experiment and in simulation
Δ_{nominal}	initial normalized sums of the average differences between measured and simulated values of both intensity ellipse semi-axes and orientation
$\Delta_{\text{nominal}}^\varphi$	initial average difference of the angles of the intensity ellipse obtained in experiment and in simulation
\Im	imaginary part of the complex number
$\Phi(\mathbf{r}, z)$	phase of the electric field
$\Psi(\mathbf{r}, z)$	complex envelope
\Re	real part of the complex number
Θ	divergence of stigmatic Gaussian beam
α	angle of orientation of cylindrical lens in plane, orthogonal to the beam axis
$\bar{I}(\mathbf{r}, z)$	mean intensity
\bar{P}	mean power
β	angular offset introduced by the CCD camera
$\eta(z)$	Gouy phase shift
η_{ac}	accumulated jumps of Gouy phase
\hat{n}	normal to the surface at the point of incidence
\hat{p}_{inc}	normal to the plane of incidence
$\hat{t}_i, \hat{t}_r, \hat{t}_t$	vectors orthogonal to directions of the incident, reflected, and transmitted beams in the plane of incidence
\hat{x}, \hat{y}	transversal coordinate vectors
\hat{z}	beam direction
λ	wavelength
λ_v	wavelength in vacuum
\mathbf{d}	2D vector of transversal coordinates d_1 and d_2 in a local coordinate system of a surface
\mathbf{r}	2D vector of transversal coordinates x and y in a beam-fixed coordinate system
$\mathbf{s}(\mathbf{d})$	3D point on a surface
L	longitudinal size of the lens system
L_{in}	distance between the test mass and the first lens of the imaging system
L_{out}	distance between the photodiode and the last lens of the imaging system
CCD	charge-coupled device

DPS	differential power sensing signal
DWS	differential power sensing signal
LPS ^{LPF}	longitudinal pathlength signal on a QPD (as defined in the LISA Pathfinder mission)
LPS	longitudinal pathlength signal
QPD	quadrant photodiode
SEPD	single element photodiode
i	imaginary unit
∇^2	Laplacian operator
∇_T^2	transverse Laplacian operator
ω	angular beam frequency
$\omega(z)$	imaginary part of the inverse of q -parameter, taken with the minus sign
ω_{het}	angular heterodyne frequency
$\phi(\mathbf{r}, z)$	phase
ϕ_{ac}	accumulated phase
$\psi(x, y, z)$	complex phase
ρ	photodiode responsivity
$\rho(z)$	real part of the inverse of q -parameter
θ	angle of beam rotation around the z axis
θ^{\Im}	imaginary part of the complex valued beam angle θ
θ^{\Re}	real part of the complex valued beam angle θ
$\theta_i, \theta_r, \theta_t$	angle of incidence, reflected angle and transmitted angle
φ_R	angle of orientation of phase ellipse
φ_{TM}	test mass angle
φ_w	angle of orientation of intensity ellipse
a	asymmetry parameter
c	contrast
$c_I(\mathbf{r}, z)$	intensity contrast
c_S	curvature of a spherical surface
d	thickness of cylindrical lens
f	focal length
h	height of cylindrical lens
k	wavenumber
k_v	wavenumber in vacuum
k_i, k_r, k_t	wavenumbers of incident, reflected and transmitted beams
l	longitudinal offset introduced by the CCD camera
n	refractive index
n_i, n_t	refractive indices of the media before and after refraction
$q(z)$	complex valued q -parameter
q_i, q_r, q_t	q -parameters of the incident, reflected and transmitted beams
r	the transversal distance $\sqrt{x^2 + y^2}$ to the point (x, y)
s_{ac}	accumulated optical pathlength
t	time
w	width of cylindrical lens
$w(z)$	beam radius or spot radius

List of Symbols

w_0	waist radius
z	position on the beam axis
z_0	waist position
z_R	Rayleigh range

CHAPTER 1

Introduction

MODELLING is an essential part of science. To study the universe and its parts one needs an idea of how these parts work, and such an idea is already a model. Since early days people tried to represent the reality using their imagination. The whole mathematical science was invented to create better representations. With time they got more and more sophisticated and more and more comprehensive. But still new challenges and new requirements often motivate scientists to enhance existing models or even to develop entirely new ones. We will probably never be capable of representing the reality in its full glory. However, each particular study requires not a perfect model, but a model that represents reality sufficiently good to study specific effects and properties [1].

While models provide descriptions of real-world objects, simulations use models to predict the behavior of those objects [2]. Therefore, these two notions are closely related. Both simulations and models play a great role in modern science and, in particular, physics [3]. When the studied phenomena cannot be observed directly in the experiment, simulations can help to investigate it and predict its behavior and properties. For example, a large variety of astrophysical objects such as binary black holes and neutron stars have not been directly observed so far, but were intensely studied in the past decades with the help of analytical models and computational numerical simulations (see for example [4]). Simulations and models can also ease the experiment design. Before building complex and often expensive setups scientists can try various possibilities in a simulation and come up with the best layout at lower cost. But even when an experiment is already set up and the laboratory investigations are ongoing, simulations and models can help to enhance the understanding of the observations or explain unpredicted effects.



Figure 1.1.: LISA constellation. Credit: AEI, NASA, ESA, SSC, CXC and STScI.

In the field of space interferometry we deal with complex optical setups and high-precision measurements. The **LISA mission** [5] (see Figure 1.1) aims to detect gravitational waves, predicted by Albert Einstein. Such a detection will not only prove one more aspect of general relativity, but also give an entirely new way of "listening to the Universe" and observing various astrophysical objects. The signals produced by gravitational waves are weak. Thus, their direct detection is a big challenge. Building an instrument capable of measuring gravitational waves requires both comprehensive experiments and theoretical investigations. The latter can only be possible together with accurate simulations and models.

accurate simulations and models.

The **LISA optical bench** (the so called **LISA OB** [P1], [P3]) is one of the key elements of the LISA mission. While performing optical simulations for the LISA OB [6, chapter 10], we realized that using a simplified model of the Gaussian beam in the fundamental mode (TEM_{00}) impacts the signal read-out. One way to study the significance of this impact is to develop a model of Gaussian beam in the fundamental mode without known simplifications and to compare the signals computed using new and old models.

1.1. Gaussian beams in fundamental mode

When talking about Gaussian beams in the fundamental mode often the **stigmatic (or circular) Gaussian beams** are assumed. Such beams have circular light spots and spherical (or flat) wavefronts at every point along the optical path. However, this is not the only possible configuration of Gaussian beams in the fundamental mode. They can also be **simple (or orthogonal)** and **general astigmatic**. Both types of astigmatic beams have elliptical light spots and ellipsoidal (or hyperboloidal) wavefronts [7]. For brevity we will denote all non-spherical wavefronts as ellipsoidal (or elliptical) within this thesis. For simple astigmatic beams the ellipses of constant intensity and ellipses of constant phase are aligned at every point along the beam path. These ellipses can be tilted around the beam axis, but this angle remains unchanged along the propagation. Therefore, each simple astigmatic Gaussian beam has two principal directions in the transversal plane and can thus be called elliptical. For general astigmatic beams [8] in contrary the ellipses of constant intensity and ellipses of constant phase are oriented at an oblique angle with respect to each other at every point along the beam path. Moreover, the orientations of both ellipses as well as their relative orientation change along the propagation (see example of rotating light spots in Figure 1.2).

Often circular Gaussian beams are used in optical simulations. However, in many cases astigmatic Gaussian beams are produced in the experiment. Some laser sources produce non-rotationally symmetric beams [7], which can be represented with simple astigmatic Gaussian beam model. And even if the initial beam is stigmatic, it can be transformed into a simple astigmatic for example via reflection or refraction at a spherical lens if the incidence is non-normal [9]. To transform simple astigmatic beam into general astigmatic it is again sufficient to propagate it through a spherical lens. The beam becomes general astigmatic for example when none of the two principal directions of the simple astigmatic beam in its transversal plane lies in the **plane of incidence**, defined by the beam direction and the surface normal at the point of incidence. Since any optical system in reality is slightly misaligned, simple and general astigmatic beams can appear almost in every optical system. However, in many cases the intensity and phase ellipses of these beams have a small ellipticity and thus the stigmatic approximation is good enough for many purposes. In the LISA OB the picometer sensitivity is required and therefore we need to investigate the impact of the beam model on the main science signal.

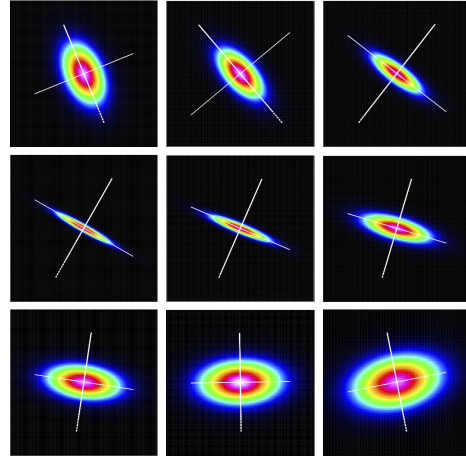


Figure 1.2.: The example of color-coded intensity ellipses of a general astigmatic Gaussian beam at different positions along the beam axis. The white lines show the orientations of major and minor semi-axes of ellipses.

1.2. This thesis

While working on LISA Pathfinder it was found [6, p. 93] that angular beam jitter in the order of hundreds of μrad can influence the main science signal, namely the longitudinal pathlength signal (signal definition will follow in Chapter 2). This effect was evaluated using a software tool called OptoCad [10] that traces simple astigmatic Gaussian beams through 2D optical setups. The signals for the resulting beams interfering on the detector were computed by an in-house software called QPD.c [6, p. 26] that used circular beam approximation at that time.

For the LISA OB similar investigations of the angular beam jitter need to be performed. Some subsystems of the LISA OB include curved surfaces. Since these surfaces can be misaligned, general astigmatic beams can appear. The evaluation of the impact of general astigmatism on interferometer signals requires development and implementation of a general astigmatic beam model.

In this thesis the complete models for stigmatic, simple and general astigmatic Gaussian beams will be presented. Each can be used to compute interferometer

signals. In the end the interferometer signals produced by each model for the same setup will be compared and the significance of using the accurate beam model will be investigated.

The models for stigmatic and simple astigmatic beams are relatively well-known (even though the concrete realizations may vary). Circular Gaussian beam approximation often implies the assumption of normal incidence in all beam transformations. Therefore it does not allow a precise evaluation of the effect of angular beam jitter even in simple optical systems, involving only flat and spherical surfaces. Simple astigmatic beams can be used in beam jitter simulations in orthogonal optical systems. In 3D it means that for their correct implementation one has to keep track of the planes of symmetry and forbid any transformations that break this symmetry. General astigmatic beams do not have these limitations. Unfortunately, we have found the least number of publications regarding general astigmatic beams and had to develop our own general astigmatic Gaussian beam model that includes all aspects that are necessary to simulate beam propagation in an arbitrary optical system, including non-normal incidence at curved surfaces. The general astigmatic Gaussian beam model suggested in this thesis does not only combine the previously available investigations, but also corrects the errors and generalizes the beam transformation equations from [11] to avoid restrictions in the choice of beam-fixed and surface-fixed coordinate systems. The important advantage of the model suggested here is that it allows to study the impact of simple and general astigmatism on the interferometer signals even when the ellipticity of both light spots and wavefronts is small along the propagation and thus considered to be negligible in many other models. All three models are implemented in the software tool IfoCad [P4] that is capable of computing interferometer signals as described in [P2].

I will start with an overview of the procedure of simulating laser interferometers given in Chapter 2. Its main principals are identical for all types of beams. They include beam tracing through optical systems and computation of interferometer signals on photodiodes. In this chapter I will also show how the beam model couples into the process of simulating laser interferometers. In the next three chapters (Chapter 3, chapter 4 and Chapter 5) I will present the mathematical descriptions of stigmatic, simple and general astigmatic Gaussian beams correspondingly. All three beam descriptions are ready to use in the simulation procedure described in Chapter 2. The general astigmatic beam model is the most general and also the most complex of the three models of Gaussian beams in fundamental mode. Since the model presented in this thesis is new, we have performed an experiment in order to prove its trustworthiness. The results of such verification will be presented in Chapter 6. In Chapter 7 I will present the study of the imaging optics systems for the test mass interferometer of a LISA-like mission, concentrating on the impact of the beam model on the longitudinal pathlength signal. With this I will compare the performance of all three models and show the consequences of simplifications.

Simulating laser interferometers

IN experiments interferometer signals are usually obtained using a phasemeter (see [12–14]). It converts the photocurrent recorded on a photodiode into meaningful signals. Usually the photocurrent results from the interference of two beams impinging on the photodiode. The interferometers are used for precision length measurements. Therefore, the main science interferometer signal measures the pathlength difference between the two interfering beams. It is called **longitudinal pathlength signal (LPS)**. The **contrast** or fringe visibility of the interference pattern is another interferometer signal that provides the general information of alignment status of the interferometer. On **quadrant photodiode (QPD)** additionally two alignment signals are available to characterize the interferometer: **differential wavefront sensing (DWS)** and **differential power sensing (DPS) signals**. Both make use of the four element spatial distribution, resulting from separate recordings of the photocurrent on each quadrant. The DPS (or ratiometric) signal measures the beam centroid on the photodiode [12], while DWS senses the relative beam tilt [15]. In case when only one beam impinges on the photodiode, DPS signal still shows its shift from the center of the photodiode. DWS signal only makes sense when two beams are interfering.

In order to simulate the interferometer signals one needs the complete information about both beams impinging on the photodiode. To obtain this information the beams must first be traced through the optical system from some reference point, where the beam parameters are defined. **Beam tracing** includes a sequence of beam propagations and transformations via reflection and refraction on surfaces of the optical system.

Both beam tracing and signal computation are very similar for different beam models. In this chapter I will introduce the concepts that are identical for all kinds of beams, leaving the components that differ for the next chapters. The concepts

of laser interferometer simulations will be presented in this chapter in the same way as they are implemented in IfoCad [P4]. Since the beam tracing prefaces the signal computation, I will start with its main concepts in Section 2.1. Then I will introduce the process of simulating interferometer signals (Section 2.2). In Section 2.3 I will give an overview of the impact of the choice of the beam model on the procedure of simulating laser interferometers. I will discuss the remaining physical parameters that depend on a choice of the beam model and are not discussed in this chapter. I will also describe the conditions, in which one type of Gaussian beams in fundamental model can be transformed into another.

2.1. Beam tracing

The procedure of beam tracing through the optical system is a sequence of beam propagations and transformations via reflection and refraction on surfaces of the system. Therefore, it requires representations of beams and surfaces together with the laws of propagation, reflection and refraction. Beam representation as well as all three laws depend on the choice of the beam model. Surface representation is generally independent of the beam model. It should be mentioned, however, that the beam transformations on some types of surfaces can only be simplified when using circular or simple astigmatic beam model.

The beam-tracing can be split up into so-called geometrical and physical parts with the geometrical part being identical for all types of beams. The physical part is different for each of the beam models and will be presented in the corresponding Chapters (3, 4 and 5). This section is dedicated to the geometrical part of the beam tracing.

The geometrical part of the light beam representation is a **ray**, which consists of the current position P and the **beam-fixed coordinate system** $(\hat{x}, \hat{y}, \hat{z})$. Vectors $\hat{x}, \hat{y}, \hat{z}$ are the unity vectors that form orthonormal basis such that vector \hat{z} shows the beam direction and the transversal coordinate vectors \hat{x} and \hat{y} can be chosen arbitrarily. For simple astigmatic beams, however, it is convenient to choose the beam-fixed coordinate system to be the **beam principal coordinate system**. In such coordinate system the transversal vectors are oriented along the principal axes of the beam ellipse. In case if other coordinate system is chosen, the angle between the principal axes of the beam ellipse and the transversal vectors of the beam-fixed coordinate system has to be introduced. The position P indicates the current point of interest, where all physical beam parameters are given.

The geometrical part of the surface representation consists of the point of incidence O' and the normal to the surface at the point of incidence \hat{n} .

As the beam propagates over a distance Δz its position changes as

$$P'_0 = P_0 + \Delta z \hat{z}. \quad (2.1)$$

Here P'_0 is the new beam position. The beam-fixed coordinate system remains unaffected along the propagation. It changes via reflection and refraction following

the corresponding laws from geometrical optics [16, chapter 4]: the **law of reflection**

$$\begin{aligned}\theta_r &= \theta_i, \\ \hat{z}_r &= \hat{z}_i - 2(\hat{z}_i \cdot \hat{n})\hat{n},\end{aligned}\tag{2.2}$$

and the **law of refraction (Snell's law)**

$$\begin{aligned}\cos \theta_i &= \hat{z}_i \cdot \hat{n}, \\ n_i \sin \theta_i &= n_t \sin \theta_t, \\ \cos \theta_t &= \sqrt{1 - \sin^2 \theta_t}, \\ \hat{z}_t &= \frac{n_i}{n_t} \hat{z}_i + (\cos \theta_t - \frac{n_i}{n_t} \cos \theta_i) \hat{n}.\end{aligned}\tag{2.3}$$

Here \hat{z}_i , \hat{z}_r and \hat{z}_t are the directions of the incident, reflected and refracted (transmitted) beams correspondingly, n_i and n_t are the refractive indices of the media before and after the refraction, θ_i is the angle of incidence, θ_r and θ_t are the angles between the surface normal and the reflected and transmitted beams correspondingly (see Figure 2.1).

Both the reflected and the refracted beam directions (\hat{z}_r and \hat{z}_t) lie in the plane of incidence [17, chapter 1].

There are many possible ways to transform the transversal vectors via reflection or refraction. The natural way is to use the following approach:

$$\begin{aligned}\hat{x}_r &= (\hat{x}_i \cdot \hat{p}_{\text{inc}})\hat{p}_{\text{inc}} + (\hat{x}_i \cdot \hat{t}_i)\hat{t}_r, \\ \hat{x}_t &= (\hat{x}_i \cdot \hat{p}_{\text{inc}})\hat{p}_{\text{inc}} + (\hat{x}_i \cdot \hat{t}_i)\hat{t}_t, \\ \hat{y}_r &= (\hat{y}_i \cdot \hat{p}_{\text{inc}})\hat{p}_{\text{inc}} + (\hat{y}_i \cdot \hat{t}_i)\hat{t}_r, \\ \hat{y}_t &= (\hat{y}_i \cdot \hat{p}_{\text{inc}})\hat{p}_{\text{inc}} + (\hat{y}_i \cdot \hat{t}_i)\hat{t}_t,\end{aligned}\tag{2.4}$$

where

$$\begin{aligned}\hat{p}_{\text{inc}} &= \frac{\hat{z}_i \times \hat{n}}{|\hat{z}_i \times \hat{n}|}, \\ \hat{t}_i &= \hat{z}_i \times \hat{p}_{\text{inc}}, \quad \hat{t}_r = -\hat{z}_r \times \hat{p}_{\text{inc}}, \quad \hat{t}_t = \hat{z}_t \times \hat{p}_{\text{inc}}.\end{aligned}\tag{2.5}$$

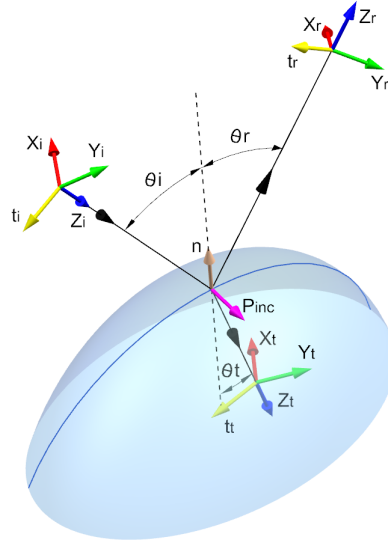


Figure 2.1.: The transformation of the beam-fixed coordinate system of the incident beam into the beam-fixed coordinate systems of the reflected and the refracted beams.

The above equations imply that the projections of each of the transversal vectors (\hat{x}_l, \hat{y}_l , where $l = i, r, t$) onto the normal to the plane of incidence \hat{p}_{inc} and on the corresponding vector $\hat{t}_l, l = i, r, t$, lying in the plane of incidence, remain unchanged after the beam transformations. Then if the incoming beam tilts in, say, the (\hat{x}_i, \hat{z}_i) plane, the reflected and the refracted beams will tilt in corresponding $(\hat{x}_l, \hat{z}_l), l = r, t$ planes. This approach to the transformation of the transversal vectors can also be used to represent the beam polarization. Alternatively any orthonormal coordinate system with the \hat{z} vector representing beam direction can be chosen. The coordinate transformation completes the description of the geometrical part of the beam-tracing.

2.2. Interferometer signals

After the beam-tracing is completed and the parameters of the two beams impinging on the photodiode are obtained the interferometer signals can be computed. The signal computation procedure has peculiar properties for **homodyne** and **heterodyne interferometers**. By definition, in homodyne interferometers interfering beams have identical frequencies, while in heterodyne interferometers they are frequency shifted. In the LISA mission interferometers are heterodyne. However, homodyne interferometers are involved in some of the dedicated experiments. Therefore, it is important to have the possibility to simulate both kinds of interferometers.

The signal computation procedure depends on the choice of the photodetector (**single element photodiode (SEPD)** or **quadrant photodiode (QPD)**). In this section I will talk about both possibilities.

When interferometers are used for length measurements one of the interfering beams is usually called **reference beam**, the other one called **measurement beam** [P2]. I will follow this notation here.

2.2.1. Photocurrent on the detector

The reference and measurement beams interfere on the detector, which results in time-varying **photocurrent** $J(t)$ proportional to the beam power P_S on a detector surface [17, p. 754]:

$$J(t) = \rho P_S(t). \quad (2.6)$$

Here ρ is the **photodiode responsivity**.

The sensed **beam power** on the photodiode can be computed as the integral of the optical intensity of the interference pattern over the detector surface:

$$P_S(t) = \int I(\mathbf{r}, z, t) dS, \quad (2.7)$$

where $\mathbf{r} = (x, y)$ is a vector of transversal coordinates. The **optical intensity** is defined as

$$I(\mathbf{r}, z, t) = \frac{1}{2Z} |E_r(\mathbf{r}, z, t) + E_m(\mathbf{r}, z, t)|^2, \quad (2.8)$$

where Z is the **impedance of the medium**, $E_r(\mathbf{r}, z, t)$ and $E_m(\mathbf{r}, z, t)$ are the **electric fields** of the two interfering beams. Neither the photodiode responsivity ρ , nor the impedance of the medium Z are needed for the signal computation. They can be set to $\rho = 2Z = 1$ in the simulation. However, I will leave them in for completeness.

The representation of the **electric fields** depends on the choice of the beam model. However, it is always possible to represent it as

$$E(\mathbf{r}, z, t) = E(\mathbf{r}, z) \exp(i\omega t), \quad (2.9)$$

where ω is the **angular beam frequency**. The time-dependent component $\exp(i\omega t)$ is identical for all types of beams, while the **complex amplitude of electric field** $E(\mathbf{r}, z)$ differs. However, its concrete representation does not affect the general signal computation procedure. Therefore, in this chapter I will leave the expression for the complex amplitude of electric field undefined. It will be obtained in the subsequent chapters for each of the beam models and can be substituted in the general signal computation procedure presented here.

Let me first rewrite the complex amplitude of the electric field using the real-valued amplitude $A(\mathbf{r}, z)$ and phase $\Phi(\mathbf{r}, z)$:

$$E(\mathbf{r}, z) = A(\mathbf{r}, z) \exp(-i\Phi(\mathbf{r}, z)). \quad (2.10)$$

Then the expression for electric field (equation (2.9)) changes to

$$E(\mathbf{r}, z, t) = A(\mathbf{r}, z) \exp(i\omega t - i\Phi(\mathbf{r}, z)). \quad (2.11)$$

Using this notation the optical intensity (equation (2.8)) becomes:

$$\begin{aligned} I &= \frac{1}{2Z} |A_r \exp(i\omega_r t - i\Phi_r) + A_m \exp(i\omega_m t - i\Phi_m)|^2 \\ &= \frac{1}{2Z} \{A_r^2 + A_m^2 + 2A_r A_m \cos[(\omega_m - \omega_r)t - (\Phi_m - \Phi_r)]\} \\ &= \frac{1}{2Z} (A_r^2 + A_m^2) \left[1 + \frac{2A_r A_m}{A_r^2 + A_m^2} \cos(\omega_{\text{het}} t - \Delta\Phi) \right]. \end{aligned} \quad (2.12)$$

In heterodyne interferometers the **angular heterodyne frequency** is defined as

$$\omega_{\text{het}} = \omega_m - \omega_r. \quad (2.13)$$

In homodyne interferometers both beams have identical frequencies and thus $\omega_m - \omega_r = 0$.

For the infinitesimal photodetector $\Delta\Phi$ is constant on its surface and can be converted into the difference between the optical pathlengths of the interfering beams:

$$\Delta\Phi = k_v \Delta s_m = \frac{2\pi}{\lambda_v} \Delta s_m, \quad (2.14)$$

where k_v is the wavenumber and λ_v is the optical wavelength in vacuum, Δs_m is the measured pathlength change between the two interfering beams. Unfortunately,

Δs_m is only an approximation of the real optical pathlength difference Δs , since it depends on a beam curvature, relative angle of the interfering beams and many other parameters.

The optical intensity in a homodyne interferometer is constant with time and depends only on the phase difference $\Delta\Phi$ and thus (see equation (2.14)) the differential arm length changes of the interferometer. In heterodyne interferometer ($\omega_{\text{het}} \neq 0$) the interference pattern oscillates with time even if the phase difference is constant.

Due to the sinusoidal shape of the intensity pattern the average intensity is reached if the cosine is zero:

$$\bar{I} = A_r^2 + A_m^2. \quad (2.15)$$

The maximum and minimum values are reached when cosine is equal to 1 or -1. Then the contrast c_I of the intensity is

$$c_I = \frac{I_{\max} - I_{\min}}{I_{\max} + I_{\min}} = \frac{2A_r A_m}{A_r^2 + A_m^2} \quad (2.16)$$

and the intensity can be expressed as

$$I = \bar{I}[1 + c_I \cos(\omega_{\text{het}} t - \Delta\Phi)]. \quad (2.17)$$

Substituting this equation into the definition of power (2.7) and using the fact that the superposition of sinusoids with equal frequency is a sinusoid with the same frequency, we obtain:

$$P_S = \bar{P}[1 + c \cos(\omega_{\text{het}} t - \phi)]. \quad (2.18)$$

Here \bar{P} is the **average power** on the photodiode, c is the **contrast** and ϕ is the **phase**.

The mean intensity \bar{I} , intensity contrast c_I and phase difference $\Delta\Phi$ are different at any point on a detector surface, while mean power \bar{P} , contrast c and phase ϕ are integrated over detector surface and therefore defined for the entire surface. Equation (2.14) is given on the infinitesimal photodetector. For the phase ϕ we can write down the corresponding equation for the arbitrary photodetector:

$$\phi = k_v \Delta s_m = \frac{2\pi}{\lambda_v} \Delta s_m. \quad (2.19)$$

In this case the measured optical pathlength difference is again only the approximation of its real value, depending on many parameters, including the size and shape of the detector.

Equation (2.18) gives the interpretation of the sensed beam power on the photodiode. In the next step I will show how to extract the mean power \bar{P} , contrast c and phase ϕ from the known sensed beam power P_S . Then these values can be combined into meaningful interferometer signals.

2.2.2. Signal computation on a single element photodiode

Single element photodiode (SEPD) has single surface, usually circular, and therefore records single photocurrent, from which the interferometer signals can be extracted.

The sensed power of each individual beam on the photodiode can be found via integration of its optical intensity over the photodiode surface:

$$P_r = \frac{1}{2Z} \int |E_r(\mathbf{r}, z, t)|^2 dS = \frac{1}{2Z} \int |E_r(\mathbf{r}, z)|^2 dS = \frac{1}{2Z} \int A_r(\mathbf{r}, z)^2 dS, \quad (2.20)$$

$$P_m = \frac{1}{2Z} \int |E_m(\mathbf{r}, z, t)|^2 dS = \frac{1}{2Z} \int |E_m(\mathbf{r}, z)|^2 dS = \frac{1}{2Z} \int A_m(\mathbf{r}, z)^2 dS. \quad (2.21)$$

The mean power on the photodiode is defined as

$$\bar{P} = \int \bar{I} dS. \quad (2.22)$$

Using equation (2.15), it transforms into

$$\bar{P} = P_r + P_m. \quad (2.23)$$

Additionally we can compute the following complex-valued integral:

$$C = \frac{1}{2Z} \int 2E_m(\mathbf{r}, z)E_r^*(\mathbf{r}, z) dS = \int c_I \bar{I} \exp(i\Delta\Phi) dS = c\bar{P} \exp(i\phi). \quad (2.24)$$

We call the obtained value the **complex amplitude of the heterodyne power** C . Contrast c and phase ϕ can then be computed from the complex amplitude of the heterodyne power C and mean power \bar{P} as

$$c = |C|/\bar{P}, \quad (2.25)$$

$$\phi = \arg C. \quad (2.26)$$

Knowing beam parameters on the photodiode and the expression for the complex amplitude of the electric field, we can compute three integrals given in equations (2.20), (2.21) and (2.24). From the obtained values we can extract the mean power, contrast and phase using equations (2.23), (2.25) and (2.26). Phase ϕ can be transformed into the optical pathlength difference Δs_m using equation (2.19). The obtained value is nothing else but the main science signal or longitudinal pathlength signal (LPS):

$$\text{LPS} = \phi/k_v. \quad (2.27)$$

It is easy to see that heterodyne angular frequency ω_{het} was not involved in the procedure of extracting the interferometer signals on the single element photodiode. Therefore, this procedure can be used equally well for heterodyne and homodyne interferometers.

2.2.3. Signal computation on a quadrant photodiode

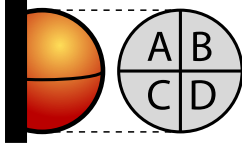


Figure 2.2.: Quadrant photodiode (QPD) with four quadrants, separated by the insensitive slit.

Quadrant photodiode consists of four quadrants, separated by the insensitive slit (see Figure 2.2). The photocurrent is recorded separately for each quadrant. It means that integration in equations (2.20), (2.21) and (2.24) should also be performed separately for each quadrant. Within this section we will name the quadrants A, B, C and D as shown in Figure 2.2. Indices l, r, t, b will stand for left, right, top and bottom

parts of the photodiode correspondingly.

Heterodyne interferometers

Using the procedure of signal computation on the single element photodiode we can find average power \bar{P} and contrast c and phase ϕ on each of the four quadrants. These four sets of values can be combined into meaningful interferometer signals.

In order to measure the position of the beam centroid we can compare the average powers on different quadrants. It will give us the horizontal and vertical differential power sensing (DPS) signals:

$$\text{DPS}_h = \frac{\bar{P}_l - \bar{P}_r}{\bar{P}_l + \bar{P}_r} = \frac{(\bar{P}_A + \bar{P}_C) - (\bar{P}_B + \bar{P}_D)}{\bar{P}_A + \bar{P}_B + \bar{P}_C + \bar{P}_D}, \quad (2.28)$$

$$\text{DPS}_v = \frac{\bar{P}_t - \bar{P}_b}{\bar{P}_t + \bar{P}_b} = \frac{(\bar{P}_A + \bar{P}_B) - (\bar{P}_C + \bar{P}_D)}{\bar{P}_A + \bar{P}_B + \bar{P}_C + \bar{P}_D}. \quad (2.29)$$

A similar comparison of the phase signals of the four quadrants can be used to measure the wavefront tilt between the two interfering beams. It results in horizontal and vertical differential wavefront sensing (DWS) signals:

$$\text{DWS}_h = \phi_l - \phi_r = \arg(C_A + C_C) - \arg(C_B + C_D) = \arg\left(\frac{C_A + C_C}{C_B + C_D}\right), \quad (2.30)$$

$$\text{DWS}_v = \phi_t - \phi_b = \arg(C_A + C_B) - \arg(C_C + C_D) = \arg\left(\frac{C_A + C_B}{C_C + C_D}\right). \quad (2.31)$$

The longitudinal pathlength signal (LPS) on a QPD can be defined in various ways. For example in the LISA Pathfinder mission [12] it is obtained as the argument of a sum of complex amplitudes of the quadrants [P2]:

$$\text{LPS}^{\text{LPF}} = \frac{1}{k_v} \arg(C_A + C_B + C_C + C_D). \quad (2.32)$$

However, there are several other possibilities to define an LPS. Finding the definition that gives the most accurate estimate for the optical pathlength difference between the two interfering beams is the work in progress.

The contrast for a QPD is defined as

$$c = \frac{|C_A| + |C_B| + |C_C| + |C_D|}{\bar{P}_A + \bar{P}_B + \bar{P}_C + \bar{P}_D}. \quad (2.33)$$

The last two signals (LPS and contrast) for a QPD are the closest known approximations of the same signals sensed by a SEPD with the same diameter.

Homodyne interferometers

In theory nothing stops us from repeating the same procedure for the homodyne interferometers: we can find the mean power \bar{P} , contrast c and phase ϕ for each of the four quadrants and combine them into LPS, DWS, DPS and contrast of the QPD. However, in reality we don't have a phasemeter that could repeat this procedure in the experiment. Therefore, we can add up the four photocurrents and obtain the contrast and the LPS signal in the same as it was done for the single element photodiode. The only possibility to define the DPS signal without finding mean powers on each of the quadrants is to use the sensed powers on the quadrants:

$$\text{DPS}_h = \frac{P_l - P_r}{P_l + P_r} = \frac{(P_A + P_C) - (P_B + P_D)}{P_A + P_B + P_C + P_D}, \quad (2.34)$$

$$\text{DPS}_v = \frac{P_t - P_b}{P_t + P_b} = \frac{(P_A + P_B) - (P_C + P_D)}{P_A + P_B + P_C + P_D}. \quad (2.35)$$

However, the sensed power is directly connected to the phase as shown in equation (2.18). Thus the DPS signal defined in such a way will not only measure the imbalance of the mean powers \bar{P} on different quadrants, but also the imbalance of phases. It means that both beam offset from the center of the photodiode and relative beam tilt between the two interfering beams will result in the changes of DPS signal. Therefore, the homodyne DPS signal is not a dedicated signal to sense a beam walk, and it gives little information about the interferometer alignment.

2.2.4. Interferometer signals outlook

This section was dedicated to an overview of a procedure that allows to compute interferometer signals in the simulation. I did not include all the technical details. For instance, I did not mention the separation of macroscopic and microscopic phase and the coordinate transformation in complex amplitude for the integration over detector surface. These are not necessary in the following discussion. Interested reader can find this additional information in [P2]. With this section I have shown that the procedure of the signal computation is identical for all kinds of beams, and the choice of the beam model only couples into the expression of the complex amplitude.

2.3. Choice of the beam model

In this chapter I have not included any description of the beam configuration. As we will see in the next three chapters, it is not identical for different types of Gaussian beam in the fundamental mode. They also obey different laws of propagation and transformation on the surfaces. In Section 2.2 it was shown that in order to compute the interferometer signals we need to know the expression for the complex amplitude of both beams impinging on photodiode. This expression depends on the type of beam and therefore the value of the complex amplitude will be different for different beam models. This, in turn, means that the signal values will differ depending on the choice of model.

In the next three chapters three models of the Gaussian beam in fundamental mode will be introduced: stigmatic, simple astigmatic and general astigmatic Gaussian beams. The propagation of stigmatic Gaussian beams through **rotationally symmetric optical systems** can be described by well-known laws [18]. In such optical systems the axis of symmetry of each surface coincides with the principal axis of each beam that is transformed on this surface. Then it is sufficient to consider beam propagation in 2D and assume that the behavior of the beam is identical in any plane containing the beam axis. The symmetry might be broken, for example, when a Gaussian beam impinges on a curved surface at an oblique angle. After such a transformation the beam becomes simple astigmatic [9]. The representation of the simple astigmatic beam can be split into two independent circular Gaussian beam representations [19], which means that the conventional laws [18] are still applicable in this case. The Gaussian beam in the fundamental mode will stay stigmatic or simple astigmatic as long as the optical system it passes through is orthogonal. In **Orthogonal optical system** every beam transformation at a surface has to satisfy the following restrictions: one of the principal directions of the beam and one of the axes of symmetry of the surface must lie in the plane of incidence. In the case of planar or spherical surfaces their axis of symmetry always lies in plane of incidence. However, if none of the principal axes of the simple astigmatic beam lie in the plane of incidence, the outgoing beam becomes general astigmatic even when the spherical surface is used. The example of an optical system that can transform stigmatic Gaussian beam into general astigmatic is shown in Figure 2.3. This system contains two spherical lenses. Since the plane of incidence on the second surface is not equal or orthogonal to the plane of incidence on the first surface, at the second transformation it is impossible to decompose the behavior of the resulting beam into two orthogonal planes. Such an **optical system is non-orthogonal** and thus the outgoing beam is general astigmatic. In many cases if only spherical lenses are used to produce general astigmatic beams both ellipses of constant intensity and of constant phase have small ellipticity, which allows to use simple astigmatic or even circular Gaussian beam approximation. However, we do stress that even optical systems consisting exclusively of rotationally-symmetric components can transform stigmatic Gaussian beams into general astigmatic. When designing high-precision instruments the difference between stigmatic or simple astigmatic approximation and the real general astigmatic beam might not be negligible.

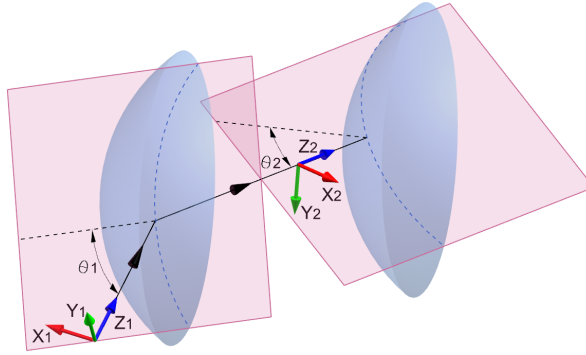


Figure 2.3.: A non-orthogonal optical system consisting of two spherical lenses. The plane of incidence for the beam transformation by the first lens and the plane of incidence for the beam transformation by the second lens are aligned at an oblique angle with respect to one other.

A strongly elliptical simple astigmatic beam can be obtained, for example, via transformation of stigmatic beam on a cylindrical surface. Then it can be transformed into a general astigmatic beam by another cylindrical surface, oriented in the plane, orthogonal to the beam axis, such that it has an oblique angle with respect to the first surface.

A general astigmatic Gaussian beam is the most general case of the Gaussian beam in fundamental mode. Simple astigmatic and circular beams can be treated as special cases of the general astigmatic beam. Therefore any general astigmatic Gaussian beam model can be thought of as a model of an arbitrary Gaussian beam in the fundamental mode. The conventional laws [18] are not applicable to general astigmatic Gaussian beams. The complete description of their propagation in free space is given in [8]. Unfortunately, this study provides limited possibilities for beam transformation and does not include the case of non-normal incidence. To our knowledge, the only work so far that deals with the transformation of astigmatic beams incident at some angle on arbitrary second order surfaces (for example spheres, ellipsoids or cylinders), is [11]. Unfortunately, this paper contains typos, which implies that one needs to re-derive the formulas from this paper in order to use them. In the end, we don't know of any readily-available complete general astigmatic Gaussian beam model that we could use in laser interferometer simulations.

The discussion of complex amplitude, intensity and phase distributions and laws of propagation, reflection and refraction will be presented in the next three chapters. Otherwise the optical simulations of interferometers follow the procedure, explained in this chapter, for every model of the laser beam.

Stigmatic Gaussian beam

In chapter 2 we have discussed the aspects of the laser interferometer simulations that are independent on the choice of a laser beam model. They include the geometrical part of the beam tracing through the optical system and the procedure of simulating interferometer signals.

In this chapter I will introduce the stigmatic model of the Gaussian beam in the fundamental mode. This model is the simplest and the most commonly used in laser interferometer simulations. It assumes the beam with circular intensity pattern and spherical or flat wavefront at every point along the propagation. Within this model only the normal incidence on a flat or spherical surface is possible without simplifications. Since in this case both the beam and the **optical system** are **rotationally symmetric** around the beam axis, the 2D representation is sufficient to fully describe the interferometer. The third dimension can be obtained by assuming that the beam behavior is identical in any meridional plane containing the beam axis.

In order to be used in laser interferometer simulations the beam model has to include four main aspects:

- the expression of the **complex amplitude of the electric field**, which is required in interferometer signals simulation;
- **intensity and phase distributions** that provide the **beam description** and its physical properties at every point along the beam path;
- the **beam propagation** that allows to transform the beam parameters as the beam propagates in some medium;
- the laws of **beam transformation** or the laws of reflection and refraction of

the beam at a surface that are necessary to trace the beam through the optical system.

In this chapter we will discuss each of these aspects in the stigmatic (or circular) Gaussian beam model.

3.1. Complex amplitude of the electric field

The complex amplitude $E(\mathbf{r}, z)$ of an electric field (see equation (2.9)) of any possible optical wave should satisfy the **Helmholtz equation**:

$$\nabla^2 E + k^2 E = 0, \quad (3.1)$$

where k is a wavenumber in the medium where the optical wave is propagating, ∇^2 is a Laplacian operator, defined as

$$\nabla^2 = \partial^2/\partial x^2 + \partial^2/\partial y^2 + \partial^2/\partial z^2 \quad (3.2)$$

in Cartesian coordinates [17, p. 43].

Essentially every laser beam is well collimated and thus its complex amplitude can be represented as the complex amplitude of a paraxial optical wave [17, chapter 2]:

$$E(\mathbf{r}, z) = \Psi(\mathbf{r}, z) \exp(-i\phi_{ac}(z) + i\eta(z)), \quad (3.3)$$

where the **complex envelope** $\Psi(\mathbf{r}, z)$ is the function of transversal coordinates $\mathbf{r} = (x, y)$ that varies slowly with z . The accumulated phase $\phi_{ac}(z)$ and the Gouy phase shift $\eta(z)$ will be discussed in details in Section 3.3.

The variation of the complex envelope $\Psi(\mathbf{r}, z)$ and its derivative with position z must be slow within the distance of a wavelength λ so that the paraxial wave approximately maintains the plane-wave nature. The complex envelope $\Psi(\mathbf{r}, z)$ of any paraxial wave has to satisfy the **paraxial Helmholtz equation** [17, chapter 2]:

$$\nabla_T^2 \Psi - i2k \frac{\partial \Psi}{\partial z} = 0, \quad (3.4)$$

where $\nabla_T^2 = \partial^2/\partial x^2 + \partial^2/\partial y^2$ is the transverse Laplacian operator.

The complex envelope of the stigmatic Gaussian beam in the fundamental mode is the solution of the paraxial Helmholtz equation (3.4) [17, chapter 3] given by:

$$\Psi(r, z) = E_0(z) \exp\left(-i k \frac{r^2}{2q}\right), \quad (3.5)$$

where

$$r = \sqrt{x^2 + y^2} \quad (3.6)$$

is the transversal distance to the point of interest. The complex-valued **q-parameter** can be represented as

$$\frac{1}{q(z)} = \frac{1}{R(z)} - i \frac{\lambda}{\pi w^2(z)}. \quad (3.7)$$

It will be shown in the next sections that R is the radius of curvature of the wavefront and w is the beam radius at the position z along the beam axis. The q -parameter is also called the complex radius of curvature.

Using equations (3.3), (3.5) and (3.7), we obtain the expression for the complex amplitude $E(r, z)$ of the stigmatic Gaussian beam:

$$\begin{aligned} E(r, z) &= E_0(z) \exp\left(-i\phi_{ac} + i\eta(z) - ik\frac{r^2}{2q(z)}\right) = \\ &E_0(z) \exp\left(-\frac{r^2}{w^2(z)} - i\phi_{ac} + i\eta(z) - ik\frac{r^2}{2R(z)}\right). \end{aligned} \quad (3.8)$$

The optical intensity is then

$$I(r, z) = |E(r, z)|^2 = E_0^2(z) \exp\left(-\frac{2r^2}{w^2(z)}\right), \quad (3.9)$$

and the total optical power carried by the beam is the integral of the optical intensity over the transverse plane:

$$\begin{aligned} P &= \int_0^\infty I(r, z) 2\pi r \, dr = \\ &\frac{\pi}{2} E_0^2(z) w^2(z) \int_0^\infty \exp\left(-\frac{2r^2}{w^2(z)}\right) d\frac{2r^2}{w^2(z)} = \\ &\frac{\pi}{2} E_0^2(z) w^2(z). \end{aligned} \quad (3.10)$$

Given the optical power P , this equation allows to compute the normalization constant $E_0(z)$:

$$E_0(z) = \frac{1}{w(z)} \sqrt{\frac{2P}{\pi}}. \quad (3.11)$$

Substituting this value into equation (3.8), we obtain the complex amplitude of the electric field of stigmatic Gaussian beam:

$$\begin{aligned} E(r, z) &= \frac{1}{w(z)} \sqrt{\frac{2P}{\pi}} \exp\left(-i\phi_{ac} + i\eta(z) - ik\frac{r^2}{2q(z)}\right) = \\ &\frac{1}{w(z)} \sqrt{\frac{2P}{\pi}} \exp\left(-\frac{r^2}{w^2(z)} - i\phi_{ac} + i\eta(z) - ik\frac{r^2}{2R(z)}\right). \end{aligned} \quad (3.12)$$

This equation can be used in signal computation.

3.2. Intensity distribution

The exponential term in equation (3.12) can be split up into real and imaginary parts. The imaginary part corresponds to the phase of the beam, while the real part represents its irradiance distribution. From equation (3.9) it follows that the optical intensity can be defined as

$$I(r, z) = \frac{2P}{\pi w^2(z)} \exp\left(-\frac{2r^2}{w^2(z)}\right), \quad (3.13)$$

At every point z along the beam axis the circle of radius r_0 contains a certain fraction of the overall beam power:

$$\frac{1}{P} \int_0^{r_0} I(r, z) 2\pi r \, dr = 1 - \exp\left[-\frac{2r_0^2}{w^2(z)}\right]. \quad (3.14)$$

Thus, within the circle with the radius $r_0 = w(z)$ beam carries $(1 - 1/e^2)$ or approximately 86% of its total power at any beam cross section. This allows to call the function $w(z)$ the **beam radius** or the **spot radius**.

By separating real and imaginary part of the complex-valued q -parameter, we obtain the following expression:

$$q(z) = z - z_0 + i z_R. \quad (3.15)$$

Combining this representation with the previously given in equation (3.7), we can derive the expression for the beam radius evolution [18]:

$$w(z) = w_0 \sqrt{1 + \left(\frac{z - z_0}{z_R}\right)^2}, \quad (3.16)$$

where

$$w_0 = \sqrt{\frac{\lambda z_R}{\pi}}. \quad (3.17)$$

We can see that w_0 is the minimum value of the beam radius that is reached when $z = z_0$. Therefore the parameter w_0 is called the **waist radius** and z_0 is called **waist position**. The beam radius increases monotonously with the increase of the distance from waist $|z - z_0|$. The value z_R is called the **Rayleigh range**. It is the distance from waist along the beam axis where the beam width increases by a factor of $\sqrt{2}$ with respect to the waist. The evolution of the beam width is illustrated in Figure 3.1.

As z approaches infinity the first term of equation (3.16) may be neglected. Then this equation transforms into the linear relation

$$w(z) \approx \frac{w_0}{z_R} (z - z_0) \quad (3.18)$$

and the beam diverges as a cone of half angle

$$\Theta = \frac{w_0}{z_R}. \quad (3.19)$$

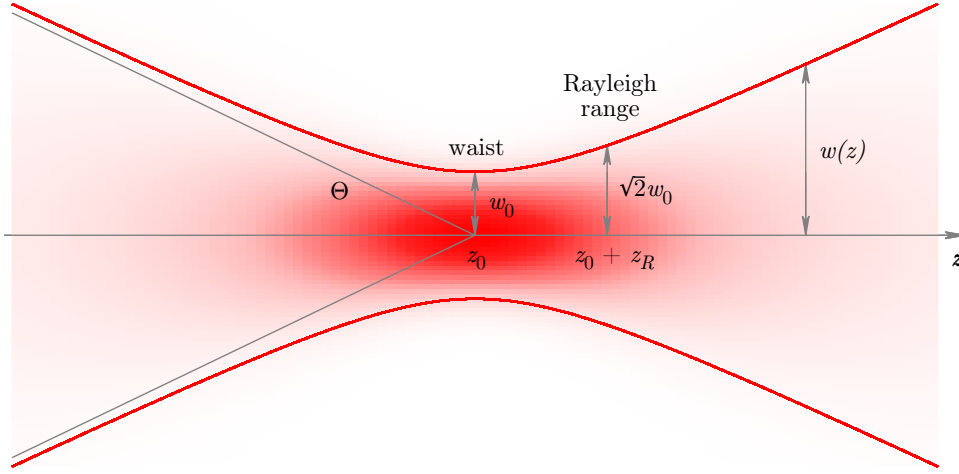


Figure 3.1.: The evolution of beam radius of a stigmatic Gaussian beam. The waist is reached at the point z_0 and has the radius of w_0 . At distance z_R from the beam waist the beam radius increases by a factor of $\sqrt{2}$. The beam divergence in the far field is illustrated with the grey lines and has the half-angle Θ . The irradiance distribution of the stigmatic Gaussian beam is shown with the points of corresponding brightness of red color.

This angle is often called the beam **divergence** and it is the far field diffraction angle of the stigmatic Gaussian beam (see Figure 3.1). From equation (3.17) it follows that

$$z_R = \frac{w_0^2 \pi}{\lambda}. \quad (3.20)$$

Then the divergence can be expressed as

$$\Theta = \frac{\lambda}{w_0 \pi}. \quad (3.21)$$

Equation (3.21) implies that the beams with larger waist radius have smaller divergence and vice versa. Therefore the good collimation (small divergence) can only be reached with wide beams.

On the beam axis intensity reduces to:

$$I(0, z) = \frac{2P}{\pi w^2}, \quad (3.22)$$

which is the maximum value of the intensity in each of the transversal planes. When additionally $z = z_0$, we are at the location of greatest intensity, where

$$I(0, 0) = 2P/(\pi w_0^2). \quad (3.23)$$

The intensity distribution is illustrated in Figure 3.1.

3.3. Phase distribution

According to equation (3.12) the phase of stigmatic Gaussian beam is

$$\phi(r, z) = \phi_{\text{ac}} - \eta(z) + \frac{kr^2}{2R(z)}. \quad (3.24)$$

The first term, **accumulated phase** ϕ_{ac} , is the phase of the plane wave. As beam propagates through the optical system from the chosen reference point, it accumulates phase as

$$\phi_{\text{ac}} = \sum_i k_i l_i, \quad (3.25)$$

where k_i and is the wavenumber and l_i is the geometrical propagation distance in each of the media that the beam is propagated through. The **accumulated optical pathlength** is computed as

$$s_{\text{ac}} = \sum_i n_i l_i, \quad (3.26)$$

where n_i is the refractive index of each of the media that the beam went through. Since the wavenumber in the medium k and wavenumber in vacuum k_v are connected as

$$k = nk_v, \quad (3.27)$$

the accumulated phase and the accumulated optical pathlength can be transformed into each other using the following equation:

$$\phi_{\text{ac}} = k_v s_{\text{ac}}. \quad (3.28)$$

Thus accumulated phase in equation (3.24) can be replaced by the term $k_v s_{\text{ac}}$. Often the term $k(z - z_0)$ with the distance from waist is used instead. However, such a notation takes into account only the local beam segment and neglects the rest of the beam path.

The second term of the phase is a **Gouy phase shift** (see for example [20, p. 682]) with the value of

$$\eta(z) = \arctan\left(\frac{z - z_0}{z_R}\right). \quad (3.29)$$

It gives an additional cumulative phase shift of $\pm\pi/2$ on either side of the waist with most of this shift occurring within one or two Rayleigh ranges from the waist. This added phase shift can be interpreted as the small decrease of the effective wavenumber in the waist region:

$$k_{\text{eq}}(z) = k - \Delta k, \quad (3.30)$$

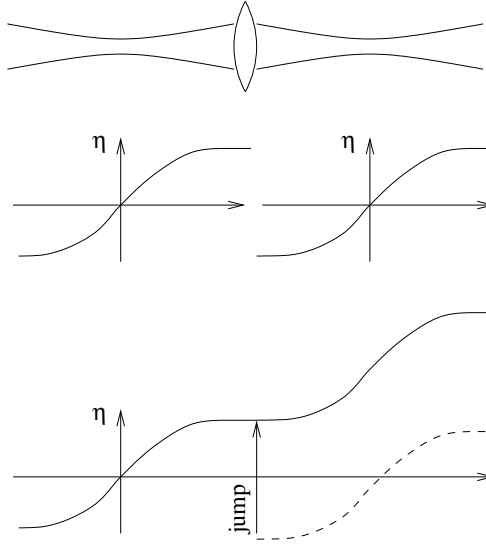


Figure 3.2.: Gouy phase jumps at the interface. Credit: IfoCad manual [21]

or the increase of spacing between the wavefronts with respect to the ideal plane wave.

Beam transformations on surfaces can result in unphysical jumps in the phase shift $\eta(z)$. In order to avoid those the Gouy phase can be computed as

$$\eta_{\text{sum}}(z) = \eta(z) + \eta_{\text{ac}}, \quad (3.31)$$

where $\eta(z)$ is the Gouy phase of the local beam segment (see equation (3.29)) and η_{ac} is accumulated as the beam propagates through the optical system [P2]. The latter term can be found by adding up the **Gouy phase jumps** η_{jump} at each beam transformation:

$$\eta_{\text{jump}} = \eta_i - \eta_t, \quad (3.32)$$

where η_i and η_t are the Gouy phases of the incident beam and the refracted beams at the surface (see Figure 3.2).

The third phase contribution is responsible for the wavefront bending [17]. The value $R(z)$ is the radius of curvature of the wavefront. Equations (3.7) and (3.15) imply that its evolution can be represented as

$$R(z) = z - z_0 + \frac{z_R^2}{z - z_0}. \quad (3.33)$$

At waist ($z = z_0$) the radius of curvature of the wavefront is infinite and the wavefront is planar. The maximum curvature of the wavefront ($1/R(z)$) is reached at the Rayleigh range and is equal to $1/(2z_R)$. As z approaches infinity the radius

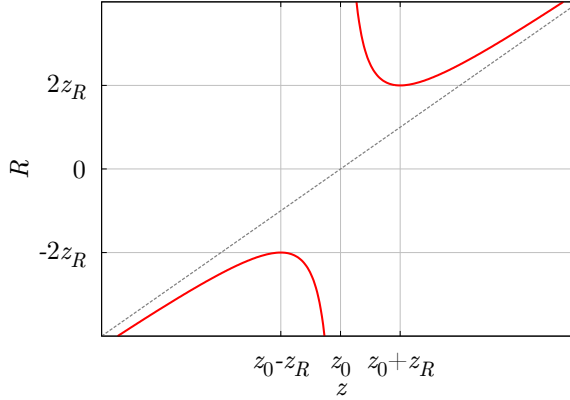


Figure 3.3.: The evolution of radius of curvature of wavefront of a stigmatic Gaussian beam. It reaches its minimum of absolute value at the Rayleigh range ($z_0 \pm z_R$). At waist the wavefront is planar. The grey line is a radius of curvature of a spherical wave.

of curvature of the wavefront $R(z)$ becomes close to its linear term (the distance from waist $z - z_0$) and the wavefronts become approximately the same as those of a spherical wave.

3.4. Beam propagation

The propagation of the stigmatic Gaussian beam has already been described in the expression for the complex amplitude given in equation (3.8). However, in simulations we are not interested in the entire beam evolution as z goes from $-\infty$ to $+\infty$. Normally we have the beam that propagates through the optical setup and we are interested in beam parameters at different points along the beam path. The beam traveling from the reference point to the photodiode usually consists of several beam segments with different beam parameters. Thus, when we talk about beam propagation through the optical system we talk about set of transformations of beam parameters. If the beam parameters are known at a specific point on a beam path and then the beam propagates through a homogeneous medium by a distance Δz to the next point of interest, the q -parameter of the beam transforms as

$$q' = q + \Delta z. \quad (3.34)$$

The accumulated optical pathlength is then increased by the geometrical propagation distance Δz multiplied by the refractive index of the medium n

$$s'_{\text{ac}} = s_{\text{ac}} + n\Delta z. \quad (3.35)$$

The accumulated phase is incremented as

$$\phi'_{\text{ac}} = \phi_{\text{ac}} + k\Delta z, \quad (3.36)$$

where k is the wavenumber in the medium.

Other parameters of the beam, such as beam radius $w(z)$, radius of curvature of the wavefront $R(z)$ and the Gouy phase $\eta(z)$ should then be recomputed according to the new value of q -parameter using equations (3.16), (3.33), (3.29).

3.5. Beam transformation

The beam transformation on a surface via reflection and refraction includes the transformation of q -parameter. The phase and optical pathlength are not accumulated in this case. The Gouy phase accumulates a jump as explained in Section 3.3.

The stigmatic beam remains stigmatic only in case of normal incidence on a flat or spherical surface. Therefore within this model we assume that any surface can be described by a single curvature c_S . Then the required expressions for transformation of q parameters as the stigmatic beam is reflected or refracted at some interface can be obtained from the formulas suggested in [9] by considering normal incidence on a spherical surface:

$$q_r = \frac{q_i}{2c_S q_i + 1}, \quad (3.37)$$

$$q_t = \frac{q n_t}{(n_i - n_t)c_S q_i + n_i}. \quad (3.38)$$

Here q_r and q_t are the q -parameters of reflected and refracted (transmitted) beams, n_i and n_t are the refractive indices of the mediums before and after refraction. The beam transmission through a dual surface optical component (such as thick lens or beamsplitter) can be split up into two refractions on each of the surfaces of the component. Between these two refractions beam propagates inside the component and its parameters are changed as described in the previous section. This approach is particularly useful for the thick lenses. It also allows to be more flexible and look at beam parameters not only before or after the beam enters the lens or beamsplitter, but also inside.

The formulae that allow to transform the stigmatic beam on a surface provided in this section complete the description of the stigmatic Gaussian beam model. Together with the description of beam tracing and signal computation provided in chapter 2 suggested model allows to simulate laser interferometers with the assumption that all surfaces in the optical system are planar or spherical and the beam incidence on a surface is always close to normal.

Simple astigmatic Gaussian beam

THIS chapter is dedicated to simple astigmatic Gaussian beams. The other name that can be found in literature is orthogonal astigmatic beams [7]. Such beams have elliptical light spots and ellipsoidal wavefronts at every point along the propagation. Circular light spots as well as spherical wavefronts are only achieved in few specific points. The orientation of light spot coincides with the orientation of wavefronts, and both orientations remain unchanged as the beam propagates through a homogeneous medium. Therefore, such beams have two planes of symmetry, corresponding to the principal semi-axes of the light spot or the wavefront. Simple astigmatic beams can be modeled by introducing two independent stigmatic Gaussian beam representations – one for each plane of symmetry of the beam [22]. Therefore, a significant part of the description of these beams is connected to the description of circular Gaussian beams provided in Chapter 3. The beam-fixed coordinate system (see Chapter 2) does not necessarily coincide with the beam principal coordinate system, given by the beam direction and the two planes of symmetry of the beam. Then additionally the angle between these coordinate systems has to be introduced.

The simple astigmatic Gaussian beam model (unlike the stigmatic model) allows non-normal incidence on a surface. However, this model is also not general. It is limited to a propagation through the **orthogonal optical system**. In such an optical system for every transformation of the simple astigmatic beam at a surface the plane of incidence has to include one of the axes of symmetry of both the beam and the surface. Otherwise the transformation cannot be decoupled into two orthogonal planes and the simple astigmatic model can only be used as a simplification.

The description of the simple astigmatic Gaussian beam model will include the same four aspects as the description of circular Gaussian beam model, namely the complex amplitude of the electric field, intensity and phase distributions, the law of

propagation and the laws of beam transformation via reflection and refraction.

4.1. Complex amplitude of the electric field

The complex amplitude of a simple astigmatic beam (as well as the complex amplitude of stigmatic beam) can be expressed by the equation for the complex amplitude of a paraxial wave (equation (3.3)), where the complex envelope $\Psi(\mathbf{r}, z)$ is a generalization of the **complex envelope** of stigmatic Gaussian beam:

$$\Psi(\mathbf{r}, z) = E_0(z) \exp \left[-ik \left(\frac{x^2}{2q_1(z)} + \frac{y^2}{2q_2(z)} \right) \right]. \quad (4.1)$$

Such generalization remains the solution of the paraxial Helmholtz equation (3.4). Substituting this expression into equation (3.3), we obtain the complex amplitude of the electric field of a simple astigmatic beam:

$$E(\mathbf{r}, z) = E_0(z) \exp \left[-i\phi_{ac} + i\eta(z) - ik \left(\frac{x^2}{2q_1(z)} + \frac{y^2}{2q_2(z)} \right) \right]. \quad (4.2)$$

Similarly to the stigmatic case, here ϕ_{ac} is the phase accumulated from the chosen reference point, $\mathbf{r} = (x, y)$ is a vector of transversal coordinates and the q -parameters can be interpreted as

$$\frac{1}{q_i(z)} = \frac{1}{R_i(z)} - i \frac{\lambda}{\pi w_i^2(z)}, \quad i = 1, 2, \quad (4.3)$$

where $R_i, i = 1, 2$ are the principal radii of curvature of the wavefront and w_i are the principal semi-axes of the light spot ellipse. An alternative representation of the q -parameters is

$$q_i(z) = z - z_{0i} + iz_{Ri}, \quad i = 1, 2, \quad (4.4)$$

where z_{0i} is the waist position and z_{Ri} is the Rayleigh range in the corresponding plane of symmetry.

The **Gouy phase** $\eta(z)$ for simple astigmatic beams is the average of the Gouy phases in two planes of symmetry [8]:

$$\eta(z) = \frac{1}{2} \left[\arctan \left(\frac{z - z_{01}}{z_{R1}} \right) + \arctan \left(\frac{z - z_{02}}{z_{R2}} \right) \right]. \quad (4.5)$$

In order to keep the Gouy phase continuous the same procedure as described in Chapter 3 has to be performed to accumulate the Gouy phase jumps as beam propagates through the optical system.

The normalization constant $E_0(z)$ can again be computed using the fact that the integral of optical intensity over the entire transversal plane equals to the beam power:

$$P = \int_{-\infty}^{+\infty} \int_{-\infty}^{+\infty} I(\mathbf{r}, z) dx dy = \int_{-\infty}^{+\infty} \int_{-\infty}^{+\infty} |E(\mathbf{r}, z)|^2 dx dy. \quad (4.6)$$

This integral can be computed using the **Euler-Poisson (or Gaussian) integral**:

$$\int_{-\infty}^{\infty} e^{-x^2} dx = \sqrt{\pi}. \quad (4.7)$$

Then the normalization constant can be expressed as

$$E_0(z) = \sqrt{\frac{Pk}{\pi}} \sqrt{\frac{z_{R1} z_{R2}}{((z - z_{01})^2 + z_{R1}^2)((z - z_{02})^2 + z_{R2}^2)}} = \sqrt{\frac{Pk \sqrt{z_{R1} z_{R2}}}{\pi |q_1 q_2|}} \quad (4.8)$$

The resulting expression for the complex amplitude of the electric field is

$$E(\mathbf{r}, z) = \sqrt{\frac{Pk \sqrt{z_{R1} z_{R2}}}{\pi |q_1 q_2|}} \exp \left[-i\phi_{ac} + i\eta(z) - ik \left(\frac{x^2}{2q_1(z)} + \frac{y^2}{2q_2(z)} \right) \right]. \quad (4.9)$$

If we compare the last equation to equation (3.12) when $q_1 = q_2 = q$, we will obtain the same results, which allows considering the stigmatic Gaussian beam to be the special case of simple astigmatic Gaussian beam.

Let us now consider the case when the **principal coordinate system of the beam** $(\hat{x}', \hat{y}', \hat{z})$ is tilted with respect to the chosen beam-fixed coordinate system $(\hat{x}, \hat{y}, \hat{z})$ counter-clockwise by an angle of θ around the beam axis \hat{z} . Then the coordinate transformation from the beam-fixed coordinate system into the principal beam coordinate system looks as (see Figure 4.1)

$$\begin{aligned} x' &= x \cos \theta + y \sin \theta, \\ y' &= -x \sin \theta + y \cos \theta. \end{aligned} \quad (4.10)$$

The complex envelope $\Psi(x', y', z)$ in the beam principal coordinate system is defined in equation (4.1). Substituting coordinate transformation given in equation (4.10) into this equation, we obtain the complex envelope in the beam-fixed coordinate system:

$$\Psi(\mathbf{r}, z) = E_0(z) \exp \left\{ -i\frac{k}{2} \left[\left(\frac{\cos^2 \theta}{q_1(z)} + \frac{\sin^2 \theta}{q_2(z)} \right) x^2 + \left(\frac{\sin^2 \theta}{q_1(z)} + \frac{\cos^2 \theta}{q_2(z)} \right) y^2 + \sin 2\theta \left(\frac{1}{q_1(z)} - \frac{1}{q_2(z)} \right) xy \right] \right\}. \quad (4.11)$$

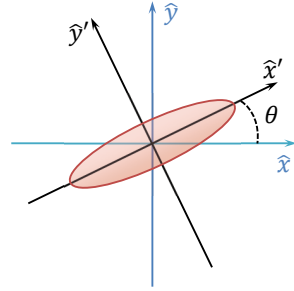


Figure 4.1.: The principal coordinate system (\hat{x}', \hat{y}') of a simple astigmatic Gaussian beam tilted counter clockwise by an angle θ with respect to its beam-fixed coordinate system (\hat{x}, \hat{y}) .

Using this expression together with equation (3.3) and the value of the normalization constant given in equation (4.8), the complex amplitude of the electric field in the beam-fixed coordinate system is defined as

$$E(\mathbf{r}, z) = \sqrt{\frac{Pk\sqrt{z_{R1}z_{R2}}}{\pi|q_1q_2|}} \exp \left\{ -i\phi_{ac} + i\eta(z) - i\frac{k}{2} \left[\left(\frac{\cos^2 \theta}{q_1(z)} + \frac{\sin^2 \theta}{q_2(z)} \right) x^2 + \left(\frac{\sin^2 \theta}{q_1(z)} + \frac{\cos^2 \theta}{q_2(z)} \right) y^2 + \sin 2\theta \left(\frac{1}{q_1(z)} - \frac{1}{q_2(z)} \right) xy \right] \right\}. \quad (4.12)$$

The terms $i\phi_{ac}$ and $i\eta(z)$ stay unaffected in this coordinate transformation. The expression for complex amplitude of electric field on the beam axis ($x = y = 0$) also does not depend on value of θ .

The beam-fixed coordinate system can always be chosen such that it coincides with the beam principal coordinate system and thus its transversal axes are aligned with the principal semi-axes of the beam ellipse. Then equation (4.9) can be used in the signal computation for laser interferometer simulations. If the other choice of the beam-fixed coordinate system is necessary for some purposes, the angle θ has to be introduced and equation (4.12) has to be used as the expression for complex amplitude of electric field.

4.2. Intensity and phase distribution

Since the representation of simple astigmatic beam can be split into two independent circular representations, the description of configuration of such beams comprises the description of the circular beam configuration. Simple astigmatic beam has two waists – one in each of the planes of symmetry, not necessarily at one point on the beam axis (see Figure 4.2). Therefore it can be characterized by two independent sets of parameters, each including waist position, waist radius and Rayleigh range. These parameters allow to compute two **beam radii** and two **radii of curvature of the wavefront** using equations, identical to those for the stigmatic beam:

$$w_i(z) = w_{0i} \sqrt{1 + \left(\frac{z - z_{0i}}{z_{Ri}} \right)^2}, \quad (4.13)$$

$$w_{0i} = \sqrt{\frac{\lambda z_{Ri}}{\pi}}, \quad (4.14)$$

$$R_i(z) = z - z_{0i} + \frac{z_{Ri}^2}{z - z_{0i}}, \quad i = 1, 2. \quad (4.15)$$

These dependancies are illustrated in Figure 4.3. In Figure 4.3a we can see that simple astigmatic beam has elliptic intensity profile at every transversal plane along the propagation, except for the two planes, where beam radii are the same in XZ and

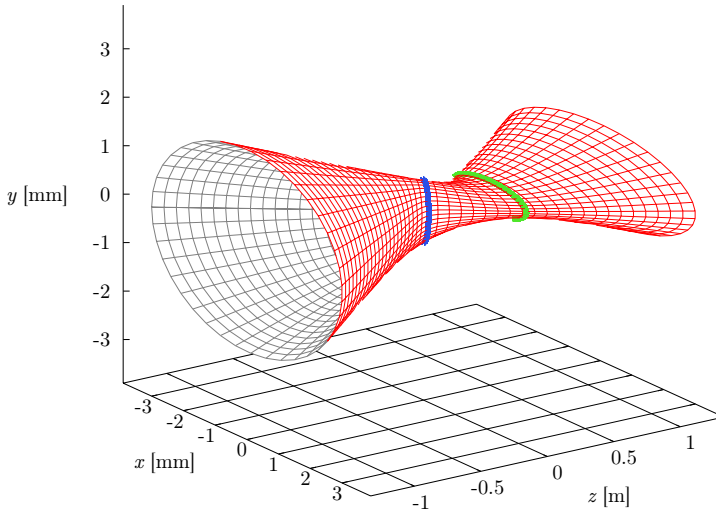


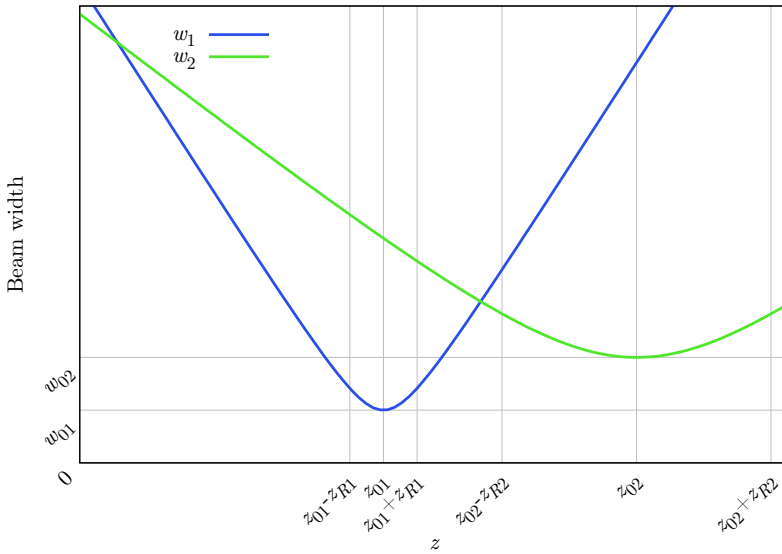
Figure 4.2.: Simple astigmatic Gaussian beam. Beam width evolution. Beam principal planes coincide with the planes XZ and YZ . Waist in XZ -plane: $w_{0x} = 0.15$ mm $z_{0x} = 0$ m, represented by blue line. Waist in YZ -plane: $w_{0y} = 0.3$ mm $z_{0y} = 0.5$ m, represented by green line. Equivalent q -parameters: $q_1 = i66$ mm, $q_2 = -500 + i266$ mm at $z = 0$. The wavelength $\lambda = 1064$ nm.

YZ planes. The ellipticity of the irradiance pattern changes along the propagation and the larger semi-axis switches from one plane to another every time the circular intensity profile is reached. However, the orientation of the light spot stays the same as beam propagates in free space.

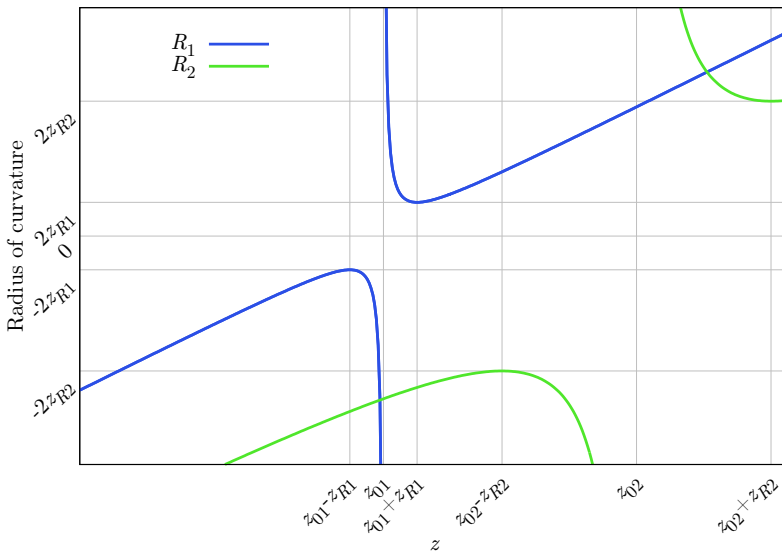
In Figure 4.3b the evolution of the two principal radii of curvature is presented. The wavefront of the simple astigmatic beam can be described by a paraboloid having two planes of symmetry [19]. The exceptions are the two intersection points where the wavefront is spherical. It is important to note that the points where the irradiance pattern is circular do not coincide with the positions of spherical wavefront.

4.3. Beam propagation

The propagation of simple astigmatic beams is similar to the propagation of stigmatic beams. The geometrical propagation distance Δz should be added to each of the q -parameters, while the optical pathlength requires multiplication of this distance by the value of the refractive index:



(a) Beam width evolution.



(b) Radius of curvature of the wavefront evolution.

Figure 4.3.: Simple astigmatic Gaussian beam. Beam width evolution (a) and radii of curvature of the wavefront evolution (b). Blue line corresponds to XZ plane, green line corresponds to YZ plane. The intersection points on the left-hand side correspond to the circular patterns of irradiance. The intersection points on the right-hand side correspond to the spherical wavefronts. Both conditions are not fulfilled simultaneously.

$$q'_1 = q_1 + \Delta z, \quad (4.16)$$

$$q'_2 = q_2 + \Delta z, \quad (4.17)$$

$$s'_{ac} = s_{ac} + n\Delta z, \quad (4.18)$$

$$\phi'_{ac} = \phi_{ac} + k\Delta z. \quad (4.19)$$

The orientation of the beam θ doesn't change along the propagation. Other parameters of the beam have to be recomputed according to the new values of the q -parameters.

4.4. Beam transformation

Beam transformation within the simple astigmatic model is only possible when it can be decoupled into two separate transformations: one for each of the circular Gaussian beam representations that make up the simple astigmatic beam representation. The laws of reflection and refraction will be obtained in the form of **ABCD-law** for both q -parameters:

$$q' = \frac{Aq + B}{Cq + D} \quad (4.20)$$

Following the approach suggested in [9], we will use the fact that the arguments of the complex amplitudes (equation (4.9)) of the incident, reflected and refracted beams must match exactly on the boundary between the two media. Due to their complex values, we shall call these arguments the **complex phases** to distinguish from the real-valued beam phase:

$$\psi(x, y, z) = -i\phi_{ac} + i\eta(z) - ik \left(\frac{x^2}{2q_1(z)} + \frac{y^2}{2q_2(z)} \right). \quad (4.21)$$

In our investigations we will restrict ourselves to the case where a simple astigmatic beam is incident on an ellipsoidal interface, defined as

$$(x^2 + z^2)/A^2 + y^2/B^2 = 1. \quad (4.22)$$

We will assume that this surface is a boundary between two media with refractive indices n_i and n_t . The beam is incident on a surface at an arbitrary angle θ_i . The reflected angle θ_r is identical to the angle of incidence (following the reflection law (2.2)). The refracted angle θ_t is defined according to the Snell's law given in equation (2.3). The plane of incidence, as before, is defined by the direction of the incoming beam \hat{z}_i and the surface normal \hat{n} at the point of incidence. From the reflection and refraction laws it follows that both directions of the outgoing beams (\hat{z}_r and \hat{z}_t) also lie in the plane of incidence.

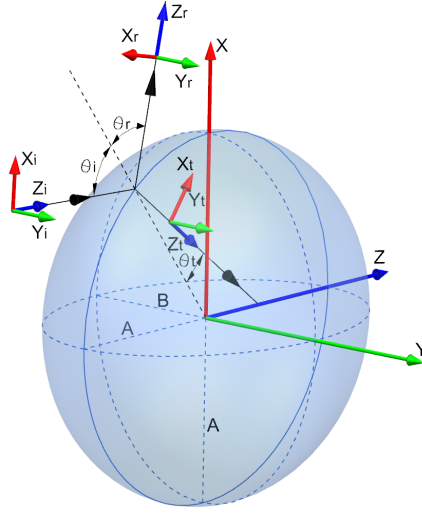


Figure 4.4.: Reflection and refraction of a simple astigmatic Gaussian beam at an ellipsoidal surface. XZ is the plane of incidence. $(\hat{x}_i, \hat{y}_i, \hat{z}_i)$, $(\hat{x}_r, \hat{y}_r, \hat{z}_r)$, $(\hat{x}_t, \hat{y}_t, \hat{z}_t)$ – beam-fixed coordinate systems for incident, reflected and transmitted beams correspondingly. x_l, z_l lie in plane of incidence for $l = i, r, t$.

The beam-fixed coordinate systems ($(\hat{x}_i, \hat{y}_i, \hat{z}_i)$ for the incident beam, $(\hat{x}_t, \hat{y}_t, \hat{z}_t)$ for the refracted (transmitted) beam, $(\hat{x}_r, \hat{y}_r, \hat{z}_r)$ for the reflected beam) must be the principal coordinate systems of the beams. In our derivations we will assume that the transversal vector $\hat{x}_l, l = i, r, t$ corresponds to the first q -parameter of each of the three beams $q_{1l}, l = i, r, t$. Then the complex amplitude of electric field for each of the three beams is given in a form of equation (4.9). All coordinate systems have their origins at the point of incidence. The propagation to the point of incidence for the incident beam and from the point of incidence for reflected and transmitted beams should be performed separately using the formulas from the previous section.

In order to make sure that both outgoing beams (reflected and refracted) are simple astigmatic, we have to introduce several restrictions:

1. one of the principal axes of ellipsoidal surface must lie in the plane of incidence; this restriction is not an issue with spherical or planar surfaces; in our investigations we will assume that the incidence happens in the XZ -plane (see Figure 4.4);
2. the incident simple astigmatic Gaussian beam must be oriented such that one of its principal axes lies in the plane of incidence; in our derivations we will assume that \hat{x}_i lies in the plane of incidence; this restriction cannot be violated if the incident beam is stigmatic;
3. the beam diameter is always small compared to both the radius of curvature of the optical wavefront and the radius of curvature of the optical surface; we

consider, at most, quadratic variations of the wavefront phase and amplitude along the transversal coordinates.

We call any optical system, where each beam transformation satisfies the first two of the restrictions above, an **orthogonal optical system**. This definition implies that in such an optical system each beam transformation can be performed separately for each of the planes of symmetry of the beam. Therefore, it is identical to the definition given in [23, p. 234].

If \hat{x}_i lies in the plane of incidence, according to the transversal coordinate transformation (2.4) both \hat{z}_r and \hat{z}_t also lie in the plane of incidence. An illustration is given in Figure 4.4.

In the plane of incidence (XZ -plane) the surface given in equation (4.22) is represented as $x^2 + z^2 = A^2$, so the radius of curvature of the surface is $R_I = A$. In the other principal plane of the surface (YZ -plane), orthogonal to the plane of incidence, the surface equation reduces to $y^2/B^2 + z^2/A^2 = 1$, which means that the radius of curvature of the surface in this plane is $R_S = B^2/A$ for sufficiently small values of y . We assume that positive radii of curvature of the surface correspond to a convex surface facing the incident beam.

Matching the complex phases of the incident, reflected and refracted beams on the interface, we obtain

$$\psi_i(x_i, y_i, z_i) = \psi_r(x_r, y_r, z_r), \quad (\text{reflection}) \quad (4.23)$$

$$\psi_i(x_i, y_i, z_i) = \psi_t(x_t, y_t, z_t). \quad (\text{refraction}) \quad (4.24)$$

In our derivations we will not include the Gouy phase $\eta(z)$. It is kept continuous separately by accumulating phase jumps as explained in Chapter 3. The accumulated phase ϕ_{ac} can be represented as

$$\phi_{ac}(z_l) = \bar{\phi}_{ac} + k_l z_l, \quad l = i, r, t, \quad (4.25)$$

where $\bar{\phi}_{ac}$ is the phase accumulated before the current transformation. This term is identical for all three beams. Therefore, only the term $k_l z_l$ will be included in the comparison.

The complex phases are given in the corresponding beam-fixed coordinate systems and the surface equation is given in the global coordinate system. In order to obtain the complex phase on the surface, we can rewrite surface equation 4.22 in the beam fixed coordinate system of the incident beam, using the following coordinate transformation:

$$\begin{aligned} x &= x_i + A \sin \theta_i, \\ y &= y_i, \\ z &= z_i - A \cos \theta_i. \end{aligned} \quad (4.26)$$

Equation (4.22) becomes

$$(x_i + A \sin \theta_i)^2 + (Ay_1/B)^2 + (z_i - A \cos \theta_i)^2 = A^2. \quad (4.27)$$

Solving this equation for z_i accurately to second order in transversal variables x_i and y_i , we obtain:

$$z_i \approx x_i \tan \theta_i + \frac{x_i^2}{2R_I \cos^3 \theta_i} + \frac{y_i^2}{2R_S \cos \theta_i}. \quad (4.28)$$

Substituting this into the complex phase (equation (4.25)) gives:

$$\psi_i(x_i, y_i) = k_i x_i \tan \theta_i + \frac{k_i x_i^2}{2} \left(\frac{1}{q_{1i}} + \frac{1}{R_I \cos^3 \theta_i} \right) + \frac{k_i y_i^2}{2} \left(\frac{1}{q_{2i}} + \frac{1}{R_S \cos \theta_i} \right) \quad (4.29)$$

4.4.1. Reflection

In order to compare the complex phases in equation (4.23) we need to rewrite the complex phase of the reflected beam in the beam-fixed coordinate system of the incident beam using the following coordinate transformation

$$\begin{aligned} x_r &= -x_i \cos 2\theta_i - z_i \sin 2\theta_i, \\ y_r &= y_i, \\ z_r &= x_i \sin 2\theta_i - z_i \cos 2\theta_i \end{aligned} \quad (4.30)$$

and the expression for z_i (equation (4.28)). Taking into account that incident and reflected beams propagate in one medium ($k_i = k_r$), the complex phase of the reflected beam becomes

$$\begin{aligned} \psi_r(x_i, y_i) &= k_i x_i \tan \theta_i + \frac{k_i x_i^2}{2} \left(\frac{1}{q_{1r}} + \frac{1 - 2 \cos^2 \theta_i}{R_I \cos^3 \theta_i} \right) \\ &\quad + \frac{k_i y_i^2}{2} \left(\frac{1}{q_{2r}} + \frac{1 - 2 \cos^2 \theta_i}{R_S \cos \theta_i} \right). \end{aligned} \quad (4.31)$$

The linear terms in equations (4.29) and (4.31) match. Equating coefficients of x_i^2 and y_i^2 , we obtain the relationship between reflected and incident q -parameters:

$$\frac{1}{q_{1r}} = \frac{1}{q_{1i}} + \frac{2}{R_I \cos \theta_i}, \quad (\text{plane of incidence}) \quad (4.32)$$

$$\frac{1}{q_{2r}} = \frac{1}{q_{2i}} + \frac{2 \cos \theta_i}{R_S}. \quad (\text{sagittal plane}) \quad (4.33)$$

From these equations it follows that the spot sizes are identical for incident and reflected beams on the surface. The wavefront radii of curvature are connected by the relationship

$$\begin{aligned} \frac{1}{R_{1r}} &= \frac{1}{R_{1i}} + \frac{2}{R_I \cos \theta_i} \\ \frac{1}{R_{2r}} &= \frac{1}{R_{2i}} + \frac{2 \cos \theta_i}{R_S}. \end{aligned} \quad (4.34)$$

Rewriting equations (4.32) and (4.33) in the form of ABCD-law (4.20), we get the following expressions for the ABCD matrices for each of the q -parameters:

$$ABCD_1 = \begin{pmatrix} 1 & 0 \\ \frac{2}{R_I \cos \theta_i} & 1 \end{pmatrix}, \quad ABCD_2 = \begin{pmatrix} 1 & 0 \\ \frac{2 \cos \theta_i}{R_S} & 1 \end{pmatrix}. \quad (4.35)$$

4.4.2. Refraction

Similarly we can obtain the equations for refracted beam. The beam-fixed coordinate system of refracted beam can be transformed into the beam-fixed coordinate system of incident beam as

$$\begin{aligned} x_t &= x_i \cos(\theta_i - \theta_t) + z_i \sin(\theta_i - \theta_t), \\ y_t &= y_i, \\ z_t &= -x_i \sin(\theta_i - \theta_t) + z_i \cos(\theta_i - \theta_t). \end{aligned} \quad (4.36)$$

Using this coordinate transformation together with expression for z_i given in equation (4.28), we obtain the expression for complex phase of the refracted beam:

$$\begin{aligned} \psi_t(x_i, y_i) &= k_t x_i [\tan \theta_i \cos(\theta_i - \theta_t) - \sin(\theta_i - \theta_t)] \\ &+ \frac{k_t x_i^2}{2} \left(\frac{\cos^2 \theta_t}{\cos^2 \theta_i} \frac{1}{q_{1t}} + \frac{\cos(\theta_i - \theta_t)}{R_I \cos^3 \theta_i} \right) \\ &+ \frac{k_t y_i^2}{2} \left(\frac{1}{q_{2t}} + \frac{\cos(\theta_i - \theta_t)}{R_S \cos \theta_i} \right) \end{aligned} \quad (4.37)$$

The wavenumbers of incident and refracted beams are related as $k_t/k_i = n_t/n_i = n_r$. Equating linear terms of equations (4.29) and (4.37) confirms the Snell's law (2.3). Equating coefficients of quadratic terms x_i^2 and y_i^2 and using Snell's law to eliminate θ_t , we obtain both q -parameters of the simple astigmatic refracted beam:

$$\frac{1}{q_{1t}} = \frac{n_r \cos^2 \theta_i}{n_r^2 - \sin^2 \theta_i} \frac{1}{q_{1i}} + \frac{n_r}{R_I} \frac{\cos \theta_i - \sqrt{n_r^2 - \sin^2 \theta_i}}{n_r^2 - \sin^2 \theta_i} \quad (\text{plane of incidence}), \quad (4.38)$$

$$\frac{1}{q_{2t}} = \frac{1}{n_r} \frac{1}{q_{2i}} + \frac{\cos \theta_i - \sqrt{n_r^2 - \sin^2 \theta_i}}{n_r R_S} \quad (\text{sagittal plane}). \quad (4.39)$$

In this case spot size remains unchanged only in sagittal plane, while for tangential it changes as

$$w_{1t} = \frac{\sqrt{n_r^2 - \sin^2 \theta_i}}{n_r \cos \theta_i} w_{1i}. \quad (4.40)$$

The radii of curvature of the wavefront are given by the following relations:

$$\begin{aligned}\frac{1}{R_{1t}} &= \frac{n_r \cos^2 \theta_i}{n_r^2 - \sin^2 \theta_i} \frac{1}{R_{1i}} + \frac{n_r}{R_I} \frac{\cos \theta_i - \sqrt{n_r^2 - \sin^2 \theta_i}}{n_r^2 - \sin^2 \theta_i}, \\ \frac{1}{R_{2t}} &= \frac{1}{n_r} \frac{1}{R_{yi}} + \frac{\cos \theta_i - \sqrt{n_r^2 - \sin^2 \theta_i}}{n_r R_S}.\end{aligned}\tag{4.41}$$

Now we can rewrite equations (4.38) and (4.39) in the form of ABCD-law (4.20). Then the ABCD matrices for each of the q -parameters are given as:

$$ABCD_1 = \begin{pmatrix} \frac{\sqrt{n_r^2 - \sin^2 \theta_i}}{n_r \cos \theta_i} & 0 \\ \frac{\cos \theta_i - \sqrt{n_r^2 - \sin^2 \theta_i}}{R_I \cos \theta_i \sqrt{n_r^2 - \sin^2 \theta_i}} & \frac{\cos \theta_i}{\sqrt{n_r^2 - \sin^2 \theta_i}} \end{pmatrix},\tag{4.42}$$

$$ABCD_2 = \begin{pmatrix} 1 & 0 \\ \frac{\cos \theta_i - \sqrt{n_r^2 - \sin^2 \theta_i}}{R_S n_r} & \frac{1}{n_r} \end{pmatrix}.\tag{4.43}$$

With this the description of the simple astigmatic Gaussian beam model is completed.

General astigmatic Gaussian beam

IN this chapter I will introduce the most general case of the Gaussian beam in fundamental mode, namely the general astigmatic Gaussian beam. Understanding simple astigmatism is relatively simple for those who are familiar with stigmatic Gaussian beam. Single circular beam representation in this case is replaced by the two circular beam representations, and instead of circular light spots and spherical wavefronts we get elliptical intensity patterns and ellipsoidal wavefronts. In case of general astigmatism one will still see elliptical light spots and ellipsoidal wavefronts as beam propagates in free space. However, both ellipses of constant intensity and ellipses of constant phase will not preserve their orientation along the propagation. Moreover, the elliptical light spots will not have the same orientation as the ellipsoidal wavefront at any point along the beam axis. Their relative orientation will also change as beam propagates. These physical properties make general astigmatic beam and its mathematical description significantly more complex than simple astigmatic beam. The behavior of such beams cannot be decoupled into two (or more) stigmatic beam representations.

General astigmatic beam model allows arbitrary transformations of Gaussian beam in the fundamental mode on the second order surface (or the surface that can be locally approximated with the second order equation at the point of incidence). Therefore, it allows to study the beam jitter effects in the misaligned optical systems or in optical systems that contain surfaces other than planar or spherical, for example cylindrical lenses.

General astigmatic Gaussian beams have been known for decades. They were introduced and described by Arnaud and Kogelnik [8]. However, in the field of optical simulations they are still rarely used. Many software tools that are used in laser interferometry simulations assume on-axis beam transformations. In this case the

majority of optical systems that are of interest for the scientists are orthogonal. The example of set of on-axis beam transformations that leads to the general astigmatism is the optical system that contains two cylinder lenses, oriented at an oblique angle with respect to each other in the transversal plane. Similar optical systems are not widely used in laser interferometry. On the other hand, if we allow off-axis beam transformations and misaligned optical systems, general astigmatic beams can be produced in many cases. As it was mentioned in Chapter 2, general astigmatic beams can be produced from stigmatic or simple astigmatic beams even in optical systems that contain only planar and spherical surfaces. Taking this into account, the general astigmatic beams become widespread and thus important to study.

The model suggested in this chapter follows the discussion presented in [P5]. It does not only combine the previously available investigations of general astigmatic Gaussian beams, but also provides a detailed derivations that enable deep understanding of physical properties and mathematical description of this kind of beams. One of the key problems in general astigmatic beam model development is to find a way to correctly transform the beams impinging on a surface at a non-normal incidence. To the best of our knowledge the only work so far that can handle the transformation of astigmatic beams incident at some angle on arbitrary second order surfaces (for example spheres, ellipsoids or cylinders), is the work by Rohani [11]. Unfortunately, this paper (as well as [24] and [25]) contains typos and only briefly explains the procedure of obtaining the necessary formulae. In this chapter I will re-derive the formulas suggested by Rohani and generalize them to the case of arbitrary choice of the beam-fixed and surface-fixed coordinate systems.

As for the stigmatic and simple astigmatic Gaussian beams, the description of the general astigmatic Gaussian beam will include the four main aspects: the complex amplitude of the electric field, intensity and phase distributions, the law of propagation and the laws of beam transformation via reflection and refraction. The general astigmatic beam model is applicable to the beam jitter simulations in every optical system, where each surface can be represented with the second order equation at the point of incidence.

5.1. Complex amplitude of the electric field

The complex envelope given in equation (4.11) remains the solution of the paraxial Helmholtz equation (3.4) even if the value of angle θ is complex. In this case equation (4.11) describes the general astigmatic Gaussian beam [8]. Then the complex amplitude of the electric field can be described by the same expression as the complex amplitude of the electric field of simple astigmatic beam, tilted around the axis of propagation:

$$E(\mathbf{r}, z) = E_0(z) \exp \left\{ -i\phi_{ac} + i\eta(z) - i\frac{k}{2} \left[\left(\frac{\cos^2 \theta}{q_1(z)} + \frac{\sin^2 \theta}{q_2(z)} \right) x^2 + \left(\frac{\sin^2 \theta}{q_1(z)} + \frac{\cos^2 \theta}{q_2(z)} \right) y^2 + \sin 2\theta \left(\frac{1}{q_1(z)} - \frac{1}{q_2(z)} \right) xy \right] \right\}. \quad (5.1)$$

The only difference between this equation and equation (4.12) is that in the first case angle θ is complex-valued. Seemingly small difference in definitions of simple and general astigmatic beams results in significant changes in their physical properties. We will discuss these in details in the next section.

The accumulated phase is defined in the same way as for stigmatic and simple astigmatic beams (see equation (3.25)). Due to the complex value of angle θ none of the known physical interpretations of the q -parameters holds (see equations (4.3) and (4.4)). However, the **Gouy phase** $\eta(z)$ can still be defined as

$$\eta(z) = \frac{1}{2} \left[\arctan \left(\frac{\Re(q_1)}{\Im(q_1)} \right) + \arctan \left(\frac{\Re(q_1)}{\Im(q_1)} \right) \right], \quad (5.2)$$

where $\Re(q)$ and $\Im(q)$ stand for the real and imaginary part of the complex number q correspondingly [8]. This expression is identical to the expression for Gouy phase of simple astigmatic beam given in equation (4.5).

Equation (5.1) can be rewritten as

$$E(\mathbf{r}, z) = E_0(z) \exp \left\{ -i\phi_{ac} + i\eta(z) - i\frac{k}{2} \mathbf{r}^T Q \mathbf{r} \right\}, \quad (5.3)$$

where

$$Q(z) = \begin{pmatrix} \frac{\cos^2 \theta}{q_1(z)} + \frac{\sin^2 \theta}{q_2(z)} & \frac{1}{2} \sin 2\theta \left(\frac{1}{q_1(z)} - \frac{1}{q_2(z)} \right) \\ \frac{1}{2} \sin 2\theta \left(\frac{1}{q_1(z)} - \frac{1}{q_2(z)} \right) & \frac{\sin^2 \theta}{q_1(z)} + \frac{\cos^2 \theta}{q_2(z)} \end{pmatrix} \quad (5.4)$$

is **complex radius of curvature tensor for generalized Gaussian beams** [19]. The superscript T means transposed.

The complex radius of curvature tensor given in equation (5.3) can also be used to represent circular and simple astigmatic Gaussian beams. In these cases it is defined as

$$Q_{\text{stigmatic}} = \begin{pmatrix} 1/q & 0 \\ 0 & 1/q \end{pmatrix}, \quad (5.5) \quad Q_{\text{SA}} = \begin{pmatrix} 1/q_1 & 0 \\ 0 & 1/q_2 \end{pmatrix}. \quad (5.6)$$

If the principal coordinate system of the simple astigmatic beam is tilted with respect to the beam-fixed coordinate system, the complex radius of curvature tensor in the beam-fixed coordinate system will follow equation (5.4), but angle θ has to stay real-valued in this case. Therefore, equation (5.3) can be used to represent the complex amplitude of electric field for all types of Gaussian beams in fundamental mode.

The complex radius of curvature tensor for general astigmatic or titled simple astigmatic beams (equation (5.4)) can be obtained from the complex radius of curvature tensor for simple astigmatic beams (equation (5.6)) by applying **rotation matrix**:

$$Q = S(\theta)^T Q_{\text{SA}} S(\theta), \quad (5.7)$$

where

$$S(\theta) = \begin{pmatrix} \cos \theta & \sin \theta \\ -\sin \theta & \cos \theta \end{pmatrix} \quad (5.8)$$

corresponds to the coordinate transformation given in equation (4.10).

The normalization constant $E_0(z)$ can be computed using the fact that the total beam power at the cross-section is the integral of the optical intensity in this cross-section, as it was done for simple astigmatic beam in equation (4.6). The optical intensity of the beam can be represented as

$$I(x, y, z) = |E(x, y, z)|^2 = E_0(z)^2 \exp(g_1(z)x^2 + g_2(z)y^2 + g(z)xy), \quad (5.9)$$

where

$$\begin{aligned} g_1(z) &= k\Im(Q_{11}) \\ g_2(z) &= k\Im(Q_{22}) \\ g(z) &= k\Im(Q_{12} + Q_{21}) \end{aligned} \quad (5.10)$$

and Q_{ij} stands for the ij -element of the complex radius of curvature tensor $Q(z)$. Substituting equation (5.9) into equation (4.6) and computing the double integral using the Euler-Poisson (Gaussian) integral (4.7), we obtain

$$\begin{aligned} P &= \iint E_0^2(z) \exp(g_1(z)x^2 + g_2(z)y^2 + g(z)xy) dx dy = \\ &E_0^2(z) \iint \exp \left[g_1(z) \left(x + \frac{g(z)}{2g_1(z)} y \right)^2 + \left(g_2(z) - \frac{g^2(z)}{4g_1(z)} \right) y^2 \right] dx dy = \\ &E_0^2(z) \sqrt{\frac{\pi}{-g_1(z)}} \int \exp \left[\left(g_2(z) - \frac{g^2(z)}{4g_1(z)} \right) y^2 \right] dy = \\ &E_0^2(z) \sqrt{\frac{\pi}{-g_1(z)}} \sqrt{\frac{\pi}{g^2(z)/4g_1(z) - g_2(z)}} = \\ &E_0^2(z) \frac{2\pi}{\sqrt{4g_1(z)g_2(z) - g^2(z)}}, \end{aligned} \quad (5.11)$$

which leads to:

$$E_0(z) = \sqrt{\frac{P}{\lambda} \sqrt{4\Im(Q_{11})\Im(Q_{22}) - \Im(Q_{12} + Q_{21})^2}}. \quad (5.12)$$

When $\theta = 0$ expressions from (5.10) look as following:

$$g_1 = -k \frac{\Im(q_1)}{|q_1|^2}, \quad g_2 = -k \frac{\Im(q_2)}{|q_2|^2}, \quad g = 0. \quad (5.13)$$

Then equation (5.12) gives the same result as equation (4.8), which in turn gives the same result as equation (3.11) when $q_1 = q_2 = q$.

Substituting equation (5.12) into equation (5.3), we get the expression for the complex amplitude of generalized Gaussian beam in fundamental mode:

$$E(\mathbf{r}, z) = \sqrt{\frac{P}{\lambda} \sqrt{4\Im(Q_{11})\Im(Q_{22}) - \Im(Q_{12} + Q_{21})^2}} \exp \left\{ -i\phi_{ac} + i\eta(z) - i\frac{k}{2} \mathbf{r}^T \mathbf{Q} \mathbf{r} \right\}. \quad (5.14)$$

Depending on the value of the complex radius of curvature tensor Q , it can represent general astigmatic, simple astigmatic or circular Gaussian beams.

From equations (5.1) and (5.3) it follows that in order to fully describe general astigmatic Gaussian beam one can choose either of two strategies. The first one is to use three complex-valued parameters: two q -parameters $q_i, i = 1, 2$, and one complex angle θ . Another possible strategy is to use the complex radius of curvature tensor (equation (5.4)). Both strategies are connected: the reciprocals of q_1 and q_2 are the eigenvalues of the complex radius of curvature tensor. Complex valued angle θ can be obtained from Q using the relationship

$$\tan 2\theta = \frac{Q_{12} + Q_{21}}{Q_{11} - Q_{22}}. \quad (5.15)$$

5.2. The law of propagation

In [26] the simple analytic formula that describes the propagation of a general astigmatic Gaussian beam in a homogeneous medium is given by:

$$Q' = \frac{Q}{E + \Delta z Q}, \quad (5.16)$$

where E is the unity matrix, Δz is the propagation distance. Equation (5.16) is equivalent to

$$Q' = \begin{pmatrix} \frac{\cos^2 \theta}{q_1 + \Delta z} + \frac{\sin^2 \theta}{q_2 + \Delta z} & \frac{1}{2} \sin 2\theta \left(\frac{1}{q_1 + \Delta z} - \frac{1}{q_2 + \Delta z} \right) \\ \frac{1}{2} \sin 2\theta \left(\frac{1}{q_1 + \Delta z} - \frac{1}{q_2 + \Delta z} \right) & \frac{\sin^2 \theta}{q_1 + \Delta z} + \frac{\cos^2 \theta}{q_2 + \Delta z} \end{pmatrix}. \quad (5.17)$$

Therefore the propagation law for general astigmatic Gaussian beam is identical to the one for simple astigmatic Gaussian beam:

$$\begin{aligned} q'_1 &= q_1 + \Delta z, \\ q'_2 &= q_2 + \Delta z. \end{aligned} \quad (5.18)$$

The optical pathlength and accumulated phase change as

$$s'_{\text{ac}} = s_{\text{ac}} + n\Delta z, \quad (5.19)$$

$$\phi'_{\text{ac}} = \phi_{\text{ac}} + k\Delta z. \quad (5.20)$$

The complex angle θ remains unaffected along the propagation.

5.3. Intensity and phase distribution

As it was mentioned above, q -parameters do not have a direct physical interpretation for general astigmatic beams. In this section I will first derive the expressions for the real-valued parameters of the beam: spot radii, radii of curvature of the wavefronts and orientations of light spots and wavefronts. Then I will talk about the evolution of these parameters and, therefore, the behavior of the general astigmatic beam as it propagates in free space.

5.3.1. Beam parameters

In order to obtain the beam radii and radii of curvature of the wavefront let me first separate the real and imaginary parts of the **complex phase** $\psi(\mathbf{r}, z)$, which is defined as the complex-valued argument of exponent in equation (5.3):

$$\psi(\mathbf{r}, z) = -i\phi_{\text{ac}} + i\eta(z) - i\frac{k}{2} \mathbf{r}^T Q \mathbf{r}. \quad (5.21)$$

In order to do so I will define the real-valued matrices

$$W(z) = -(k/2)\Im(Q), \quad C(z) = \Re(Q) \quad (5.22)$$

and rewrite the complex amplitude of the electric field (equation (5.3)) [27] as

$$E(\mathbf{r}, z) = E_0(z) \exp \left\{ -i\phi_{\text{ac}} + i\eta(z) - \mathbf{r}^T W(z) \mathbf{r} - i\frac{k}{2} \mathbf{r}^T C(z) \mathbf{r} \right\}. \quad (5.23)$$

For circular beams matrices W and C represent the light spots and the wavefronts:

$$W_{\text{circular}}(z) = \begin{pmatrix} \frac{1}{w^2(z)} & 0 \\ 0 & \frac{1}{w^2(z)} \end{pmatrix}, \quad C_{\text{circular}}(z) = \begin{pmatrix} \frac{1}{R(z)} & 0 \\ 0 & \frac{1}{R(z)} \end{pmatrix}. \quad (5.24)$$

Similarly for simple astigmatic beams in their principal coordinate system:

$$W_{\text{SA}}(z) = \begin{pmatrix} \frac{1}{w_1^2(z)} & 0 \\ 0 & \frac{1}{w_2^2(z)} \end{pmatrix}, \quad C_{\text{SA}}(z) = \begin{pmatrix} \frac{1}{R_1(z)} & 0 \\ 0 & \frac{1}{R_2(z)} \end{pmatrix}, \quad (5.25)$$

For the general astigmatic beam the **matrices** defined in equation (5.22) still **represent the ellipses of constant intensity and of constant phase**. However, in this case both matrices are non-diagonal. Similarly to the complex radius of curvature tensor for generalized Gaussian beams (equation (5.7)) they can be obtained as

$$W = S(\varphi_w)^T W_{SA} S(\varphi_w), \quad (5.26)$$

$$C = S(\varphi_R)^T C_{SA} S(\varphi_R), \quad (5.27)$$

or, writing down the result of multiplication,

$$W(z) = \begin{pmatrix} \frac{\cos^2 \varphi_w}{w_1^2(z)} + \frac{\sin^2 \varphi_w}{w_2^2(z)} & \frac{1}{2} \sin 2\varphi_w \left(\frac{1}{w_1^2(z)} - \frac{1}{w_2^2(z)} \right) \\ \frac{1}{2} \sin 2\varphi_w \left(\frac{1}{w_1^2(z)} - \frac{1}{w_2^2(z)} \right) & \frac{\sin^2 \varphi_w}{w_1^2(z)} + \frac{\cos^2 \varphi_w}{w_2^2(z)} \end{pmatrix}, \quad (5.28)$$

$$C(z) = \begin{pmatrix} \frac{\cos^2 \varphi_R}{R_1(z)} + \frac{\sin^2 \varphi_R}{R_2(z)} & \frac{1}{2} \sin 2\varphi_R \left(\frac{1}{R_1(z)} - \frac{1}{R_2(z)} \right) \\ \frac{1}{2} \sin 2\varphi_R \left(\frac{1}{R_1(z)} - \frac{1}{R_2(z)} \right) & \frac{\sin^2 \varphi_R}{R_1(z)} + \frac{\cos^2 \varphi_R}{R_2(z)} \end{pmatrix}.$$

Note that for simple astigmatic beams tilted by a real-valued angle θ around the z axis equation (5.28) holds with $\varphi_w = \varphi_R = \theta$. The eigenvalues $1/w_i^2$, $i = 1, 2$ of the matrix $W(z)$ are reciprocals of the principal axes of the intensity ellipse squared. Similarly the eigenvalues $1/R_i$, $i = 1, 2$ of the matrix $C(z)$ are the reciprocals of the principal radii of curvature of the wavefront. The **orientation of ellipses** is described by the angles φ_w and φ_R , which can be obtained in the same way as the angle θ in equation (5.15):

$$\tan 2\varphi_w = \frac{W_{12} + W_{21}}{W_{11} - W_{22}}, \quad (5.29)$$

$$\tan 2\varphi_R = \frac{C_{12} + C_{21}}{C_{11} - C_{22}}. \quad (5.30)$$

Equations (5.29)-(5.30) and eigenvalue computation are already sufficient for computation of the intensity and phase distribution of any Gaussian beam in the fundamental mode. However, they don't provide a direct description of general astigmatic Gaussian beam characteristics. In order to study these more closely we can substitute

$$\begin{aligned} \theta &= \theta^{\Re} + i\theta^{\Im}, \\ 1/q_i &= \rho_i - i\omega_i, \quad i = 1, 2, \\ \rho_i(z) &= \Re(q_i)/|q_i|^2, \\ \omega_i(z) &= \Im(q_i)/|q_i|^2 \end{aligned} \quad (5.31)$$

in the complex radius of curvature tensor $Q(z)$ (equation (5.4)) and obtain the matrices $W(z)$ and $C(z)$ from equation (5.22). Then the elements of matrix $W(z)$ are:

$$\begin{aligned} w_{11} &= \frac{k}{4}(\omega_1 + \omega_2 + (\omega_1 - \omega_2) \cos 2\theta^{\Re} \cosh 2\theta^{\Im} + (\rho_1 - \rho_2) \sin 2\theta^{\Re} \sinh 2\theta^{\Im}), \\ w_{12} = w_{21} &= \frac{k}{4}((\omega_1 - \omega_2) \sin 2\theta^{\Re} \cosh 2\theta^{\Im} - (\rho_1 - \rho_2) \cos 2\theta^{\Re} \sinh 2\theta^{\Im}), \\ w_{22} &= \frac{k}{4}(\omega_1 + \omega_2 - (\omega_1 - \omega_2) \cos 2\theta^{\Re} \cosh 2\theta^{\Im} - (\rho_1 - \rho_2) \sin 2\theta^{\Re} \sinh 2\theta^{\Im}). \end{aligned} \quad (5.32)$$

Similarly the elements of matrix $C(z)$ are:

$$\begin{aligned} c_{11} &= \frac{1}{2}(\rho_1 + \rho_2 + (\rho_1 - \rho_2) \cos 2\theta^{\Re} \cosh 2\theta^{\Im} - (\omega_1 - \omega_2) \sin 2\theta^{\Re} \sinh 2\theta^{\Im}), \\ c_{12} = c_{21} &= \frac{1}{2}((\rho_1 - \rho_2) \sin 2\theta^{\Re} \cosh 2\theta^{\Im} + (\omega_1 - \omega_2) \cos 2\theta^{\Re} \sinh 2\theta^{\Im}), \\ c_{22} &= \frac{1}{2}(\rho_1 + \rho_2 - (\rho_1 - \rho_2) \cos 2\theta^{\Re} \cosh 2\theta^{\Im} + (\omega_1 - \omega_2) \sin 2\theta^{\Re} \sinh 2\theta^{\Im}). \end{aligned} \quad (5.33)$$

Then using equations (5.29)-(5.30), the values for the **angles of orientation** φ_w and φ_R **of the intensity and phase ellipses** are

$$\tan 2\varphi_w = \frac{(\omega_1 - \omega_2) \tan 2\theta^{\Re} - (\rho_1 - \rho_2) \tanh 2\theta^{\Im}}{(\omega_1 - \omega_2) + (\rho_1 - \rho_2) \tan 2\theta^{\Re} \tanh 2\theta^{\Im}}, \quad (5.34)$$

$$\tan 2\varphi_R = \frac{(\rho_1 - \rho_2) \tan 2\theta^{\Re} + (\omega_1 - \omega_2) \tanh 2\theta^{\Im}}{(\rho_1 - \rho_2) - (\omega_1 - \omega_2) \tan 2\theta^{\Re} \tanh 2\theta^{\Im}}. \quad (5.35)$$

It is easy to see that $\tan 2\varphi_w = \tan 2(\varphi_{w0} + \theta^{\Re})$ and $\tan 2\varphi_R = \tan 2(\varphi_{R0} + \theta^{\Re})$, where φ_{w0} and φ_{R0} are the angles of the constant intensity and phase ellipses for the case of $\theta^{\Re} = 0$. Therefore,

$$\tan 2\varphi_{w0}(z) = -\frac{\rho_1(z) - \rho_2(z)}{\omega_1(z) - \omega_2(z)} \tanh 2\theta^{\Im}, \quad \varphi_w(z) = \varphi_{w0}(z) + \theta^{\Re}, \quad (5.36)$$

$$\tan 2\varphi_{R0}(z) = \frac{\omega_1(z) - \omega_2(z)}{\rho_1(z) - \rho_2(z)} \tanh 2\theta^{\Im}, \quad \varphi_R(z) = \varphi_{R0}(z) + \theta^{\Re}. \quad (5.37)$$

The eigenvalues of the matrices $W(z)$ and $C(z)$ can be expressed as

$$\frac{1}{w_{1,2}^2(z)} = \frac{k}{4} \left\{ \omega_1(z) + \omega_2(z) \pm \sqrt{[\omega_1(z) - \omega_2(z)]^2 \cosh^2 2\theta^{\Im} + [\rho_1(z) - \rho_2(z)]^2 \sinh^2 2\theta^{\Im}} \right\}, \quad (5.38)$$

$$\frac{1}{R_{1,2}(z)} = \frac{1}{2} \left\{ \rho_1(z) + \rho_2(z) \pm \sqrt{[\rho_1(z) - \rho_2(z)]^2 \cosh^2 2\theta^{\Im} + [\omega_1(z) - \omega_2(z)]^2 \sinh^2 2\theta^{\Im}} \right\}. \quad (5.39)$$

Equations (5.36)-(5.39) introduce the physical meaning of the complex parameters of general astigmatic Gaussian beam. In the simple astigmatic case each principal axis of the beam spot ellipse and the phase ellipse can be computed from a single q -parameter using equation (3.7). In the general astigmatic case instead each real-valued parameter is computed using both q -parameters and the value of the complex angle θ . Therefore a single q -parameter or angle θ alone does not have a direct physical interpretation for general astigmatic beams.

We have shown that the parameters of intensity and phase distributions of the general astigmatic Gaussian beam can be obtained from the radius of curvature tensor $Q(z)$ using eigenvalue computation and simple equations (5.29) and (5.30). Alternatively, one can use equations (5.36)-(5.39) that allow to compute these parameters from complex-valued q -parameters and the angle θ .

5.3.2. Beam evolution

The complex angle θ (and thus both θ^{\Re} and θ^{\Im}) does not change as the beam propagates in free space (equation (5.18)). Its real part θ^{\Re} is one of the two terms for both angles φ_w and φ_R (equations (5.36) and (5.37)) and it does not couple into the principal axes of the ellipses of constant intensity and constant phase (equations (5.38), (5.39)). These two facts allow the interpretation of θ^{\Re} as the angle of rotation of the entire beam. It is always possible to choose a beam-fixed coordinate system where θ^{\Re} is zero. The imaginary part θ^{\Im} causes the orientations of both ellipses of constant intensity and of constant phase (φ_w and φ_R) to change along the propagation (equations (5.36) and (5.37)). In order to study this dependence we will illustrate the evolution of the two q parameters (equation (5.31)) by a Gaussian beam (or Collins [20, p. 681]) chart (Figure 5.1). The evolution of each of the two q -parameters is represented by a circle with a diameter of $1/\Im(q)$. The line connecting two circles at identical values of z changes the angle with the ω axis monotonically by a total of 2π as z goes from $-\infty$ to $+\infty$. The tangent of this angle for each value of z is $(\rho_1 - \rho_2)/(\omega_1 - \omega_2)$. This value is used in both equations (5.36) and (5.37). Therefore both φ_w and φ_R change monotonically with increasing z . Depending on the value of θ^{\Im} angles can either increase, or decrease. Each angle changes by a total of π radians from $z = -\infty$ to $z = \infty$. Experimental observation over the infinite range is impossible, but by choosing to observe the regions with maximum slope $\partial\varphi_w/\partial z$ (or $\partial\varphi_R/\partial z$) one can see most of the overall rotation of the ellipse of constant intensity (or ellipse of constant phase).

The relative orientation of the ellipses of constant intensity and constant phase

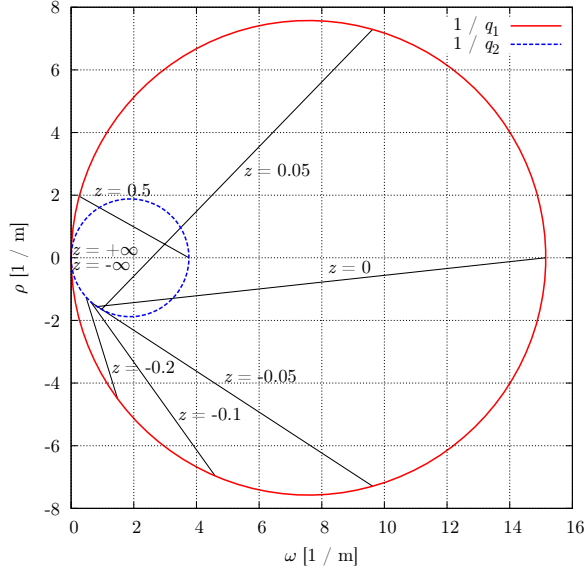


Figure 5.1.: A Gaussian beam (or Collins) chart. $q_1 = i66 \text{ mm}$, $q_2 = -500 + i266 \text{ mm}$ at $z = 0$. The axes are $\omega(z) = \Im(q)/|q|^2$ and $\rho(z) = \Re(q)/|q|^2$. The line connecting two circles for the same value of z forms an angle with tangent $(\rho_1 - \rho_2)/(\omega_1 - \omega_2)$ with the ω axis.

(from equations (5.36) and (5.37)) is described by

$$\tan 2(\varphi_w(z) - \varphi_R(z)) = -\sinh 2\theta^{\Im} \cosh 2\theta^{\Re} \left(\frac{\rho_1(z) - \rho_2(z)}{\omega_1(z) - \omega_2(z)} + \frac{\omega_1(z) - \omega_2(z)}{\rho_1(z) - \rho_2(z)} \right). \quad (5.40)$$

This equation shows that the ellipses can only be aligned (have a relative angle of 0 or $\pi/2$) at a given point z' if either $\theta^{\Im} = 0$ or $q_1(z') = q_2(z')$. According to the law of propagation (equation (5.18)) this is only possible for special cases of the simple astigmatism or perfect stigmatism. Thus the ellipses of constant intensity and constant phase cannot be aligned at any point along the propagation for general astigmatic beams. Similarly it can be shown that spot ellipses and wavefronts of the general astigmatic Gaussian beam never degenerate to circles. Equation (5.40) shows that the relative orientation changes along the z axis. Only the invariant

$$\tan 2\varphi_{w0}(z) \tan 2\varphi_{R0}(z) = -\tanh^2 2\theta^{\Im} \quad (5.41)$$

is independent of z .

The evolution of the beam width is presented in Figure 5.2. The beam parameters that were used to produce this figure are identical to those for Figure 4.2 that illustrates the evolution of the beam width of the simple astigmatic beam. Only the complex angle θ is added in general astigmatic case. These two plots illustrate the

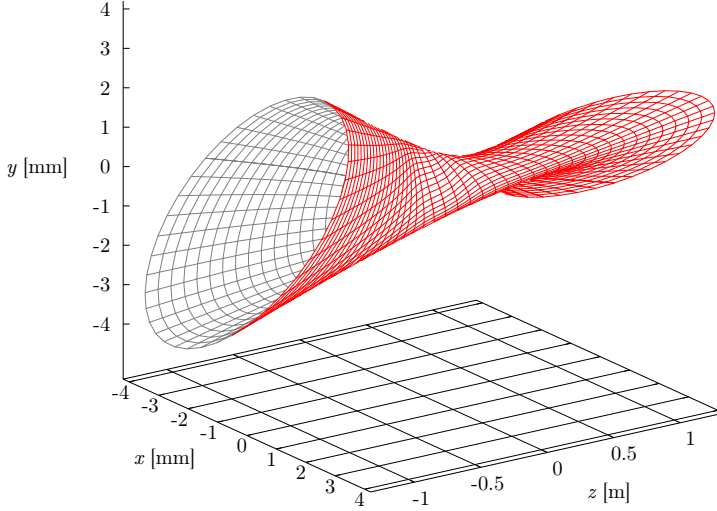


Figure 5.2.: General astigmatic Gaussian beam. Beam width evolution. q -parameters: $q_1 = i66$ mm, $q_2 = -500 + i266$ mm at $z = 0$ (identical to q -parameters used in figure 4.2). Complex angle $\theta = 20^\circ - i10^\circ$. The wavelength $\lambda = 1064$ nm.

comparison of two types of astigmatism of Gaussian beam. The corresponding graphs for the major and minor semi-axes of both ellipses of constant phase and constant intensity are shown in Figure 5.3. For simple astigmatic beams waist positions and Rayleigh ranges can be found from the q -parameters using equation (4.4) separately in each of the planes of symmetry. The minimal wavefront radius of curvature in this case is achieved where $z = z_{0i} \pm z_{Ri}$ and is equal to $2z_{Ri}$. This physical interpretation no longer holds for general astigmatic Gaussian beams.

Let us estimate the expression under the square root sign in equation (5.38):

$$[\omega_1(z) - \omega_2(z)]^2 \underbrace{\cosh^2 2\theta^{\Im}}_{\geq 1} + \underbrace{[\rho_1(z) - \rho_2(z)]^2 \sinh^2 2\theta^{\Im}}_{\geq 0} \geq [\omega_1(z) - \omega_2(z)]^2, \quad (5.42)$$

and equality holds only in the simple astigmatic case. This means that for any value of θ^{\Im}

$$\frac{1}{w_{2GA}^2(z)} < \frac{1}{w_{1,2SA}^2(z)} < \frac{1}{w_{1GA}^2(z)} \quad (5.43)$$

where $w_{1,2GA}(z)$ are the major and minor semi-axes of the intensity ellipse of the general astigmatic beam, $w_{1,2SA}(z)$ are the semi-axes of the intensity ellipse of the simple astigmatic beam with identical q -parameters. Taking into account that all values of spot radii are positive, this is equivalent to

$$w_{1GA}(z) < w_{1,2SA}(z) < w_{2GA}(z) \quad (5.44)$$

for any value of z . This fact is illustrated in Figure 5.3a and effectively means that for any general astigmatic Gaussian beam its ellipses of constant intensity have higher ellipticity than for the corresponding simple astigmatic Gaussian beam. Similarly

$$\frac{1}{R_{2GA}(z)} < \frac{1}{R_{1,2SA}(z)} < \frac{1}{R_{1GA}(z)}, \quad (5.45)$$

where $R_{1,2GA}(z)$ are the principal radii of curvature of the wavefront of the general astigmatic Gaussian beam, $R_{1,2SA}(z)$ are the principal radii of curvature of the wavefront of the corresponding simple astigmatic Gaussian beam. Since some of those radii can be negative we can not draw the same conclusion as for spot radii (see Figure 5.3b).

The value of θ^{\Im} cannot be arbitrary. The semi-axes of the spot ellipse should always be positive [8]:

$$\omega_1 + \omega_2 \geq \sqrt{(\omega_1 - \omega_2)^2 \cosh^2 2\theta^{\Im} + (\rho_1 - \rho_2)^2 \sinh^2 2\theta^{\Im}}. \quad (5.46)$$

This condition is equivalent to:

$$\cosh^2 2\theta^{\Im} \leq \frac{(\omega_1 + \omega_2)^2 + (\rho_1 - \rho_2)^2}{(\omega_1 - \omega_2)^2 + (\rho_1 - \rho_2)^2}, \quad (5.47)$$

which in turn is the same as

$$\cosh^2 2\theta^{\Im} \leq \frac{(\Re(q_1) - \Re(q_2))^2 + (\Im(q_1) - \Im(q_2))^2}{(\Re(q_1) - \Re(q_2))^2 + (\Im(q_1) - \Im(q_2))^2}, \quad (5.48)$$

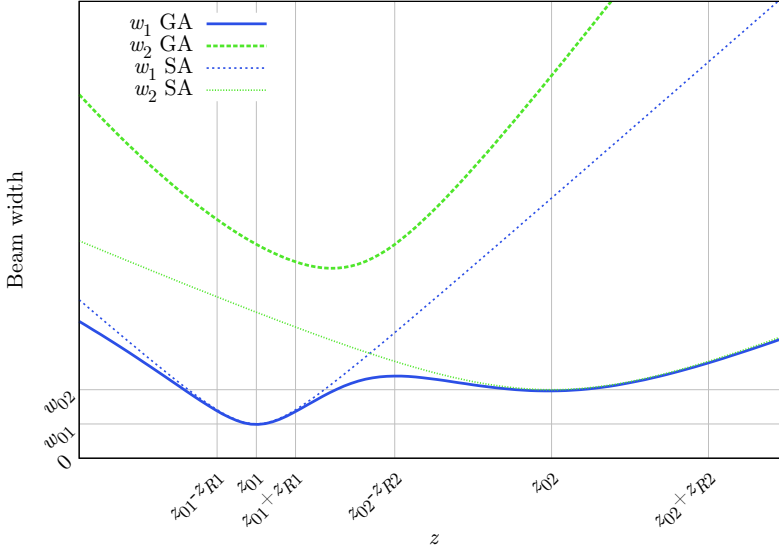
or, more compactly

$$\cosh^2 2\theta^{\Im} \leq \left| \frac{q_1 - q_2^*}{q_1 - q_2} \right|. \quad (5.49)$$

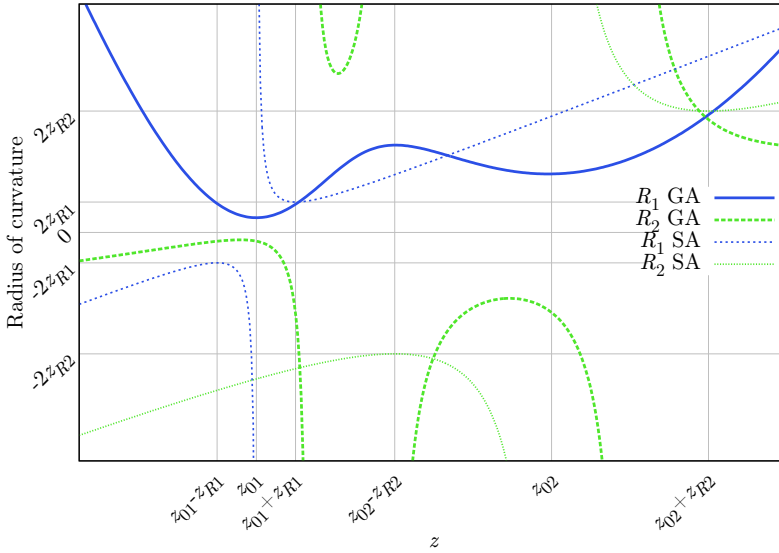
If this restriction is fulfilled at some position z , it is fulfilled at every point along the beam axis. Therefore, confined beam remains confined as it propagates in free space.

5.4. Beam transformation

In order to obtain the formulae for general astigmatic Gaussian beam transformation via reflection or refraction we will generally follow the procedure proposed in [11]. In our derivations we will add the possibility of choosing beam-fixed and surface-fixed transversal coordinate vectors arbitrarily. We will use the fact that the complex phase (equation (5.21)) of incident, reflected and refracted beams should match exactly on the surface. This is, therefore, an extension of the phase matching method described in [28, 29]. We will assume that at the point of incidence the beam radii are small in comparison to the radii of curvature of the surface.



(a) Beam width evolution.



(b) Radius of curvature of the wavefront evolution.

Figure 5.3.: Beam width evolution (a) and radius of curvature of the wavefront evolution (b) of a general astigmatic Gaussian beam in comparison to the same parameters of a simple astigmatic Gaussian beam with identical q -parameters and optical wavelength. $q_1 = i66$ mm, $q_2 = -500 + i266$ mm at $z = 0$. $\lambda = 1064$ nm. The complex angle for the general astigmatic beam is $\theta = 20^\circ + i10^\circ$. For any value of z : $w_{1GA}(z) < w_{1,2SA}(z) < w_{2GA}(z)$, $w_{1GA}(z) \neq w_{2GA}(z)$, and $R_{1GA}(z) \neq R_{2GA}(z)$.

Any second order 3D surface (sphere, ellipsoid, cylinder etc.) can be described by a quadratic equation

$$\mathbf{s}(\mathbf{d}) = d_1 \hat{d}_1 + d_2 \hat{d}_2 - \frac{1}{2}(\mathbf{d}^T C_s \mathbf{d}) \hat{n}, \quad (5.50)$$

where \mathbf{d} is a 2D vector with components d_1 and d_2 , $(\hat{d}_1, \hat{d}_2, \hat{n})$ is an orthonormal local coordinate system describing a surface at the point of incidence (see Figure 5.4) such that \hat{n} is a unit vector normal to the surface and \hat{d}_1 and \hat{d}_2 are unit vectors in the plane tangential to the surface. Vectors \hat{d}_1 and \hat{d}_2 can be chosen arbitrarily such that the coordinate system stays orthonormal. C_s is the **curvature matrix of the surface** in the local coordinate system. Any higher order surface can be locally approximated using equation (5.50).

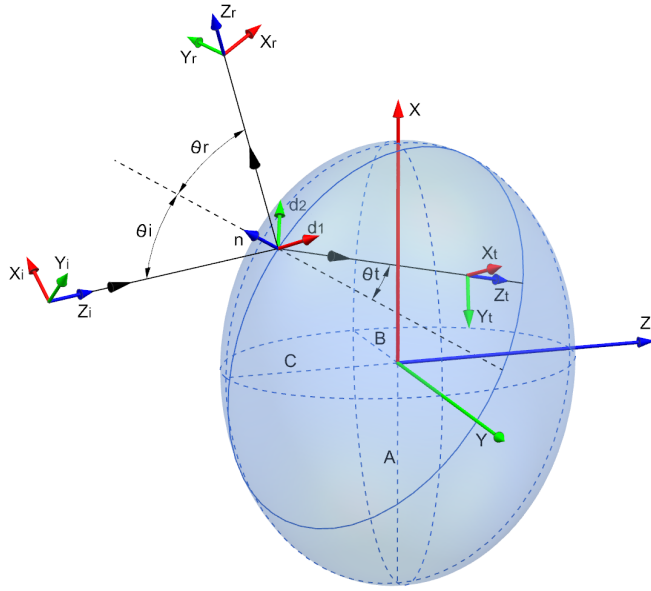


Figure 5.4.: Reflection and refraction of a general astigmatic Gaussian beam at an ellipsoidal surface.

If the surface equation in the local coordinate system is given, one can obtain its curvature matrix C_s as the second order derivative at the point of incidence. For example the ellipsoid with the principal semi-axes A , B and C (see Figure 5.4) in its nominal coordinate system, placed in the center of the ellipsoid, is represented by

$$f(\mathbf{x}) = \mathbf{x}^T S \mathbf{x} - 1 = 0, \quad (5.51)$$

where

$$S = \begin{pmatrix} 1/A^2 & 0 & 0 \\ 0 & 1/B^2 & 0 \\ 0 & 0 & 1/C^2 \end{pmatrix}, \quad (5.52)$$

and $\mathbf{x} = (x, y, z)$ is a coordinate vector. We can rewrite this equation in the local coordinate system using the affine transformation $\mathbf{x}' = M\mathbf{x} + \mathbf{t}$, where \mathbf{t} is a vector connecting the center of the ellipsoid with the point of incidence, and M is a rotation matrix from the nominal ellipsoid coordinate system into the local coordinate system. Then we obtain

$$f(\mathbf{x}') = (\mathbf{x}' - \mathbf{t})^T S' (\mathbf{x}' - \mathbf{t}) - 1 = 0. \quad (5.53)$$

Here $S' = MSM^T$. From this equation we need to derive z' as a function of (x', y') and find the curvature matrix as it's second order derivative

$$C_s = \begin{pmatrix} \partial^2 z' / \partial x'^2 & \partial^2 z' / \partial x' \partial y' \\ \partial^2 z' / \partial y' \partial x' & \partial^2 z' / \partial y'^2 \end{pmatrix}. \quad (5.54)$$

Skipping lengthy calculations (see appendix A), the curvature matrix of an ellipsoid at a point on it's surface is equal to

$$C_{\text{ellipsoid}} = \pm \frac{1}{b} \begin{pmatrix} S'_{11}S'_{33} - S'^2_{13} + g^2_{t_y} & S'_{12}S'_{33} - S'_{13}S'_{23} - g_{t_x}t_y \\ S'_{12}S'_{33} - S'_{13}S'_{23} - g_{t_x}t_y & S'_{22}S'_{33} - S'^2_{23} + g^2_{t_x} \end{pmatrix}, \quad (5.55)$$

where

$$\begin{aligned} b &= [(S'_{13}t_x + S'_{23}t_y)^2 - S'_{33}(S'_{11}t_x^2 + 2S'_{12}t_x t_y + S'_{22}t_y^2 - 1)]^{3/2}, \\ g &= S'_{11}S'^2_{23} + S'_{22}S'^2_{13} + S'_{33}S'^2_{12} - 2S'_{12}S'_{13}S'_{23} - S'_{11}S'_{22}S'_{33}, \end{aligned} \quad (5.56)$$

S'_{ij} are the elements of matrix S' . Equation (5.55) can also be used for cylindrical surfaces ($1/A^2$ or $1/B^2$ should then be set to 0). In the special case of spherical surfaces the curvature matrix is the same at every point of the surface:

$$C_{\text{sphere}} = \pm \begin{pmatrix} c & 0 \\ 0 & c \end{pmatrix}, \quad (5.57)$$

where $1/c$ is the radius of the sphere.

Now let us introduce three beam-fixed coordinate systems $(\hat{x}_l, \hat{y}_l, \hat{z}_l)$ for $l = i, r, t$ for incident, reflected and transmitted beams, respectively (Figure 5.4). Similar to ray fixed coordinate system from [29, chapter 4] \hat{z}_l corresponds to the direction of the beam and transversal unit vectors \hat{x}_l and \hat{y}_l can be chosen arbitrarily such that coordinate system $(\hat{x}_l, \hat{y}_l, \hat{z}_l)$ stays orthonormal. The directions of the beams are connected via law of reflection (2.2) and law of refraction (2.3).

For each of the three beams the complex radius of curvature tensor $Q_l(z_l)$ is given in a corresponding coordinate system $(\hat{x}_l, \hat{y}_l, \hat{z}_l)$. The complex phase (equation (5.21)) of each of the three beams in their beam-fixed coordinate system is

$$\psi(\mathbf{r}_l, z_l) = -\phi_{ac l} + k_l \frac{1}{2} \mathbf{r}_l^T Q_l(z_l) \mathbf{r}_l, \quad l = i, r, t, \quad (5.58)$$

where \mathbf{r}_l is a vector of transversal coordinates x_l and y_l in a beam-fixed coordinate system $(\hat{x}_l, \hat{y}_l, \hat{z}_l)$. We neglect the slowly varying Gouy phase $\eta(z)$ since it can be computed independently using equation (5.2). In order to keep the Gouy phase continuous, the accumulated Gouy phase can be used as described in Chapter 3. Similarly to simple astigmatic case, we can use the term $k_l z_l$ instead of accumulated phase in the phase matching.

The points (x_l, y_l, z_l) on a surface (equation (5.50)) can be found from

$$\begin{aligned} x_l &= \mathbf{s}(\mathbf{d}) \hat{x}_l = d_1 \hat{x}_l \hat{d}_1 + d_2 \hat{x}_l \hat{d}_2 - 1/2 (\mathbf{d} C_s \mathbf{d}^T) \hat{x}_l \hat{n} \\ y_l &= \mathbf{s}(\mathbf{d}) \hat{y}_l = d_1 \hat{y}_l \hat{d}_1 + d_2 \hat{y}_l \hat{d}_2 - 1/2 (\mathbf{d} C_s \mathbf{d}^T) \hat{y}_l \hat{n} \\ z_l &= \mathbf{s}(\mathbf{d}) \hat{z}_l = d_1 \hat{z}_l \hat{d}_1 + d_2 \hat{z}_l \hat{d}_2 - 1/2 (\mathbf{d} C_s \mathbf{d}^T) \hat{z}_l \hat{n} \end{aligned} \quad (5.59)$$

If we introduce **coordinate transformation matrices** as

$$K_l = \begin{pmatrix} \hat{x}_l \hat{d}_1 & \hat{x}_l \hat{d}_2 \\ \hat{y}_l \hat{d}_1 & \hat{y}_l \hat{d}_2 \end{pmatrix}, \quad l = i, r, t, \quad (5.60)$$

equation (5.59) can be split into two terms:

$$\begin{aligned} \mathbf{r}_l &= K_l \mathbf{d} - \frac{1}{2} (\mathbf{d} C_s \mathbf{d}^T) \cdot \begin{pmatrix} \hat{x}_l \hat{n} \\ \hat{y}_l \hat{n} \end{pmatrix} \\ z_l &= d_1 \hat{z}_l \hat{d}_1 + d_2 \hat{z}_l \hat{d}_2 - \frac{1}{2} (\mathbf{d} C_s \mathbf{d}^T) \hat{n} \hat{z}_l \end{aligned} \quad (5.61)$$

Ignoring second order term for the transversal coordinates [28] and substituting the result into equation (5.58), we obtain:

$$\begin{aligned} \phi_l &= -k_l \left((\hat{z}_l \hat{d}_1) d_1 + (\hat{z}_l \hat{d}_2) d_2 - \frac{1}{2} (\mathbf{d} C_s \mathbf{d}^T) \hat{n} \hat{z}_l + \frac{1}{2} (K_l \mathbf{d})^T Q_l(z_l) (K_l \mathbf{d}) \right) \\ &= -k_l \underbrace{((\hat{z}_l \hat{d}_1) \hat{d}_1 + (\hat{z}_l \hat{d}_2) \hat{d}_2)}_{p_l} (d_1 \hat{d}_1 + d_2 \hat{d}_2) - \frac{1}{2} k_l \mathbf{d}^T \underbrace{(K_l^T Q_l(z_l) K_l - C \hat{n} \hat{z}_l)}_{\Gamma_l} \mathbf{d}. \end{aligned} \quad (5.62)$$

Here p_l is a projection of the beam direction \hat{z}_l on a plane that is tangential to the surface at the point of incidence. Since the beam radii are much smaller than the radii of curvature of the surface we can assume that Q_l is constant on a surface and is equal to its value at the point of incidence.

Linear and quadratic terms of the complex phases should be matched separately. The linear term confirms Snell's law and the quadratic term allows the equations for the complex radius of curvature tensor of reflected and transmitted beams to be obtained:

$$k_i \Gamma_i = k_r \Gamma_r = k_t \Gamma_t, \quad (5.63)$$

which yields:

$$Q_r = (K_r^T)^{-1} (K_i^T Q_i K_i - C(\hat{n} \hat{z}_i - \hat{n} \hat{z}_r)) K_r^{-1}, \quad (5.64)$$

$$Q_t = \frac{n_1}{n_2} (K_t^T)^{-1} (K_i^T Q_i K_i - C(\hat{n} \hat{z}_i - \frac{n_2}{n_1} \hat{n} \hat{z}_t)) K_t^{-1}. \quad (5.65)$$

Therefore we derived the equations for the complex radius of curvature tensor of reflected and refracted beams for the case of an arbitrary 3D surface, approximated by a quadratic equation. Lenses and other multi-surface structures can be analyzed by considering multiple reflections and refractions from each of the surfaces that make up such structures.

Equations (5.64) and (5.65) do not only correct the typos in [11], but also allow different possible notations for beam-fixed and surface-fixed coordinate systems. Only the beam directions \hat{z}_l and surface normal (\hat{n}) at the point of incidence should stay fixed, while transversal coordinate vectors ($\hat{x}_l, \hat{y}_l, \hat{d}_1, \hat{d}_2$) can be chosen arbitrarily in the plane that is tangential to the surface at the point of incidence. We also believe that using the given vector notation is more reliable than substituting angles of incidence, reflection and refraction since it does not require sign checks.

Experimental verification of the general astigmatic Gaussian beam model

TAKING into account the configuration of general astigmatic beam, investigated in Chapter 5, one of the obvious ways to verify the general astigmatic Gaussian beam model experimentally is to compare the evolution of the intensity ellipse ellipse obtained in simulation and in experiment.

In this chapter I will introduce the experiment, where the simple astigmatic beam is transformed into a general astigmatic by two cylindrical lenses. Then the light spots at different distances behind the second lens are measured with a charge-coupled device (CCD) and compared to the simulation results. Apart from the plain comparison this work includes the search of the setup that produces a beam with the clearly visible properties of general astigmatism in the observation region. In order to minimize the effect of measurement uncertainties of the individual parameters of the setup we then fitted these parameters to the measured beam intensity distributions.

The experiment has been performed by Dennis Schmelzer [30], the simulations were done by myself. Within this chapter there are deviations from the results presented in [30]. This is due to the fact that a lot more simulation analysis has been performed after the thesis was written by Dennis Schmelzer. Thus, this work represents a refinement, which results in small differences in some numbers and graphs. However, the results presented in [30] are very similar to the ones given in this chapter and the major conclusions stay unaffected.

I will start this chapter with the general schematic of the experiment provided in Section 6.1. I will talk about the main components and their features and about the measurement technique. Section 6.2 will include the approach to the comparison of the measured and simulated data. It will discuss the difficulties and the criteria of

the good agreement between the theory and the experiment. I will also introduce the procedure of fitting individual measured parameters to the measured data. In Section 6.3 I will talk about the first measurements, made with a simple approach. Then I will give an overview of a procedure for finding an optimal setup for the comparison. I will explain what setup and why do we consider an optimal and how do we choose it from the number of different possibilities. With the new optimal setup two other sets of measurements have been performed. The results of these measurements compared to the simulation will be presented in Section 6.5 and Section 6.6. In Section 6.7 I will discuss the results of the comparison so far and the way forward in the field of experimental verification of the general astigmatic Gaussian beam model.

6.1. General setup

Within this thesis I emphasized that general astigmatic Gaussian beam can be produced from stigmatic and simple astigmatic beams in the optical system that contains only two spherical lenses. However, using such a system in the comparison of the light spots is not efficient due to the fact that it produces the general astigmatic beams with a small ellipticity of the intensity pattern. The easiest way to achieve high ellipticity is to use strongly astigmatic components in the optical system. An example of such a component is a cylindrical lens. In order to produce a general astigmatic beam from stigmatic two cylindrical lenses are needed. The first lens will transform stigmatic beam into simple astigmatic. The second lens will transform simple astigmatic beam into general astigmatic if the principal axes of the simple astigmatic beam are not aligned with the principal axes of the lens. This is the case if the second lens is aligned at an oblique angle to the first one in the plane, orthogonal to the axis of propagation.

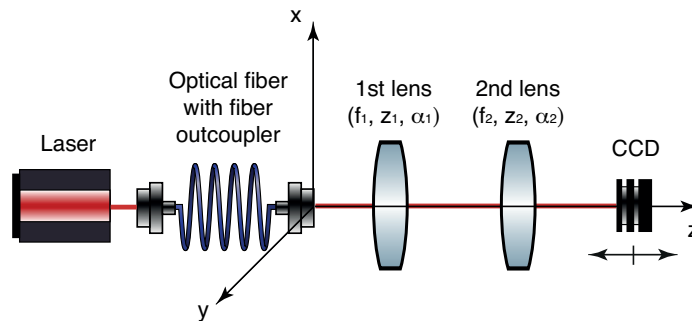


Figure 6.1.: A simplified schematic of experiment. The output from a laser was coupled into a fiber acting as a special mode filter. First, the beam exiting the fiber was characterized using the CCD camera, then two cylindrical lenses (focal length f_i , distance to fiber collimator z_i , angle α_i to y -axis) were inserted and the resulting beam intensity pattern was measured with the CCD camera at different positions behind the second lens.

In Figure 6.1 the schematic of the experimental setup is shown. The light from a laser (Mephisto 500 by Coherent [31]) with a wavelength of $\lambda = 1064 \text{ nm}$ was coupled

into a single-mode polarisation-maintaining fiber with angle-polished connectors, that acted as a spatial mode filter. The light emitted by the fiber was collimated with an aspherical lens with 11 mm focal length (60FC-4-A11-03 by Schäfter und Kirchoff [32]). The principal beam radii w_1 and w_2 and the angle of orientation φ_{w0} of the intensity ellipse with respect to the camera-fixed coordinate system were measured at several distances z_j from the fiber collimator using the WinCamD-UCD23 by Dataray [33].

The waist radii w_{01} and w_{02} and distances between fiber collimator and waists z_{01} and z_{02} were obtained using least-square fit of the beam radii evolution described as

$$w_i(z) = w_{0i} \sqrt{1 + \left(\lambda \frac{z - z_{0i}}{\pi w_{0i}^2} M_i^2 \right)^2}, \quad i = 1, 2. \quad (6.1)$$

to the measured beam radii $w_i(z_j)$, $i = 1, 2$. The **beam propagation factor** M^2 characterizes the beam quality or the deviation of the initial beam from Gaussian beam in fundamental mode [34, p. 605], [17, p. 85]. For the ideal Gaussian beam in fundamental mode $M^2 = 1$. The beam propagation factors in the simulations discussed in this chapter were always set to 1 and thus the initial beam was always considered to be simple astigmatic Gaussian beam in the fundamental mode. However, I will leave the M^2 factors in the list of parameters of the initial beam for completeness. The procedure of obtaining the parameters of the initial beam will be discussed in details in the sections where the measurement results are introduced. The parameters of the initial beam are listed in Table 6.1.

Table 6.1.: The list of parameters of the initial beam.

λ	optical wavelength
z_{01}	waist position in XZ -plane
z_{02}	waist position in YZ -plane
w_{01}	waist size in XZ -plane
w_{02}	waist size in YZ -plane
φ_{w0}	beam orientation in XY -plane
M_1^2	beam propagation factor in XZ -plane
M_2^2	beam propagation factor in YZ -plane

After an initial simple astigmatic beam was fully characterized we transformed it into a general astigmatic beam using two cylindrical lenses, tilted with respect to each other in the transversal plane xy . The lenses were placed at distances z_1 and z_2 from the fiber collimator and tilted by angles α_1 and α_2 around the optical axis ($\alpha_j = 0$ stands for no curvature in the horizontal direction). Their focal lengths were f_1 and f_2 respectively.

After the general astigmatic beam was produced, its intensity profile was characterised using the same CCD camera at different distances behind the second lens. From this characterisation we obtained principal beam radii w_1 and w_2 and the angles of the beam ellipse φ_w at different positions along the optical axis z .

6.1.1. Cylindrical lenses

Within our investigations we had three different cylindrical lenses available. Their parameters were unknown and we measured them by ourselves. In this subsection I will describe the characterization procedure that we used. In the end I will provide the resulting parameters of all three lenses.

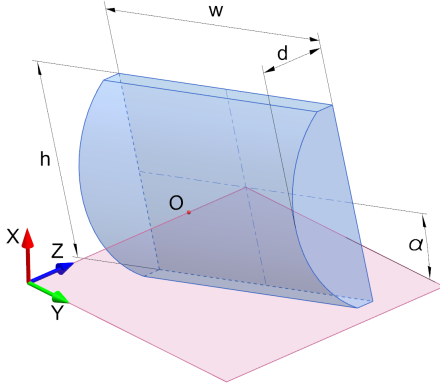


Figure 6.2.: Cylindrical lens and its geometrical parameters: height h , width w , thickness d , orientation in the transversal plane α .

It shows the connection between the curvatures of two surfaces of the lens. For the plano-convex lenses this parameter can have values of 1 if the plane surface is a front surface facing the incident beam and -1 in the other case. For biconvex lenses with equal curvatures on front and back surfaces asymmetry parameter is zero.

For both front and back surfaces of the cylindrical lens the curvature in one of the transversal directions is zero. The curvatures in the other two directions are equal (c_1 for front surface and c_2 for back surface). Then we can use the usual **lensmaker's equation** [16, chapter 6], [21] to obtain the required principal curvature of the front and the back surfaces of the cylindrical lens:

$$\frac{1}{f} = (n - 1) \left(c_1 + c_2 - \frac{n - 1}{n} d c_1 c_2 \right). \quad (6.2)$$

In order to solve this equation for c_1 and c_2 additionally an **asymmetry condition** is required [21]:

$$a = \frac{c_2 - c_1}{g}, \quad (6.3)$$

where

$$g = \frac{1}{f(n - 1)} = c_1 + c_2 - \frac{n - 1}{n} d c_1 c_2. \quad (6.4)$$

Once the lens is placed in the setup two more parameters are of interest: lens position z along the optical axis and the angle of the lens orientation in the transversal plane α . Zero angle corresponds to zero principal curvature in the horizontal direction. The sketch of cylindrical lens and its geometrical parameters is given in Figure 6.2. The complete set of cylindrical lens parameters is given in Table 6.2. These parameters were measured in a lab for all three lenses. The results of these measurements were implemented in the simulation, where they were used to refract the ingoing beam on a lens surface using equation (5.65).

Table 6.2.: Parameters of a cylindrical lens (cf. Figure 6.2).

h	height
w	width
d	thickness
f	focal length
a	asymmetry parameter
n	refractive index
z	position along the optical axis
α	transversal angle of orientation

All three lenses we had in our study were made of fused silica (refractive index $n = 1.44963$ at a wavelength $\lambda = 1064$ nm). Linear sizes of lenses (height, width and thickness) were measured accurately. Height and width do not affect neither experimental, nor simulation results. Only the thickness is involved into the beam transformation. Since all three parameters were well defined, we assumed no tolerances for them later on in the fit. The values of these parameters for all three lenses are listed in Table 6.3.

Table 6.3.: Linear sizes of cylindrical lenses.

Parameter	Unit	Lens1	Lens2	Lens3
h	[mm]	50	20	30
w	[mm]	50	60	60
d	[mm]	5.5	3	6.5

The asymmetry parameter of biconvex Lens3 is equal to zero. The plano-convex Lens1 and Lens2 can have the asymmetry parameter a to be either 1, or -1, depending on which surface (planar or convex) faces the ingoing beam.

The most important lens parameter in our calculations was the focal length, which allows to compute the curvature matrix of the surface. This parameter was measured by illuminating the lens with a flashlight and measuring the distance of the arising focus. This method has a limited accuracy and we assumed an error of up to 10% for each measurement. As we will see later, this fact made the focal length the major source of errors in our comparison.

The focal length was measured with visible light ($\lambda_{\text{visible}} = 480$ nm). In the simulations we need the focal length for the wavelength of $\lambda_{\text{laser}} = 1064$ nm. From the

lensmaker's equation for this lens [16, chapter 5]

$$\frac{1}{f} = (n - 1)(c_1 + c_2) \quad (6.5)$$

it follows that

$$\frac{f_{\text{laser}}}{f_{\text{visible}}} = \frac{n_{\text{visible}} - 1}{n_{\text{laser}} - 1}. \quad (6.6)$$

Fused silica has refractive index $n_{\text{visible}} = 1.4635$ for visible light and refractive index $n_{\text{laser}} = 1.44963$ for laser light. Therefore,

$$f_{\text{laser}} = 1.030848 f_{\text{visible}}. \quad (6.7)$$

The focal length of the first lens was measured only once and therefore has a tolerance $\sigma(f)$ of 10%. The focal lengths of the second and third lenses were measured independently two times. Each measurement has a tolerance $\sigma(f) \approx 10\%(f)$. Therefore for the average of the two measurements is defined as:

$$\sigma^2(\bar{f}) = \sigma^2\left(\frac{1}{2}(f^1 + f^2)\right) = \frac{1}{4}\sigma^2(f^1) + \frac{1}{4}\sigma^2(f^2) + \frac{1}{2}\text{cov}(f^1, f^2). \quad (6.8)$$

Since they are independent and $\sigma(f_1) = \sigma(f_2) = \sigma(f) \approx 10\%$, the tolerance of the average value of the two measurements is given by

$$\sigma(\bar{f}) = \frac{\sigma(f)}{\sqrt{2}} \approx 7\%(f). \quad (6.9)$$

The results of both measurements (f^1 and f^2) are listed in a table 6.4. We used the average values (\bar{f}) of the two measurements in the simulations, since they have smaller tolerances $\sigma(\bar{f})$ than each individual measurement.

Table 6.4.: Measured focal lengths of cylindrical lenses and tolerances of these measurements. The upper indices show the number of the measurement. A bar indicates averaging of all measurement results for this value. The values that will be used in the simulations are shown in bold.

Parameter	Unit	Lens1	Lens2	Lens3
f^1	[mm]	361	62	52
f^2	[mm]	-	71	55
$\sigma(f)$	[mm]	± 35	± 6	± 5
$\bar{\mathbf{f}}$	[mm]	361	66.5	53.5
$\sigma(\bar{\mathbf{f}})$	[mm]	± 35	± 4.2	± 3.5

For the position z of the lens in a setup we assumed a tolerance of 1 mm. The transversal angle α of the lens in a setup can be measured up to 1° .

6.1.2. Charge-coupled device (CCD) camera

The charge-coupled device (CCD) camera is used to measure the intensity profile of the beam [17, p. 85]. In our investigations we used the beam profiling camera WinCamD-UCD23 by Dataray [33] with a CCD-sensor. This camera is suitable for the wavelengths in the range from 350 to 1150 nm. The sensor area is 8.8 mm \times 6.6 mm. However, in order to have the entire intensity profile on the sensor and to perform accurate measurements with the camera the beam radii should not exceed 1.25 mm. The minimal possible beam diameter that corresponds to 10 pixels on a sensor is 65 μ m [33].

Table 6.5.: The list of parameters of the CCD camera.

l	longitudinal offset
β	angular offset

In the simulation we have to include two parameters related to the CCD camera. A chip depth from the front of case produces a longitudinal offset l of 7.2 mm in our case. The maximum possible tolerance given in the datasheet of a camera is ± 0.5 mm. However, the measurement from the fiber outcoupler (or from the second cylindrical lens) to the front of case of a camera is also performed with some tolerance. Therefore, we will assume a tolerance of 1 mm for the longitudinal offset. The second parameter that has to be introduced is the transversal angle of the camera with respect to the global coordinate system β . The camera was aligned to the global coordinate system, but its small residual tilt around the z axis has to be accounted for. For this angle we assume a tolerance of $\pm 1^\circ$. The description of the parameters related to the CCD camera is given in Table 6.5. The summary of values and tolerances of these parameters can be found in Table 6.6.

Table 6.6.: The values of the parameters of the CCD camera and their tolerances.

Parameter	Unit	Value	Tolerance
l	[mm]	7.2	± 1
β	[degree]	0	± 1

CCD camera makes a snapshot of the intensity profile at a given point of the beam axis. Then its software defines the principal beam radii w_1 and w_2 and the angle of orientation φ_w of the intensity ellipse with respect to the camera-fixed coordinate system at this point. The intensity profile can be measured in several points along the beam axis. Then the curves $w_1(z)$, $w_2(z)$ and $\varphi_w(z)$ can be constructed and fitted to the desired beam model.

6.2. Comparison of experimental and simulated results

The procedure of the comparison of experimental and simulated results seems to be obvious. In the first step one needs to measure the required parameters and plug them in the simulation. In the next step one needs to perform the measurement of interest and run the corresponding simulation. Then, finally, one can compare the results obtained from the experiment and simulation. However, in reality it's not that simple. The initial parameters required by the simulation can only be measured with some tolerances. It leads to deviations between simulated and experimental results. In order to conclude that the reached agreement is sufficient we decided to fit the simulation results to the experiment by varying the initial parameters within the measurement tolerances. This was done by the special simulation that minimized the average deviation between the measured and simulated values.

The complete set of the initial parameters of the experimental setup includes the parameters listed in Table 6.1 and Table 6.5. The lens parameters from Table 6.2 must be given for each of the two cylindrical lenses in the setup. Each of these parameters has its measurement tolerance. However, we don't need to include all of them in the fit.

Within the investigation described in this chapter we assumed that the optical wavelength λ of the beam, as well as refractive indices n and asymmetry parameters a of all lenses are well-known and do not need to be varied. We also did not include the M^2 factors in the simulation. As I will show in subsequent sections, using simple astigmatic Gaussian beam in fundamental mode in the simulations allows very good fits to the measurements. This indicates that the higher order modes that caused M^2 factors to be greater than 1 do not seem to have a notional effect. The linear sizes of lenses (height h , width w and thickness d) were also not varied in a fit since height and width do not influence the beam transformation and the thickness was accurately measured. Additionally, from equation (6.4) it follows that thickness variations are residual if the focal length is varied. Variations of the transversal angle of the first lens in the setup α_1 cause the same effect as the variations of the transversal angle of the initial beam φ_{w0} . Thus only one of these parameters should be included in the fit. We chose to vary the beam angle φ_{w0} . Similarly changes of the first lens position z_1 can not be distinguished from changes of waist positions in both principal planes of the initial simple astigmatic beam z_{0x} and z_{0y} . We vary the waist positions in the fit. Therefore, for each measurement the following parameters are varied in a fit: focal lengths of both cylindrical lenses in a setup (f_1 and f_2), longitudinal position (z_2) and the angle (α_2) of the second lens, waist radii (w_{01} and w_{02}) and waist positions (z_{01} and z_{02}) of the initial beam in its principal planes, transversal angle (φ_{w0}) of the initial beam with respect to the global coordinate system, longitudinal (l) and angular (β) offsets induced by the CCD camera.

The residual parameters were not included in the fit. However, as I will show in the next section, if the individual parameters that are used in the fit are varied separately one by one, variations of different parameters can cause similar effects in the results.

Thus, the fit might not be unique in all cases. However, the fit always answers the question how well the experimental and simulated results can agree within the current measurement uncertainties.

6.3. First measurements with manually defined setup

The first comparison was performed with a heuristically obtained setup. The only criterion for the setup choice was the beam size limitation conditioned by the CCD camera restriction discussed above. This criterion has to be fulfilled at every point along the beam path, where beam intensity was measured with the camera.

In this section I will first describe the procedure of initial beam characterization. Then I will introduce the lens configuration that was chosen for the first measurements. Afterwards I will show the results of the comparison of the simulated and measure data and discuss the impact of each individual parameter variation.

6.3.1. Characterization of the initial beam

In order to characterize the initial simple astigmatic beam several measurements of its intensity profile were performed using a CCD camera. These measurements were made within a Rayleigh range from the waist to guarantee an accurate beam characterization. From each measurement of the intensity ellipse the camera software automatically extracted its principal axes w_1 and w_2 . Then waist radii w_{01} , w_{02} and waist positions z_{01} , z_{02} were found by fitting beam radii evolutions (see equation (6.1)) to the measured beam radii $w_i(z_j)$, $i = 1, 2$. The angle of orientation of the simple astigmatic initial beam φ_{w0} is constant along the beam axis and can be found from the single measurement of the intensity ellipse.

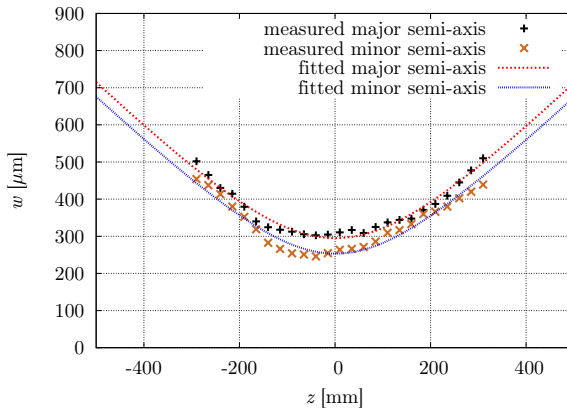


Figure 6.3.: Characterization of the beam. Gaussian curve is fitted to the measured beam radii separately for two principal semi-axes of the simple astigmatic beam.

The evolution of the initial beam in the first measurements is shown in Figure 6.3.

Black plusses and brown crosses represent the measured values of the principal semi-axes of the intensity ellipses at different points along the propagation. Red and blue lines indicate the corresponding fitted curves.

The parameters of the initial beam together with their standard errors and confidence interval, obtained in the fit are given in Table 6.7. The values of these parameters correspond to the red and blue lines in Figure 6.3. Standard errors show the range where each parameter value most probably lies. However, this value can also lie within a confidence interval. Therefore, taking confidence interval as the tolerance in the fit is more secure.

Table 6.7.: The parameters of simple astigmatic beam obtained by fitting Gaussian curves into the measured beam radii.

Parameter	Units	Value	Standard error	Confidence interval
z_{01}	[mm]	1.02	± 3.6	± 10.2
z_{02}	[mm]	0.82	± 4.3	± 12.3
w_{01}	[μm]	295	± 4.3	± 12.2
w_{02}	[μm]	253	± 5.4	± 15.2
M_1	[1]	1.06	± 0.008	± 0.024
M_2	[1]	0.97	± 0.01	± 0.027

Both M^2 -factors are sufficiently close to one and can be neglected within a comparison.

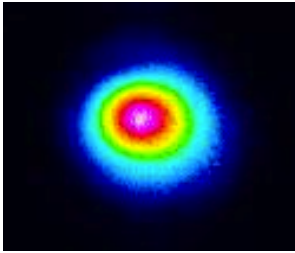


Figure 6.4.: Intensity profile of the initial beam at a position close to the waist.

The orientation φ_{w0} of the initial simple astigmatic beam was measured several times. Due to the fact that the beam is close to circular ($w_{0x}/w_{0y} = 1.17$) and it doesn't have an ideal Gaussian profile (see Figure 6.4) the camera software could not determine this value accurately. The results from different measurements varied. Thus, we assumed the nominal value for the beam angle to be $\varphi_{w0} = 0$ and the measurement tolerance to be $\pm 10^\circ$.

6.3.2. Manually defined lens configuration

Every configuration of the two cylindrical lenses, oriented at an oblique angle with respect to each other in the transversal plane, transforms a stigmatic or a simple astigmatic beam into general astigmatic beam. In the beginning we chose a random configuration of the two lenses out of three available. The only restriction imposed was the limitation of the resulting general astigmatic beam radius. It could not exceed 1.25 mm (CCD camera restriction discussed above) in any of the transversal directions within the propagation distance, sufficient to perform several measurements of the

intensity ellipse at different points along the optical axis. We made measurements within a distance of about 20 cm behind the second lens.

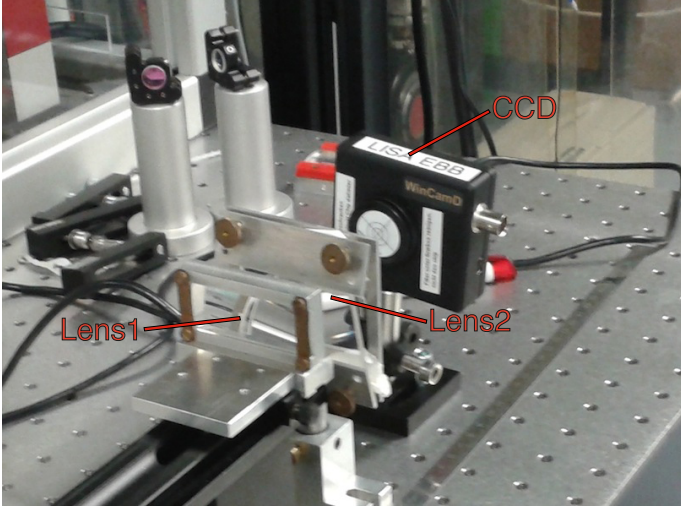


Figure 6.5.: Lab photograph of the manually defined setup.

The manually defined lens configuration that fulfilled the limitation above was found and used in first measurements. It included the first two cylindrical lenses out of three described above. The lenses were oriented almost orthogonally to each other. Both of them were plano-convex, and within this setup were oriented such that the curved surface was facing the incoming beam. The photograph of this lens configuration is shown in Figure 6.5. The parameters of the setup are listed in Table 6.8. As described in Section 6.1, parameter z shows the distance from the fiber outcoupler to the front surface of the lens, angle α shown the orientation of the lens in the transversal plane such that zero angle corresponds to zero principal curvature in the horizontal direction.

Table 6.8.: The parameters of the manually defined lens configuration.

Name	Orientation (a)	z [cm]	α [degree]
Lens2	convex-plane (-1)	13	0
Lens1	convex-plane (-1)	16	81

6.3.3. Measurement results

Three sets of measurements were performed with the initial beam and manually defined setup described above. All three showed similar results. Right behind the second lens, where we expect a general astigmatic beam to be formed, the elliptical intensity profile was aligned horizontally. Then it transformed into a nearly circular light

spot. At a distance of about 10 cm behind the second cylindrical lens the intensity profile obtained vertical orientation, which was preserved as the beam propagated further. The selection of snapshots from the CCD camera, illustrating these results, is shown in Figure 6.7. Thus, within this case the expected rotation of the intensity ellipse cannot be easily seen from the pictures, produced by the camera. Major and minor semi-axes can switch their principal directions in simple astigmatic case (see Chapter 4). Therefore, it is hard to say if the measured beam is indeed general astigmatic.

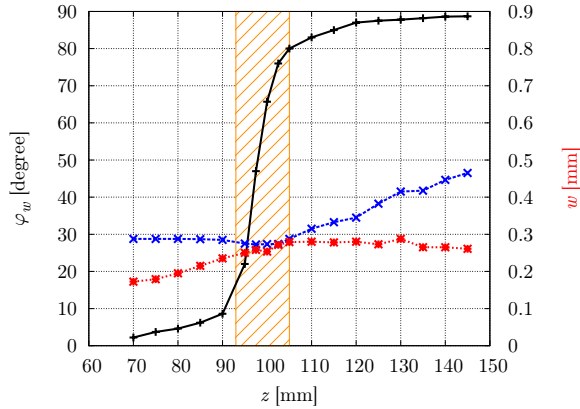


Figure 6.6.: The measured evolution of orientation (in black) and major and minor semi-axes (in blue and red) of the intensity ellipse as beam propagates behind the second lens of the manually defined setup. Dashed area highlights the region of maximal rotation and minimal ellipticity of the light spot.

For each snapshot of the beam profile the dedicated camera software computes the principal semi-axes and the orientation of the beam ellipse. If we plot these results, we obtain the graph in Figure 6.6. This graph shows that intensity ellipse indeed tilts along the propagation, but the major changes in its orientation correspond to approximately 1 cm long region, where the beam is nearly circular. Thus the resulting beam behind the second lens is general astigmatic, which agrees to the theoretical expectations. Even though it is hard to see the rotation of the intensity ellipse, we can use this beam for the first comparison of the experimental and simulated light spot evolutions.

6.3.4. Fit of the intensity ellipse angle evolution

The fits were performed separately for each of the three measurements made with the manually defined setup. There was a time gap between the measurements and the setup was reconstructed for each of them. However, the goal was to build the identical setup described in Table 6.8 in all measurements. Thus, the initial parameters describing cylindrical lenses and their configuration did not change from one fit to another, but in reality they could have differed within measurement tolerances. The

initial simple astigmatic beam was configured and characterized once before the first of the three measurements and was not changed since then. Still we expect that some minor deviations could have occurred. Therefore, all initial parameters used in the simulation are identical for all three fits. However, it is expected that the resulting fitted parameters may vary from one fit to another.

Figure 6.9 illustrates the results of the comparison of the simulated and measured intensity ellipse orientations for the manually defined setup. In red is the so-called nominal simulated curve corresponding to the measured values of the setup parameters. This line is identical in all three graphs. Black plusses illustrate the measurement points, obtained from the CCD camera software. It is easy to see that they form similar, but not identical curves from one measurement to another. In blue are simulated curves corresponding to the best found fit of the setup parameters to the measurement results. In all three cases they follow the measurement points very closely. This means that it was possible to find a set of the setup parameters within their measurement tolerances that results in accurate theoretical description of the experimental observations.

The results of all three fits are summarized in Table 6.9. It includes all the complete set of parameters of the setup that took part in the fit with their measured values, tolerances and fitted values. As expected, the values of the setup parameters resulting from different fits are not identical. However, the fitted values of both focal lengths and one of the waist sizes changed only slightly from one fit to another. All other parameters of the initial simple astigmatic beam differ. The fit with so many parameters is not necessarily unique. This hypothesis will be discussed separately later. The geometrical parameters of the setup such as the second lens position and angle, longitudinal and angular offsets, do not have to agree in different fits since the setup was reconstructed before each set of measurements.

The fit performance can be evaluated using the average absolute difference between the measured and simulated intensity ellipse angle at identical positions. The initial average difference $\Delta_{\text{nominal}}^{\varphi}$ is defined as

$$\Delta_{\text{nominal}}^{\varphi} = \left[\sum_{i=1}^n (\varphi_{wi}^m - \varphi_{wi}^n)^2 / n \right]^{1/2}, \quad (6.10)$$

where φ_{wi}^m are the measured values of the intensity ellipse angle, φ_{wi}^n are the corresponding values of the intensity ellipse angle obtained from the simulation with the nominal values of all parameters. Analogously the fitted average difference $\Delta_{\text{fitted}}^{\varphi}$ is given by

$$\Delta_{\text{fitted}}^{\varphi} = \left[\sum_{i=1}^n (\varphi_{wi}^m - \varphi_{wi}^f)^2 / n \right]^{1/2}. \quad (6.11)$$

Here φ_{wi}^f are values of the intensity ellipse angle produced by the simulation with the fitted parameter values. In Table 6.9 both average differences are given for each of the three measurements. The initial average difference $\Delta_{\text{nominal}}^{\varphi}$ is in the order of tens of degrees for all measurements. This means that in average the measured

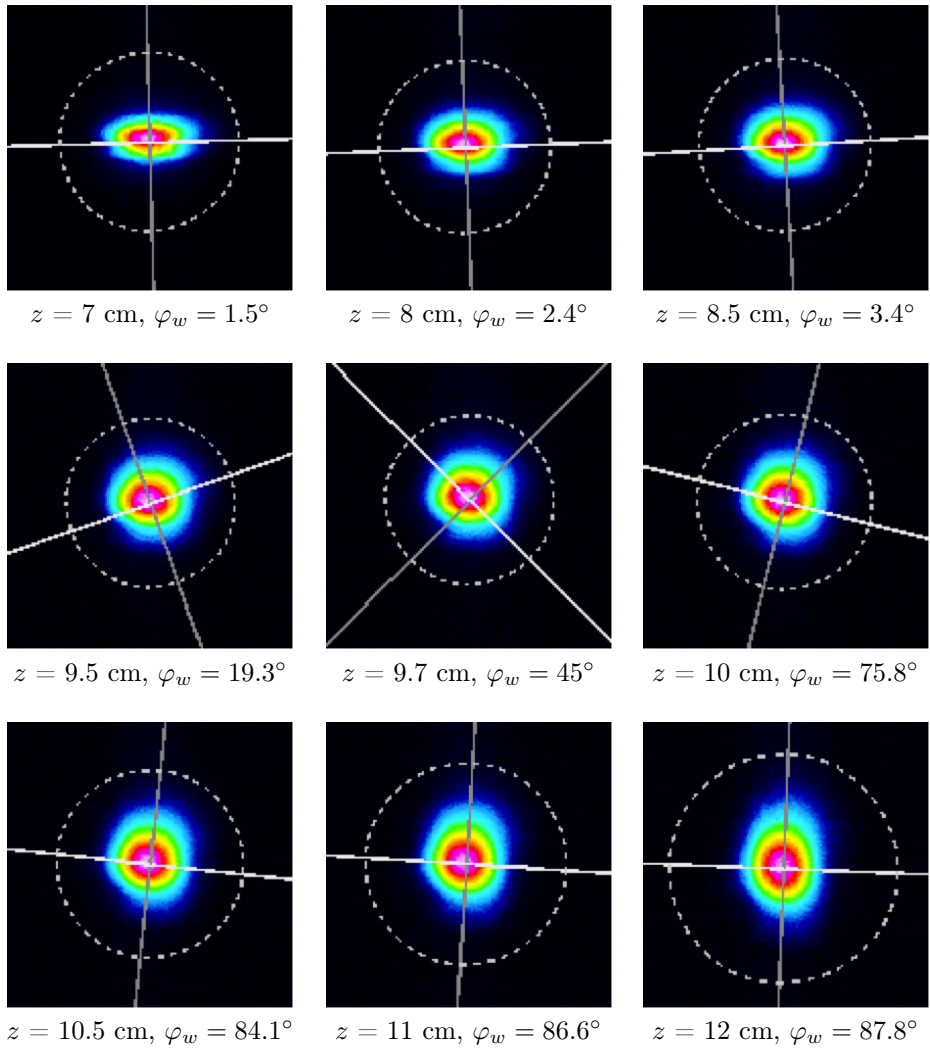


Figure 6.7.: The evolution of intensity ellipse of the general astigmatic beam produced by the manually defined setup. Snapshots from the CCD camera taken at different distances z behind the second cylindrical lens. The orientation φ_w of each intensity ellipse was defined by the CCD camera software.

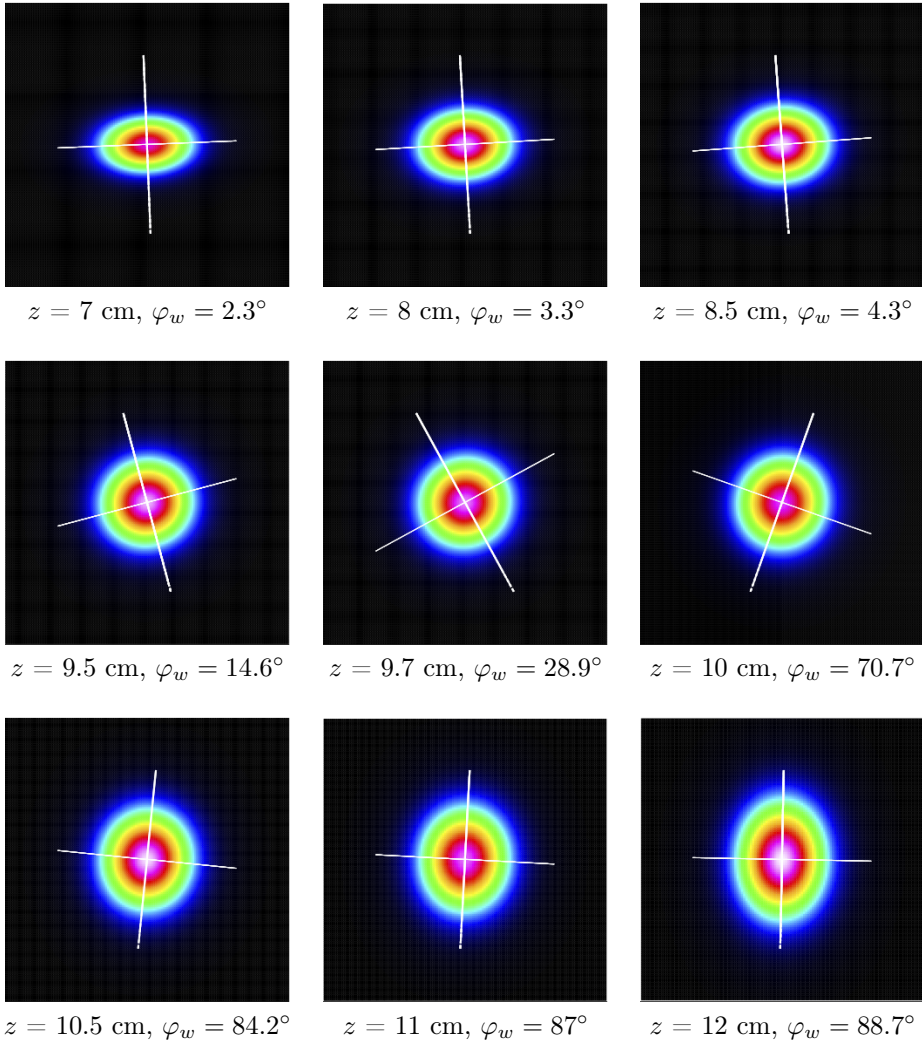


Figure 6.8.: The evolution of intensity ellipse of the general astigmatic beam produced by the manually defined setup. Snapshots from the simulation fitted to the third measurement. The value of z shows the distance behind the second cylindrical lens. The value φ_w is the angle of orientation of the intensity ellipse.

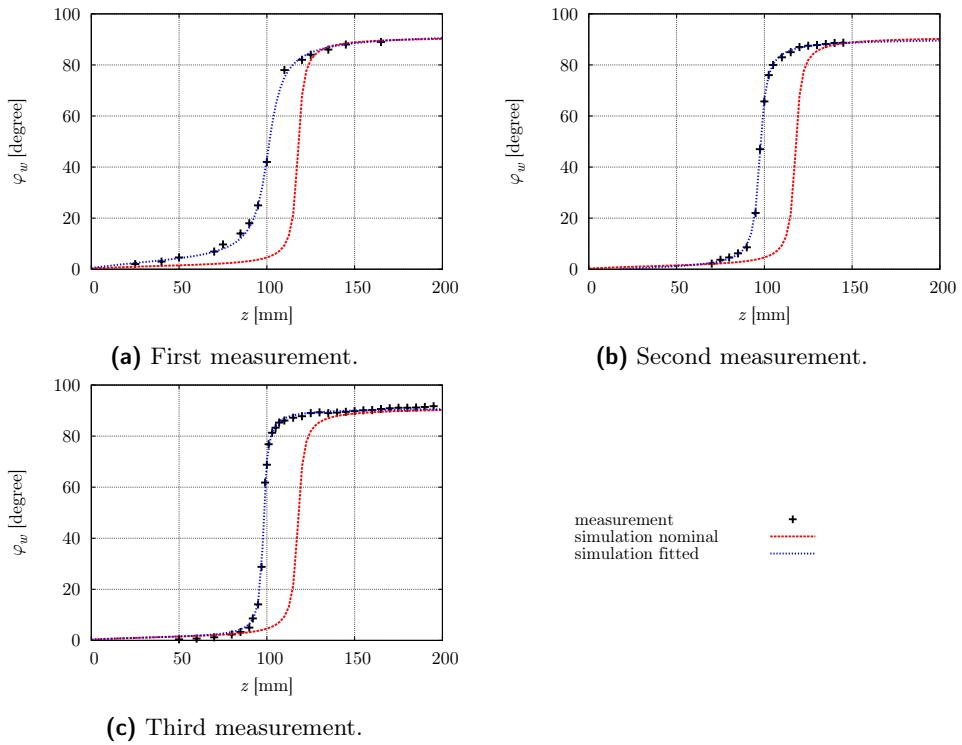


Figure 6.9.: The evolution of intensity ellipse orientation as beam propagates behind the second lens of the manually defined setup. Black pluses illustrate the measurement points, red curve results from the simulation with the measured parameters of the setup, blue curve results from the simulation with the fitted parameters of the setup.

angle at some point along the beam axis deviates from the simulated angle by tens of degrees. This is clearly a large difference, but if we look at graphs in Figure 6.9, we can see that it results from the longitudinal shift between the curves, which is then eliminated by fit. The average difference $\Delta_{\text{fitted}}^{\varphi}$ for fitted curves (see Table 6.9) is in the order of one degree in all three cases. This value lies within (or even exceeds) a measurement accuracy of the intensity ellipse orientation.

Table 6.9.: Measured and fitted parameters of the manually defined setup. The deviation between the measurement and simulation with the measured parameter values is given by $\Delta_{\text{nominal}}^{\varphi}$. Similar deviation for the fitted parameter values is given by $\Delta_{\text{fitted}}^{\varphi}$.

Parameter	Units	Value	Tolerance	Fit 1	Fit 2	Fit 3
f_1	[mm]	66.5	± 4.2	62.11	62.3	62.3
f_2	[mm]	361	± 35	326	326	327
z_2	[mm]	160	± 1	161	161	161
α_2	[degree]	81	± 1	79.98	82	81.9
w_{01}	[μm]	295	± 12.2	307.6	307.3	307.2
w_{02}	[μm]	253	± 15.2	255.4	269	268
z_{01}	[mm]	0.82	± 10.2	5.66	11.02	6.4
z_{02}	[mm]	1.01	± 12.3	13.7	10.94	-8.62
φ_{w0}	[degree]	0	± 10	-10	-3.75	0.79
l	[mm]	7.2	± 1	8.2	8.2	8.1
β	[degree]	0	± 1	1	-0.92	0.1
$\Delta_{\text{nominal}}^{\varphi}$	[degree]			21.9	38.2	33.7
$\Delta_{\text{fitted}}^{\varphi}$	[degree]			1.27	0.73	1.07

Fit has helped us to obtain a good agreement between measured and simulated orientation of the intensity ellipse in the manually defined setup. However, there are still some questions to answer. One of them is to find an explanation of the significant disagreement between the measurement results and simulated results with nominal parameters. Another remaining question requires understanding of deviations of the initial beam parameters from one fit to another. I will answer both questions in the next section.

6.3.5. Analysis of the impact of individual parameters

It is well-known that from the results of several separate variations of the individual parameters of the simulation it is hard to predict the result of variation of all parameters simultaneously. However, by looking at individual parameter variations it is possible to get a feeling of how big is the impact that they can cause. Such investigation can also help in understanding how much can the simulated curve vary within the given tolerances of individual parameters.

The impact of variation of the offsets induced by the CCD camera (longitudinal offset l and angular offset β) is trivial: the nominal simulated curve (see Figure 6.9) will be shifted horizontally (for longitudinal offset) or vertically (for angular offset)

exactly by the value of the offset variation. For all three graphs in Figure 6.9 the longitudinal shift between the nominal and fitted curves is in the order of cm. The tolerance of each of the offsets is small and thus they can not play a major role in the procedure of the parameter fit.

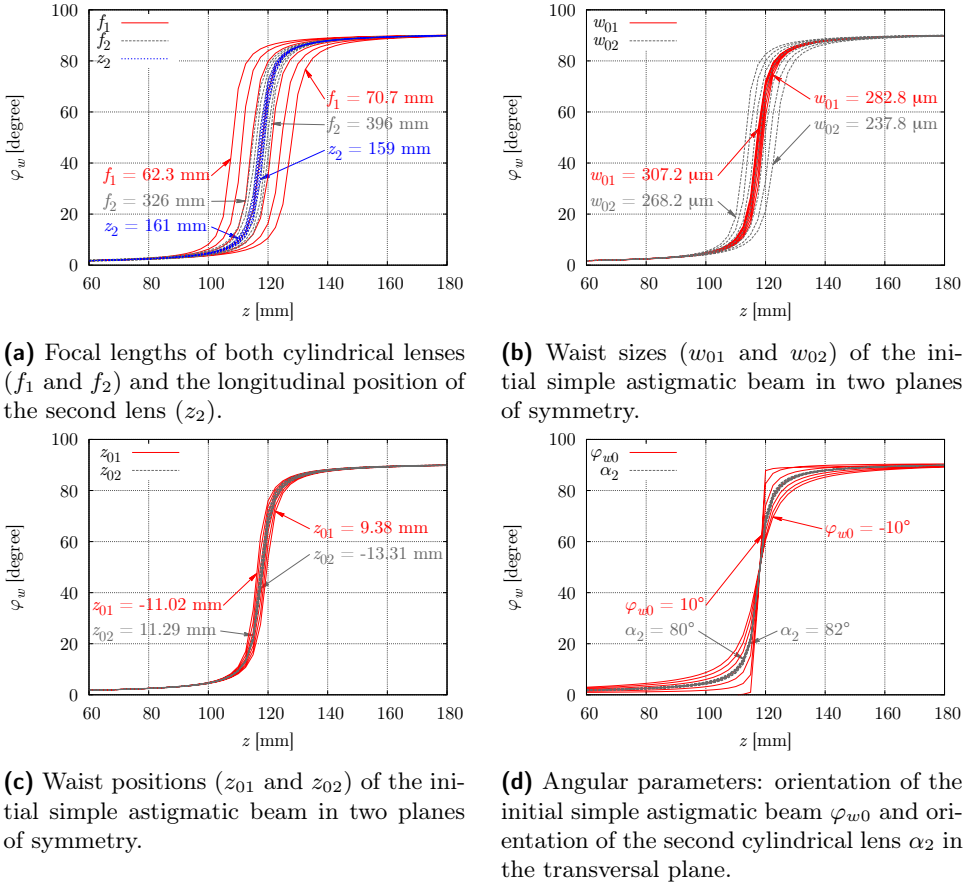


Figure 6.10.: Variation of individual parameters of the manually defined setup in equidistant steps.

Individual variation of most of the parameters of the setup that take part in the fit shifts the nominal simulated curve horizontally. This is true for both focal lengths f_1 and f_2 , longitudinal position of the second lens z_2 (see Figure 6.10a), waist sizes w_{01} and w_{02} (Figure 6.10b) and waist positions z_{01} and z_{02} (Figure 6.10c) of the initial simple astigmatic beam in both of its principal planes. Neither of those parameters significantly effects the slope of the curve. The biggest impact according to the graphs in Figure 6.10 has the uncertainty in the focal length of the first cylindrical lens in the setup. The focal length of the second cylindrical lens has bigger uncertainty. Surprisingly, its variation causes smaller effect. Variation of the waist sizes of the

initial simple astigmatic beam also causes significant shift of the nominal simulated curve. Variation of waist positions and the longitudinal position of the second lens does not seem to produce big effect.

Variation of angular parameters of the setup (orientation of the initial simple astigmatic beam φ_{w0} and orientation of the second cylindrical lens α_2) results in changes of the slope of the nominal simulated curve (see Figure 6.10d). The angle of the second lens does not seem to play a big role in the parameter fit. Uncertainty of the orientation of the initial simple astigmatic beam, in contrary, causes clearly observable changes.

This study shows that variations of individual parameters of the setup cause similar effects and thus it is not surprising that the fit is not unique. This agrees to my observations while running fitting simulation several times for each measurements. The results given in Table 6.9 were chosen by the smallest found value of $\Delta_{\text{fitted}}^\varphi$ from several simulation runs. However, it does not mean that all the parameters of the setup in each of the measurements were exactly equal to the fitted parameters in the table. Another important observation is that variation of some parameters does not cause big changes in the evolution of the intensity ellipse orientation. It explains, for example, why the fitted waist positions vary from one measurement to another. The major source of uncertainty is the imprecise focal length of the first lens. According to Figure 6.10a, it can explain most of the longitudinal shift between the nominal and fitted simulated curves in Figure 6.9. Unfortunately, we could not improve the accuracy of the focal length definition within the scope of this analysis. Another significant factor of uncertainty is the inaccurate value of orientation of the initial beam. Variation of this value causes significant deviations and its fitted value is different in different fits. On the one hand, the laser beam was not changed between the measurements. On the other hand, initial beam tilt is the only parameter that can cause significant changes of the slope of the curve (see Figure 6.10d). As we can see in Figure 6.9, the slope of measured curves is not identical in all three graphs. Thus, it is not surprising that the fitted values of the initial beam angle change from one measurement to another.

6.3.6. Comparison of the intensity ellipse semi-axes

Previously I discussed the comparison and fit of the evolution of the intensity ellipse orientation of the general astigmatic beam. In order to compare the measured and simulated evolutions of the intensity ellipse it is also necessary to compare the evolution of the principal beam radii w_1 and w_2 . Such comparison is illustrated in Figure 6.11. This graph shows that the evolution of both measured and simulated intensity ellipse semi-axes is similar and at every measurement point both principal radii are well below the CCD camera restriction of 1.25 mm. However, the point where the major and minor semi-axes are closest to each other for the nominal simulated curves is shifted with respect to the similar point of measured curves. The fit improves the situation, but even in this case there is significant deviation between measured and simulated values of the principal beam radii. This deviation can be explained by the filters used or inaccuracy of the CCD-camera software. This effect was not

observed later in the measurements, where new camera software and no filters were used.

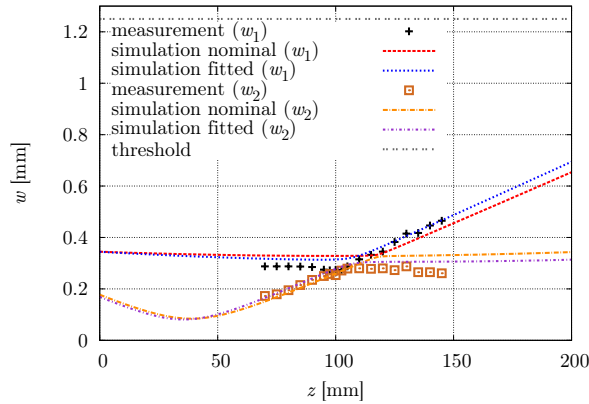


Figure 6.11.: The evolution of principal radii w_1 and w_2 of intensity ellipse of the the general astigmatic beam as it propagates behind the second cylindrical lens of the manually defined setup. Measurement points are taken from the second measurement (Figure 6.9b). The threshold shows the CCD camera restriction of 1.25 mm.

6.3.7. Comparison of intensity distributions

The comparison of the evolutions of the orientation and semi-axes of the intensity ellipse is sufficient to study how well do the simulated and measured results agree. However, we can do yet another step and compare the images illustrating intensity distributions at different points along the propagation. Such pictures are taken by the CCD camera and a subset of those pictures have already been shown in Figure 6.7. In order to produce their simulated analogs we can compute intensity in every point using equation (5.9) and produce a heat map. The resulting simulated ellipses are illustrated in Figure 6.8. Comparing them to the measured ellipses from Figure 6.7, one can see that both sets of intensity distributions are very similar. The largest deviations in values of intensity ellipse angle occur in the region where the intensity distribution is nearly circular and thus CCD camera is expected to produce larger errors in defining this angle.

6.3.8. Conclusion

The first set of comparisons with the manually defined lens configuration has shown promising results. Overall we achieved a good agreement between the simulation and measurement results. However, with this setup we did not have a chance to see a clear rotation of the intensity ellipse as general astigmatic beam propagates in free space. Thus, in the next set of measurements our goal is to build a lens configuration

that produces a general astigmatic beam with the clearly observable rotation of the intensity ellipse.

6.4. Optimal setup search

In the previous section it was shown that with some general astigmatic Gaussian beams it is not easy to study all their properties. In particular, we could not observe the clear rotation of the intensity ellipse. This problem was not caused by the measurement accuracy or any other technical problems. It came from the properties of the beam itself. Major part of the rotation of its ellipse happened within a small distance, corresponding to the region, where the intensity profile was nearly circular. This observation leads to the conclusion that not all general astigmatic beams are equally well-suited to study their properties. The parameters of the resulting general astigmatic beam are conditioned by the setup the beam propagated through. Thus, not all the setups that produce general astigmatic Gaussian beams are equally good to investigate the behavior of such beams.

In this section I will suggest the criteria of a setup that is optimal in a sense that it produces the general astigmatic beam that is the most convenient for a study of beam characteristics from all possible setups. To find the optimal setup I developed an algorithm and implemented it in the simulation. The resulting optimal setup will be described in the end of this section.

6.4.1. Criteria of optimal setup

As discussed above we consider the lens configuration to be optimal if it produces the general astigmatic beam with the most clearly recognizable rotation of the intensity ellipse behind the second lens. In this section I am going to transform this relatively vague condition into concrete criteria of optimality.

In Chapter 5 it was proven that the intensity ellipse angle of the general astigmatic beam changes by a total of π as beam propagates from $-\infty$ to $+\infty$. It is obvious that the measurements cannot be performed over infinite distance. Thus, in order to see a clear rotation we need to have a significant fraction of a total angle change within a region, where measurements are performed. Assume that the first measurement point is located at distance z^1 behind the second lens and the orientation of the intensity ellipse at this point is φ_w^1 , the last – at a distance z^n with the intensity ellipse angle of φ_w^n . Then we would like to maximize the total change of the intensity ellipse orientation $\Delta\varphi_w = |\varphi_w^n - \varphi_w^1|$.

Even if the observed change of the intensity ellipse angle in the measurement region contains a significant fraction of the total change of π radians, it does not guarantee the observation of clear rotation. It can happen that most of the observed change happens between two consequent measurement points and in other measurement points the curve is nearly flat. To avoid this in the optimal setup we need to minimize the maximum slope of the evolution of the intensity ellipse orientation $\max_i \partial\varphi_w^i / \partial z$. Together with the first criterion it will allow to choose the setup that produces the

intensity ellipse that rotates as slow as possible to reach the big change of the intensity ellipse orientation. In other words, we want to reach moderate speed of rotation that allows observations of the intensity ellipse at different stages of its evolution. In the first criterion we postulated that we want the overall measured angle change to be as big as possible. In the second criterion we added that we don't want all this change to happen within a single measurement point, but rather to spread it over the entire measurement region.

The higher the **ellipticity** $w_{\text{major}}/w_{\text{minor}}$ (or **flattening** $F = 1 - w_{\text{minor}}/w_{\text{major}}$) of the intensity ellipse at every measurement point, the easier to see the ellipse orientation and thus rotation of the light spot. If the measurements were performed at distances $z^i, i = 1, \dots, n$ behind the second lens and the flattening at each point was $F^i, i = 1, \dots, n$, than we would like to maximize the minimum flattening $\min_i F^i$.

The last criterion is induced by the CCD-camera and was already mentioned above. It implies that at each measurement point the beam should not become too large for the camera to capture. Both principal beam radii should not exceed 1.25 mm. We did not impose the lower limit on the beam size since within the investigations described in this chapter we never had an issue with a beam that is too small. However, it should be kept in mind that beam diameter should not become smaller than 65 μm .

These four criteria were implemented in the simulation for the search of the optimal setup among the variety of two lens configurations that we could build using three available lenses. The algorithm used in this simulation is described in appendix B.

6.4.2. Optimal lens configuration

The simulation for the optimal setup search (appendix B) has found the optimal configuration of the two cylindrical lenses described in table 6.10. Lens positions are given with respect to the beam waist, the transversal angle α is zero when the axis of symmetry of the cylindrical lens, corresponding to the zero curvature, is oriented horizontally.

Table 6.10.: The parameters of optimal lens configuration, found by the simulation for the optimal setup search.

Name	Orientation (a)	z [mm]	α [degree]
Lens3	biconvex (0)	10	0
Lens2	plano-convex (1)	216.5	25

The performance of this setup according to criteria discussed above can be described as:

1. the total change of the intensity ellipse orientation over the measurement region of 25 cm behind the second lens is $|\Delta\varphi_w| = 101.88^\circ$ or about 0.6 of the total rotation of 180° ;
2. the maximum slope of the evolution of the intensity ellipse angle is $|\partial\varphi_w/\partial z|_{\text{max}} = 0.77^\circ/\text{mm}$, which means that the rotation is really slow and

smooth within the measurement region;

3. the minimum flattening over the measurement region of 25 cm behind the second lens is $F_{\min} = 0.46$, which means that at every point along the beam propagation in this region the major principal semi-axis of the intensity ellipse is at least 1.85 times larger than the minor principal semi-axis;
4. the beam does not exceed the radius of 1.25 mm within a measurement region.

The evolution of the intensity ellipse is illustrated in Figure 6.12. Black lines corresponds to the intensity ellipse orientation, blue and red curves represent major and minor semi-axes of the beam spot. It is easy to see that the evolution of the light spot angle is smooth and result in a big angle change over the measurement region. The principal semi-axes never become close to each other and thus the intensity profile remains elliptical at every point.

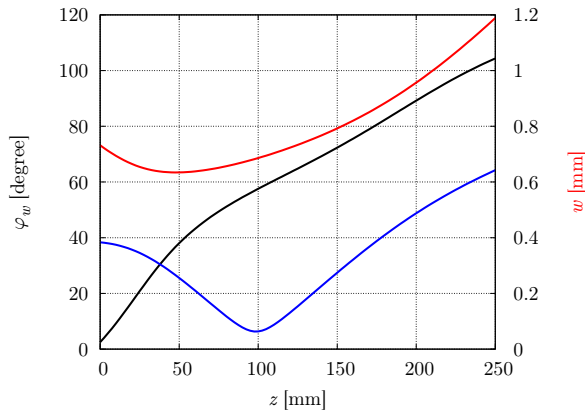


Figure 6.12.: The performance of the optimal lens configuration found by the simulation for the optimal setup search. Evolution of the intensity ellipse angle (in black) and semi-major (in red) and semi-minor (in blue) axes.

This optimal setup meets all the requirements. It should be mentioned, however, that depending on the search parameters such as the weighting of the different criteria the optimal setup can change. It might also be different if the initial simple astigmatic beam is replaced by a different one. For our concrete specifications this setup is optimal and we used it in the further investigations of general astigmatic Gaussian beams.

6.5. Measurements with the nearly optimal setup

In this section I will show the results of the measurements with the setup that is close to the optimal lens configuration described in the previous section. It will provide the new sets of observations and comparison between measured and simulated results.

The initial simple astigmatic beam did not change in comparison to the previous sets of measurements. Thus I will not discuss it in this section. I will start right away with the parameters of the new setup and continue with the measurement results and corresponding simulation results.

6.5.1. Nearly optimal lens configuration

Due to technical reasons the setup that was built in the lab is slightly different setup from the one found in the optimal setup search. Almost all parameters of the lens configuration are identical to the ones give in Table 6.10. The only parameter who's value has changed is the transversal angle of the second lens α_2 since the angle required in the optical setup was not achievable with the available mounts. Its value was 19° in the experiment instead of 25° in the optimal setup. Such setup still has a good performance and the rotation of its intensity ellipse is still clearly observable. For this nearly optimal lens configuration

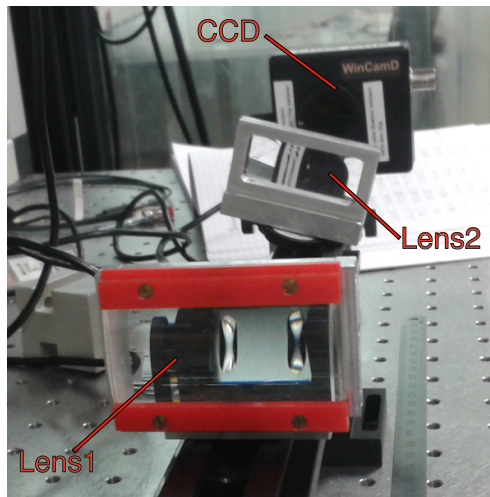


Figure 6.13.: Lab photograph of the nearly optimal setup.

1. the total change of the intensity ellipse orientation over the measurement region of 25 cm behind the second lens is $|\Delta\varphi_w| = 116.07^\circ$ or about 0.64 of the total rotation of 180° ;
2. the maximum slope of the evolution of the intensity ellipse angle is $|\partial\varphi_w/\partial z|_{\max} = 0.9^\circ/\text{mm}$;
3. the minimum flattening over the measurement region of 25 cm behind the second lens is $F_{\min} = 0.41$, which means that at every point along the beam propagation in this region the major principal semi-axis of the intensity ellipse is at least 1.7 times larger than the minor principal semi-axis;

4. the beam does not exceed the radius of 1.25 mm within a measurement region.

Overall for this setup only the slope of the intensity ellipse angle evolution is slightly bigger and the minimum flattening is slightly higher than for the optimal setup. On the other hand, the total angle change increases by about 15° . All together it makes this setup comparable with the optimal setup. The photograph of this nearly optimal setup is shown in Figure 6.13.

6.5.2. Measurement results

With the setup described above two sets of measurements were performed. As before, the snapshots of the intensity profile were taken with the CCD camera at different distances behind the second lens. The angle of the intensity ellipse was extracted from these pictures by the CCD camera software. The subset of the images from the CCD camera is presented in Figure 6.14. As expected, the rotation of the intensity ellipse is clearly observable. The light spot never degenerates to circle, the rotation is significant, slow and thus captured at different stages.

6.5.3. Fit of the intensity ellipse angle evolution

For each of the two sets of measurements the fit has been performed in the same way as for measurements with the manually defined setup. Figure 6.16 illustrates the results of the comparison between the measured and simulated intensity ellipse orientations for both sets of measurements. As for the measurements with the manually defined setup, black pluses show the measurement points, red curve is the nominal simulated curve and blue curve is the fitted simulated curve. The graphs show that even with the measured initial parameters simulation agrees with the experiment. After the parameters are fitted the agreement improves. For the second set of measurements fitted simulated curve almost exactly follows the measurement points.

The results of the comparison are summarized in Table 6.11. The fit performance is again characterized by the value of $\Delta_{\text{fitted}}^\varphi$. In both cases it shows significant improvement in comparison to the value of $\Delta_{\text{nominal}}^\varphi$. However, for the first measurement the average distance between the measured and simulated intensity ellipse angles is about 6° , which is a significant deviation that can hardly be explained by inaccuracy of the measurement points. This is not true for the second measurement, where this value is less than 2° .

6.5.4. Comparison of the intensity distributions

Additionally to comparison of measured and simulated evolutions of intensity ellipse orientations we can now compare measured and simulated intensity profiles in the same way as it was done in the section dedicated to the manually defined setup. The snapshots from the CCD camera are given in Figure 6.14. Corresponding simulated intensity distributions are given in Figure 6.15. These pictures show that the evolution of intensity profiles is very similar in both cases.

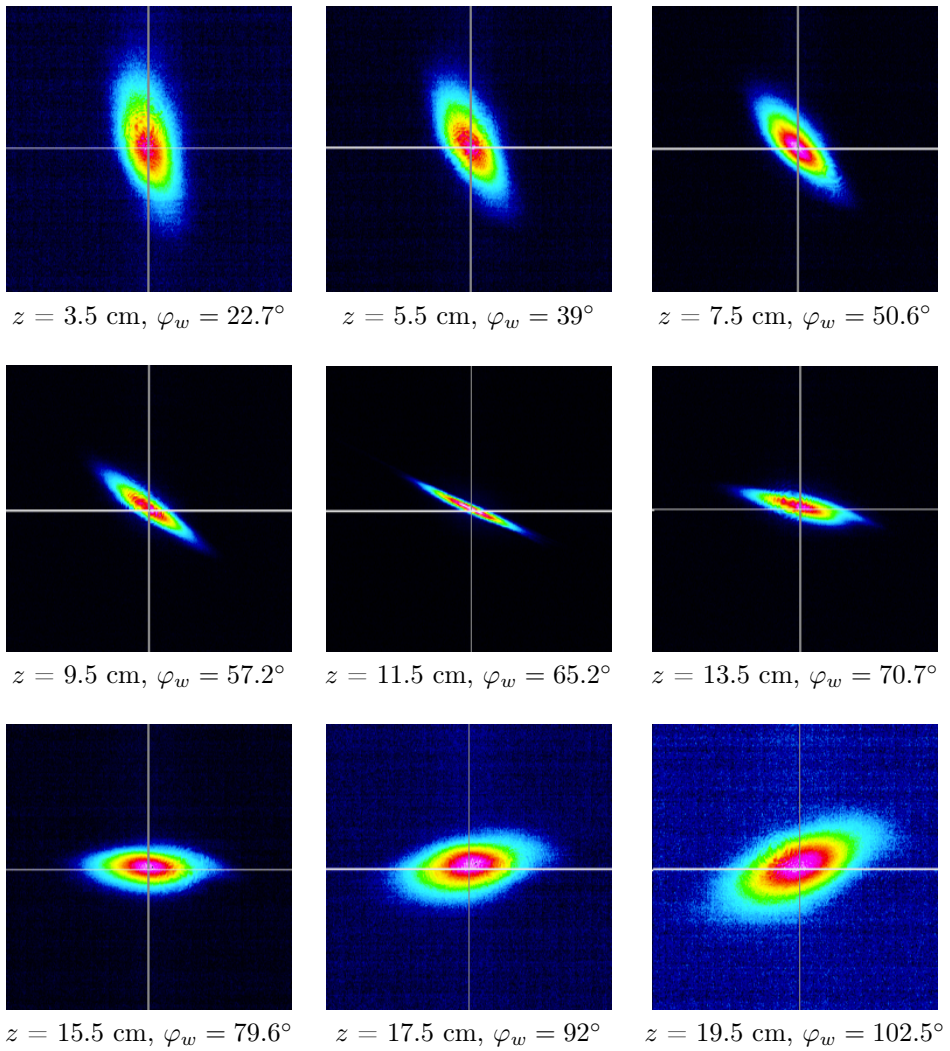


Figure 6.14.: The evolution of intensity ellipse of the general astigmatic beam produced by the nearly optimal setup. Snapshots from the CCD camera taken at different distances z behind the second cylindrical lens. The orientation φ_w of each intensity ellipse was defined by the CCD camera software.

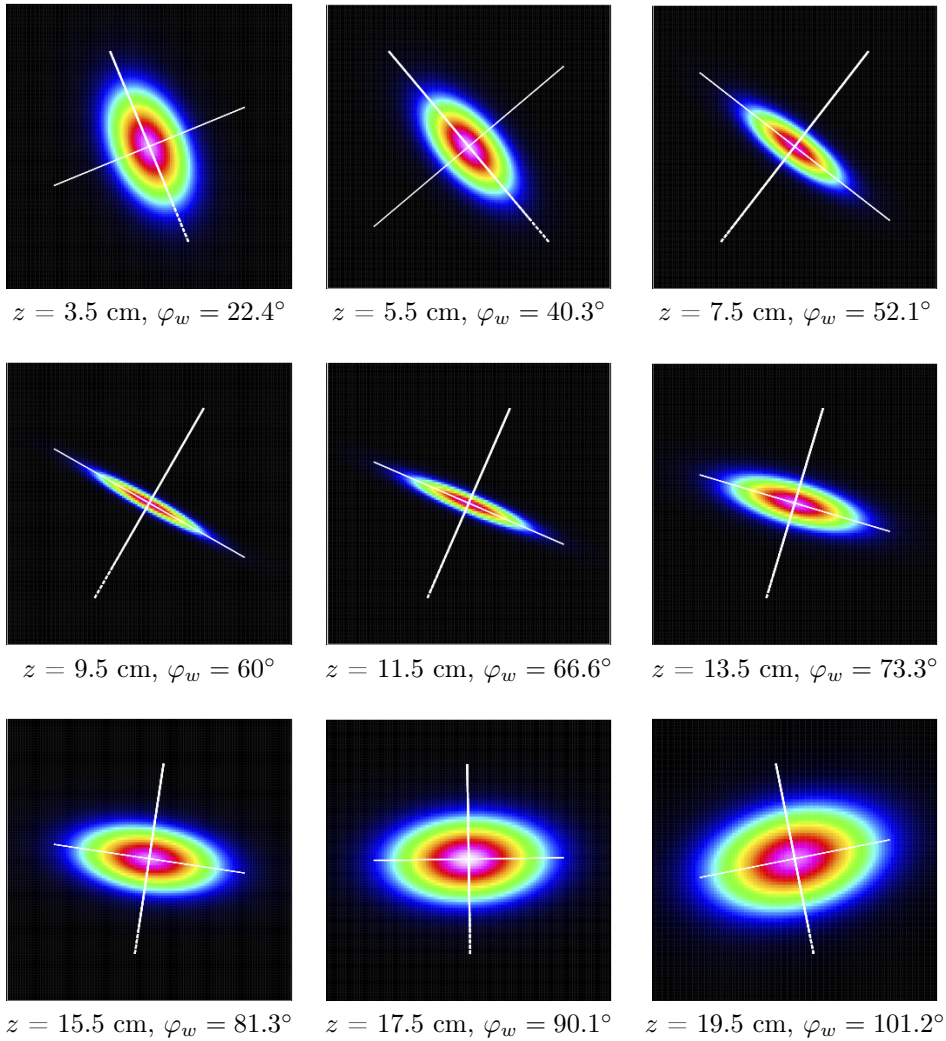


Figure 6.15.: The evolution of intensity ellipse of the general astigmatic beam produced by the nearly optimal setup. Snapshots from the simulation fitted to the first measurement. The value of z shows the distance behind the second cylindrical lens. The value φ_w is the angle of orientation of the intensity ellipse.

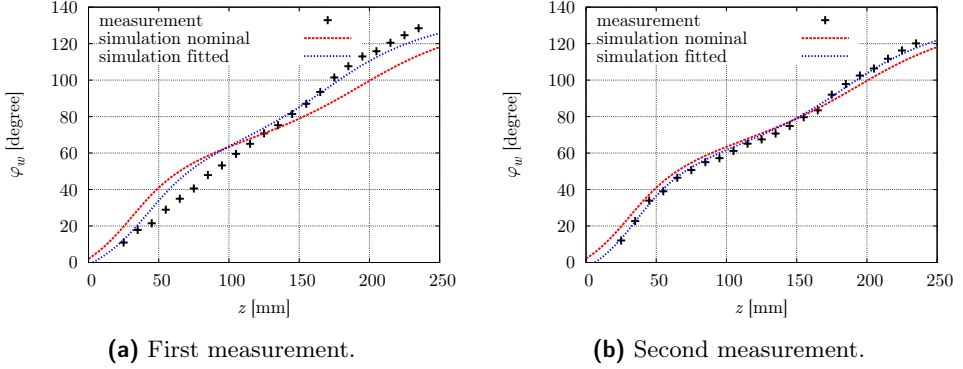


Figure 6.16.: Evolution of the intensity ellipse orientation as the beam propagates behind the second lens of the nearly optimal setup. Black plusses illustrate the measurement points, the red curve results from the simulation with the measured parameters of the setup, the blue curve results from the simulation with the fitted parameters of the setup.

Table 6.11.: Measured and fitted parameters of the nearly optimal setup. The deviation between the measurement and simulation is given by $\Delta_{\text{nominal}}^{\varphi}$. Similar deviation for the fitted parameters values is given by $\Delta_{\text{fitted}}^{\varphi}$.

Parameter	Units	Value	Tolerance	Fit 1	Fit 2
f_1	[mm]	53.5	± 3.5	49.9	50.1
f_2	[mm]	66.5	± 4.2	66.3	66.8
z_2	[mm]	216.5	± 1	217.5	217.5
α_2	[degree]	19	± 1	18	19.7
w_{01}	[μm]	295	± 12.2	307.4	307.5
w_{02}	[μm]	253	± 15.2	268.4	237.5
z_{01}	[mm]	0.82	± 10.2	11.05	-9.5
z_{02}	[mm]	1.01	± 12.3	13.34	13.3
φ_{w0}	[degree]	0	± 10	-10	-10
l	[mm]	7.2	± 1	6.2	6.2
β	[degree]	0	± 1	-1	-1
$\Delta_{\text{nominal}}^{\varphi}$	[degree]			11.56	4.5
$\Delta_{\text{fitted}}^{\varphi}$	[degree]			6.14	1.87

On the pictures taken by the CCD camera (Figure 6.14) some disturbances in intensity distributions are visible (see for example snapshot at $z = 13.5$ cm). This effect is also visible in the snapshots from the measurements with the manually defined setup (Figure 6.7). It can be explained by the imperfection of the initial simple astigmatic Gaussian beam (see Figure 6.4). It is not unlikely that this deviation of the initial beam from the Gaussian beam profile can couple into the values of the intensity ellipse angle and semi-axes.

6.5.5. Conclusion

In this section we performed two sets of measurements with the nearly optimal setup. Thus we could clearly see the intensity ellipse rotation as general astigmatic Gaussian beam propagates in free space. The comparison between the measured and simulated evolutions of the intensity ellipse orientation has shown good agreement. However, this agreement can possibly be further improved by using different initial simple astigmatic (or circular) beam. From Figure 6.4 it is obvious that the initial beam does not have a clear Gaussian profile. Even with the naked eye it is visible that it is hard to determine the orientation of this beam. Thus it is not surprising that different measurements with the CCD camera have shown different values of φ_{w0} . Therefore, in the next step we will improve the quality of the initial beam.

6.6. Measurements with improved initial beams

In this section I will present the results of comparison of two sets of measurements with the corresponding simulations. Each set of measurements was performed with a different initial beam and slightly different lens configuration. In both cases the initial beams had much clearer Gaussian profile than the beam that was used in previous sets of measurements. Thus within this investigation we could achieve a good agreement not only for orientation of the intensity ellipse, but also for its semi-axes.

I will start with the characterization of both improved initial beams. Then I will describe the lens configurations. Both of them are the variations of the nearly optimal setup studied in the previous section. It is not unlikely that for new beams optimal setup search would suggest different optimal lens configuration. However, with the new beams nearly optimal setup produced general astigmatic beam with the clearly observable rotation of the intensity ellipse. After describing the setup I will present the results of fits for both cases.

6.6.1. Characterization of the improved initial beams

The characterization of both improved initial beams has been performed following the same procedure as the characterization of the previously used initial beam. Even though they were fitted into simple astigmatic model, both beams are nearly circular in reality. Thus, we assumed that the angle of orientation of the initial beam can have any value in the range of $\pm 90^\circ$. The tolerances of other beam parameters were computed in the same way as before.

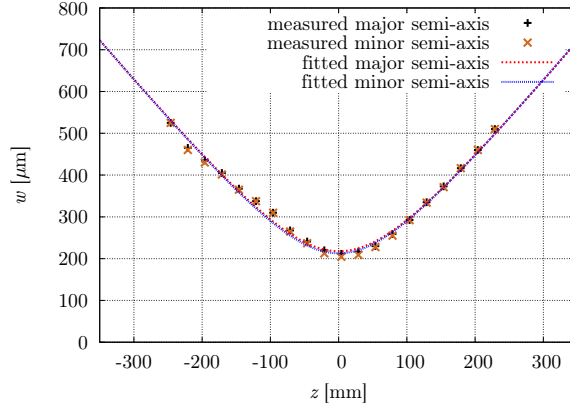


Figure 6.17.: Characterization of the first improved initial beam. Gaussian curve is fitted to the measured beam radii separately for two principal semi-axes of the simple astigmatic beam.

The evolution of the principal semi-axes of the first improved initial beam is shown in Figure 6.17. Black pluses and brown crosses represent the measurement points, red and blue curves are the corresponding fitted curves. Found beam parameters are given in Table 6.12.

Table 6.12.: The list of parameters of the first improved initial beam.

Parameter	Units	Value	Standard error	Confidence interval
z_{01}	[mm]	0.68	± 1.7	± 5
z_{02}	[mm]	0.21	± 2	± 5.7
w_{01}	[μm]	218	± 4.2	± 12.2
w_{02}	[μm]	213	± 5	± 14
M_1	[1]	1.12	± 0.008	± 0.025
M_2	[1]	1.11	± 0.01	± 0.03

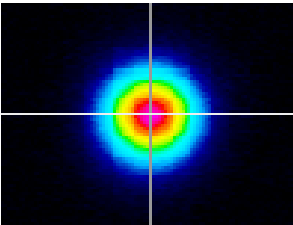


Figure 6.18.: Intensity profile of the improved beam at a position close to the waist.

Similarly the results for the second improved initial beam are given in Figure 6.17 and Table 6.12.

Even though the determined M^2 factors for both improved beams are significantly bigger than they were in the previous case, we could achieve a very good agreement between simulation and experiment without taking them into account. As before, they were not implemented in the simulation and thus neglected in a comparison.

Both beams have a clear Gaussian shape with no disturbances. The intensity profile of the second improved initial beam near the waist position is shown

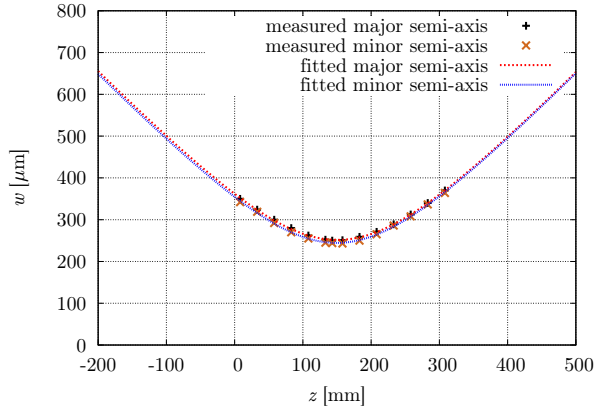


Figure 6.19.: Characterization of the second improved initial beam. Gaussian curve is fitted to the measured beam radii separately for two principal semi-axes of the simple astigmatic beam.

Table 6.13.: The list of parameters of second improved initial beam.

Parameter	Units	Value	Standard error	Confidence interval
z_{01}	[mm]	151	± 0.5	± 1.44
z_{02}	[mm]	149.5	± 0.6	± 2
w_{01}	[μm]	252	± 0.6	± 2
w_{02}	[μm]	244.5	± 0.8	± 2.75
M_1	[1]	1.13	± 0.002	± 0.007
M_2	[1]	1.11	± 0.003	± 0.01

in Figure 6.18. The intensity profile of the first improved beam looks similar.

6.6.2. Lens configuration

The lens configuration did not change much in comparison to the nearly optimal lens configuration used in the previous section. As it will be shown later, from the new initial beams it also produced clearly observable rotating intensity ellipses with a moderate speed of rotation, significant ellipticity and without violating spot size requirement. The exact parameters of the lens configuration used in both sets of measurements can be found in Table 6.14.

Table 6.14.: The parameters of nearly optimal lens configurations that were used in the measurements with the improved beams. ¹ – measurement with the first improved beam, ² – measurement with the second improved beam

Name	Orientation (a)	z [mm]	α [degree]
Lens3	biconvex (0)	10	0
Lens2 ¹	plano-convex (1)	208	17
Lens2 ²	plano-convex (1)	213	17

6.6.3. Fit of the intensity ellipse evolution

The sets of measurements with both improved beams have been performed with the updated CCD camera software and without filters. Thus it was possible to fit the evolution of principal semi-axes of the intensity ellipse together with the evolution of the intensity ellipse orientation. The evolution of the intensity ellipse is illustrated in Figure 6.20. The simulated evolution of both orientation and semi-axes of the intensity ellipse agrees to the experimental results even when the measured parameters are used. Fitted curves follow the measurement points even closer. These graphs also show that nearly optimal lens configuration has good performance with the new initial beam: the total change of the intensity ellipse orientation is big and the speed is moderate, the major semi-axis is always significantly bigger than the minor semi-axis, but does not exceed the limit induced by the CCD camera.

Table 6.15 contains both measured and fitted parameters of the measurement with the nearly optimal lens configuration and the first improved initial beam. The fit performance can still be evaluated by comparing the values Δ_{nominal} and Δ_{fitted} . These values are now the normalized sums of the average differences between measured and simulated values of both intensity ellipse semi-axes and orientation:

$$\Delta_{\text{nominal}} = \Delta_{\text{nominal}}^{\varphi} + \omega_{w1} \Delta_{\text{nominal}}^{w1} + \omega_{w1} \Delta_{\text{nominal}}^{w2}, \quad (6.12)$$

$$\Delta_{\text{fitted}} = \Delta_{\text{fitted}}^{\varphi} + \omega_{w1} \Delta_{\text{fitted}}^{w1} + \omega_{w1} \Delta_{\text{fitted}}^{w2}, \quad (6.13)$$

where the average value of the absolute difference between the measured and simulated angles of the intensity ellipse is given by equations (6.10) and (6.11). Similarly

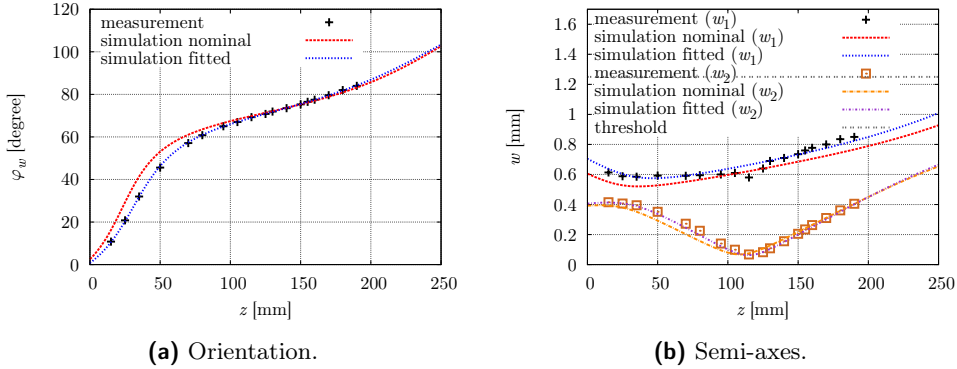


Figure 6.20.: Intensity ellipse evolution as beam propagates behind the second lens of the nearly optimal setup. The initial beam is the first improved nearly circular beam.

the average absolute difference between measured and simulated intensity ellipse semi-axes is defined as

$$\Delta_{\text{nominal}}^{wj} = \left[\sum_{i=1}^n (w_j^m - w_j^n)^2 / n \right]^{1/2}, \quad (6.14)$$

$$\Delta_{\text{fitted}}^{wj} = \left[\sum_{i=1}^n (w_j^m - w_j^f)^2 / n \right]^{1/2}, \quad j = 1, 2. \quad (6.15)$$

The weights ω_1 and ω_2 are given by

$$\omega_j = \Delta_{\text{nominal}}^\varphi / \Delta_{\text{nominal}}^{wi}, \quad j = 1, 2. \quad (6.16)$$

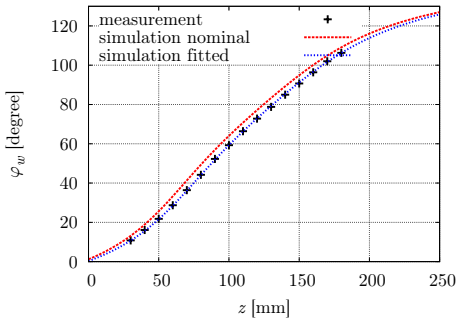
Similarly the results for the measurement with the second improved beam are presented in Figure 6.20 and Table 6.16. In this case, unlike in all previous measurements, the waist of the initial beam is not located before the first cylindrical lens. Still the performance of nearly optimal lens configuration is very good and the rotation is clearly observable. The simulated curve is fitted very closely to the measurement points.

6.6.4. Comparison of intensity distributions

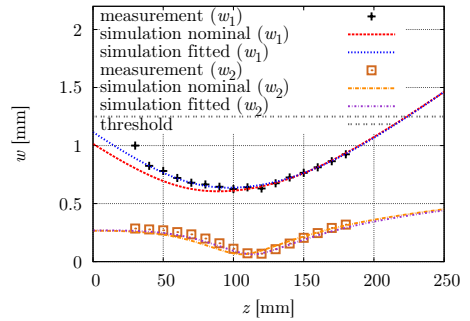
Within these sets of measurements we did not produce large sets of intensity profiles to compare. However, to illustrate that the measured and simulated light spots in this case are even more similar to each other, in Figure 6.22 several intensity ellipse snapshots from the CCD camera and from the simulation are provided.

Table 6.15.: Measured and fitted parameters for the measurement with the first improved initial beam.

Parameter	Units	Value	Tolerance	Fit
f_1	[mm]	53.5	± 3.5	49.9
f_2	[mm]	66.5	± 4.2	68.2
z_2	[mm]	208	± 1	209
α_2	[degree]	17	± 1	16.6
w_{01}	[μm]	218	± 12.2	207.17
w_{02}	[μm]	213	± 14	227.3
z_{01}	[mm]	0.68	± 5	-2.5
z_{02}	[mm]	0.21	± 5.7	5.98
φ_{w0}	[degree]	0	± 90	1.5
l	[mm]	7.2	± 1	6.2
β	[degree]	0	± 1	-0.6
Δ_{nominal}	[degree]			11.74
Δ_{fitted}	[degree]			3.8



(a) Orientation.

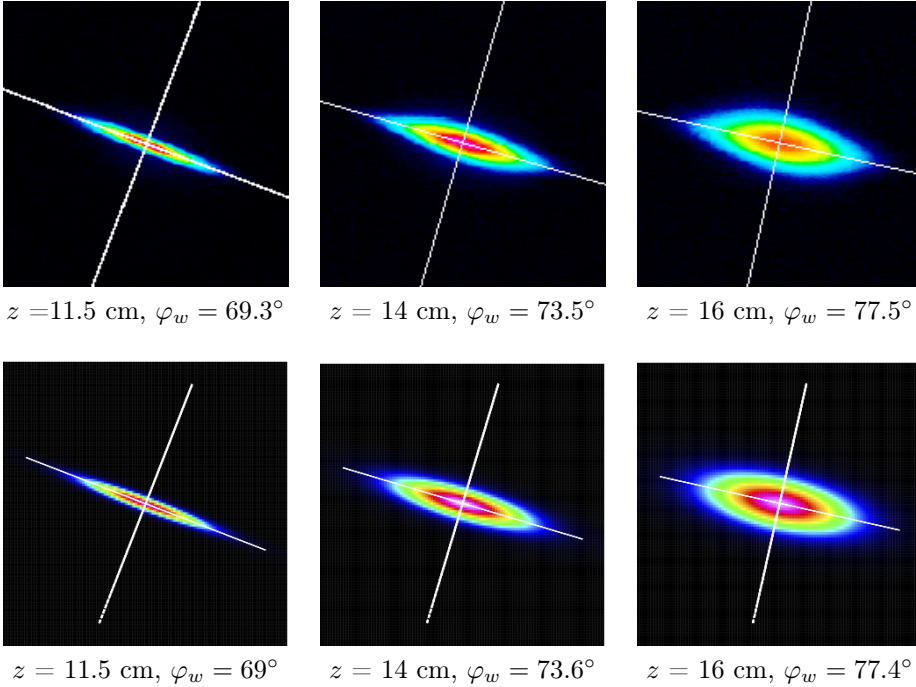


(b) Semi-axes.

Figure 6.21.: Intensity ellipse evolution as beam propagates behind the second lens of the nearly optimal setup. The initial beam is the second improved nearly circular beam.

Table 6.16.: Measured and fitted parameters for the measurement with the second improved initial beam.

Parameter	Units	Value	Tolerance	Fit
f_1	[mm]	53.5	± 3.5	50
f_2	[mm]	66.5	± 4.2	69
z_2	[mm]	213	± 1	214
α_2	[degree]	17	± 1	16.3
w_{01}	[μm]	252	± 2	254
w_{02}	[μm]	244.5	± 2.75	242.5
z_{01}	[mm]	151	± 1.44	149.56
z_{02}	[mm]	149.5	± 2	242.5
φ_{w0}	[degree]	0	± 90	1
l	[mm]	7.2	± 1	6.2
β	[degree]	0	± 1	-0.6
Δ_{nominal}	[degree]			12.25
Δ_{fitted}	[degree]			4.7

**Figure 6.22.:** The evolution of intensity ellipse of the general astigmatic beam produced from the first improved initial beam by the nearly optimal setup. Images from CCD camera (first row) and simulated images (second row).

6.7. Conclusion and outlook

In this chapter I presented the results of the experimental verification of the general astigmatic Gaussian beam model. We compared measured and simulated evolutions of the intensity ellipses in several different cases. By fitting the initial parameters of the setup within their measurement tolerances we achieved a very good agreement between the simulation and the experiment. Thus, we proved that the suggested general astigmatic Gaussian beam model is capable of representing the evolution of the general astigmatic Gaussian beam. Within the simulation I used the formula that transforms arbitrary Gaussian beams in fundamental mode via refraction on the second order surface (equation (5.65)). Therefore, the capability of the model to transform beams on surfaces was verified experimentally.

Since there was no Shack-Hartmann sensor available (see for example [35]), this study does not include any comparison of the evolution of the wavefront. It is planned, however, to investigate the evolution of the wavefront of the general astigmatic Gaussian beam in further experiments.

The implication of beam model choice on a pathlength readout

THREE models of the Gaussian beam in fundamental mode were discussed in Chapter 3, Chapter 4 and Chapter 5. The geometrical part of tracing beams through the optical systems is identical for all types of beams and was given in Chapter 2. The accumulated phase and accumulated optical pathlength are also computed in the same way in all three models. The main differences between the models are the beam description and beam transformation via reflection and refraction.

It was shown that the most general case of a Gaussian beam in fundamental mode is a general astigmatic Gaussian beam. With the general astigmatic model it is possible to simulate the transformation of a beam impinging at an oblique angle at an arbitrary second order surface. With the simple astigmatic model a beam can be transformed at an ellipsoidal surface if one of its principal axes and one of the principal axes of the surface lie in the plane of incidence. If these restrictions are not fulfilled the simple astigmatic beam model can only be used as an approximation. For the beam transformation within the stigmatic Gaussian beam model it is assumed that the beam incidence on a surface is close to normal and the angle of incidence is neglected when the q -parameter is transformed. Therefore, when using this model for the transformation of the beam impinging at an oblique angle on a surface, one should keep in mind that the angle of incidence will only be used in the geometrical part of the beam tracing.

In this chapter I will analyze the implications of the beam model choice on the main science signal, namely the longitudinal pathlength signal (see Chapter 2). In my investigation I will consider the cross-coupling of the angular beam jitter into the pathlength readout for the case, when before impinging on the photodiode both reference and measurement beams are traced through the imaging optics, consisting of two spherical lenses.

I will start with the explanation of the main principles of the imaging optics systems and the motivation to use them in a LISA-like mission (Section 7.1). Then I will present the approach to the design of such systems and suggest a set of exemplary two lens optical systems. In Section 7.3 I will discuss which types of Gaussian beams in fundamental mode and under which circumstances can appear in such systems. Then I will start the comparison of the cross-coupling of the beam angular jitter into the pathlength readout obtained with three different models. First I will present the results for the perfectly aligned optical systems. Then I will analyze the response of the longitudinal pathlength signal on the misalignment of the single lens. In the end I will compare the results for the realistically misaligned optical systems and conclude on the implication of the beam model choice.

7.1. Imaging optics

Optical simulations for LISA Pathfinder have shown that the expected test mass angular jitter, which results in angular jitter of the measurement beam, cross couples into the longitudinal pathlength signal [6, p. 93]. In a LISA-like mission the sensitivity requirements are more stringent and thus the suppression of the undesired cross-coupling is required. It was decided to design lens systems that image the test mass surface onto the photodiode [PD1]. Such systems have not been used before in precision interferometry for this purpose. Thus, they required extensive investigation.

Stigmatic and simple astigmatic beams can be transformed into general astigmatic beams by an imaging optics system. Therefore, the only beam model that can be used to trace tilted beams through the lens systems is the general astigmatic beam model. In this chapter I will study the impact of the use of simplified beam model in simulations of imaging optics systems.

In order to investigate the propagation of a Gaussian beam in fundamental mode through the imaging optics and study the implications of the beam model choice I will use two lens systems for the test mass interferometer. In this interferometer the reference and measurement beams are both Gaussian in fundamental mode with a waist radius of 1 mm. The requirements for the imaging optics systems evolve together with the design of the LISA Optical Bench (LISA OB). Thus, it is likely that the concrete specifications will change in the future. The requirements for the imaging optics systems that will be used within this chapter are taken from [PD2]. The primary design goal for the imaging optics system is to suppress the cross coupling of the test mass angular jitter into the longitudinal pathlength signal. For all test mass angles φ_{TM} in the range of $\pm 250 \mu\text{rad}$ the slope of the longitudinal pathlength signal $\partial(\text{LPS})/\partial\varphi_{\text{TM}}$ should not exceed $35.8 \text{ pm}/\mu\text{rad}$ [PD3].

The distance between the test mass and the first lens of the imaging system L_{in} is fixed and with the requirements considered here is equal to 426 mm (see Figure 7.1). This restriction comes from the fact that in order to balance transmission through fused silica substrates, the imaging optics systems should be placed behind the recombination beam splitter that interferes the static reference and the tilting measurement

beams. Another length constraint affects the distance between the second lens and photodiode L_{out} . This distance cannot be smaller than 16 mm to accommodate the photodiode and its mount [PD3]. Due to the size limits of the LISA OB the overall size of the imaging optics system ($L + L_{\text{out}}$) cannot exceed 120 mm.

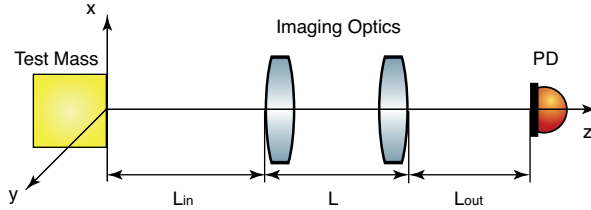


Figure 7.1.: The simplified not to scale schematic of the imaging optics system as it is implemented in the simulation. Both the reference and the measurement beams have their origins at the test mass surface. The reference beam is static, the measurement beam is tilting.

The imaging optics system should not introduce considerable magnification. Within the current requirements we aim for a 1:1 imaging in the test mass interferometer. The preferable lens material is fused silica [PD3].

Table 7.1.: The requirements for the imaging optics systems for the test mass interferometer.

Parameter	Requirement
$\partial(\text{LPS})/\partial\varphi_{\text{TM}}$	$< 35.8 \text{ pm}/\mu\text{rad}$ for every φ_{TM} in range of $\pm 250 \mu\text{rad}$
L_{in}	$= 426 \text{ mm}$
L_{out}	$> 16 \text{ mm}$
$L + L_{\text{out}}$	$< 120 \text{ mm}$
magnification	1:1
material	fused silica
PD diameter	5.33 mm
QPD slit width	70 μm
waist position	on the test mass
waist radius	1 mm

The currently chosen photodiode is the quadrant photodiode with the 5.33 mm diameter and 70 μm slit. Within this chapter I will show the results for this photodiode and for a single element photodiode with the same diameter.

It is desired to use as few lenses as possible in the imaging optics systems to minimize stray light within the laser mode. Within this chapter I will only consider the systems that include only two spherical lenses. However, it is possible to design imaging optics with more lenses. Also the lenses can be aspherical. Analysis of such systems is out of the scope of the current study.

The requirements for the imaging optics for the test mass interferometer that were used within this chapter are summarized in Table 7.1. However, this investigation does not aim to evaluate the overall performance of each imaging optics system and suggest the solution that can be used in the LISA OB. Rather, it will show the impact of the use of the simplified beam model, which will be quite general for all similar lens systems.

7.2. Designs of the imaging optics systems

When the reference and measurement beams have identical wavefront curvatures on the photodiode their relative tilt does not couple into the pathlength readout in case if they are both centered on a perfect photodiode that detects both beams without any clipping. In the test mass interferometer reference and measurement beams do have nominally equal waist sizes and similar beam paths. Thus, if they are both centered on the photodiode they should have similar wavefront curvatures. This fact gives a possibility to use a purely geometrical approach to design the imaging optics systems for the test mass interferometer. If we find a lens system system that minimizes the beam walk on the photodiode, it will also minimize the cross coupling of the angular beam jitter into the pathlength signal.

In order to find suitable imaging systems a dedicated simulation was used. The goal of this simulation was to find a lens system, which would transform the measurement beam, tilted by $100\ \mu\text{rad}$ with respect to the reference beam, into a beam, impinging at the same angle (magnification 1:1) on the center of the photodiode. The test angle of the measurement beam could have been chosen differently. The value of $100\ \mu\text{rad}$ lies within a range of interest and seems to lead to the systems with a good performance.

In the search we used the fused silica lenses available from Qioptiq (former Linos) [36]. This catalog does not include fused silica lenses with focal lengths smaller than 6.14 mm. One additional fused silica lens with the small focal length of -4.5 mm was taken from the catalog of Sill Optics [37]. Each plano-convex and plano-concave lens was considered twice, depending on its orientation towards the incoming beam (similarly to cylindrical lenses in the optimal setup search in Chapter 6).

For each pair of lenses the distance L between them and the distance L_{out} between the second lens and the photodiode were varied until the measurement beam hit the center of the photodiode at the angle of $100\ \mu\text{rad}$. If for some particular lens pair it is impossible to find such values of L and L_{out} within the length constraints given in Table 7.1, the simulation continued the search with the new lens pair.

I performed the search of the imaging optics systems using the dedicated simulation described above. With the current requirements given in Table 7.1 I could find ten candidates shown in Figure 7.2. Their parameters are listed in Table 7.2. The lens names starting with capital G denote the lenses from Qioptiq. The lens S6LDK4120 is taken from Sill Optics. The specifications of lenses can be found in the corresponding lens catalogues.

The approach to the imaging optics design suggested above does not include the beam parameters and the photodiode shape. The imaging optics systems found with

Table 7.2.: The parameters of the imaging optics systems for the test mass interferometer.

Name	Lens 1	Lens 2	z_1 [mm]	z_2 [mm]	z_{PD} [mm]
TMIO-M1-EP426-01	G312257000	S6LDK4120	426	448.360	523.584
TMIO-M1-EP426-02	G312257000	S6LDK4120	426	445.954	520.716
TMIO-M1-EP426-03	G312258000	S6LDK4120	426	454.430	514.919
TMIO-M1-EP426-04	G312258000	S6LDK4120	426	452.373	512.529
TMIO-M1-EP426-05	G312259000	S6LDK4120	426	463.465	511.111
TMIO-M1-EP426-06	G312259000	S6LDK4120	426	460.457	507.706
TMIO-M1-EP426-07	G312301000	S6LDK4120	426	505.601	528.982
TMIO-M1-EP426-08	G311206000	S6LDK4120	426	449.331	524.003
TMIO-M1-EP426-09	G311026000	S6LDK4120	426	456.376	515.943
TMIO-M1-EP426-10	G311207000	S6LDK4120	426	461.541	511.030

the simulation described above guarantee minimum beam walk of the measurement beam on the photodiode. However, they do not guarantee the satisfaction of the primary design goal ($\partial(\text{LPS})/\partial\varphi_{\text{TM}} < 35.8 \text{ pm}/\mu\text{rad}$). The search does not take into account the values of the longitudinal pathlength signal (LPS). Since within this study I aim to investigate the impact of the beam model choice on the longitudinal pathlength signal, I will not consider the performance of the found imaging optics systems with respect to the main science goal. Instead I will compare the pathlength signals for the found lens systems obtained with each of the three beam models. Using only one setup in such a comparison would not allow to draw general conclusions, since a particular setup can have specific features that might affect the results. Thus, I will use all ten setups given in Table 7.1 in the comparison to provide the sustainability of the obtained results.

7.3. Analysis of pathlength readout

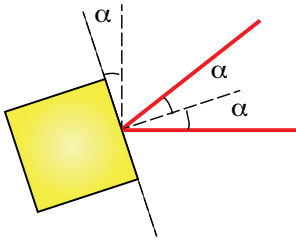
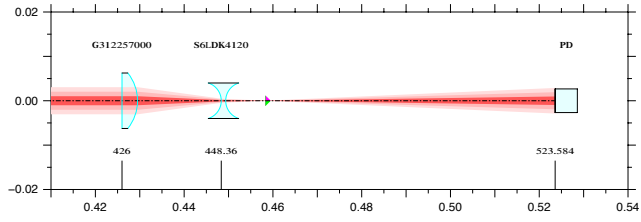


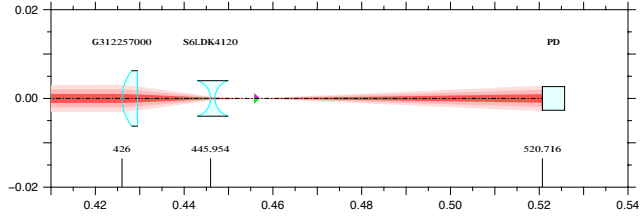
Figure 7.3.: The tilt of the test mass by an angle α results in the tilt of the measurement beam by an angle 2α .

Within this section I will investigate the cross coupling of the test mass angular jitter into the longitudinal pathlength signals both for quadrant and single element photodiodes. The test mass angular jitter in the range of $\pm 250 \mu\text{rad}$ results in the angular jitter of the measurement beam in the range of $\pm 500 \mu\text{rad}$ (see Figure 7.3). The reference beam is not reflected from the test mass and thus stays unaffected. To estimate the cross coupling of test mass angular jitter into the main science signal for each particular imaging optics system I will vary the test mass angle (and thus the angle of the measurement beam) in equidistant steps in the range of $\pm 250 \mu\text{rad}$. On each step

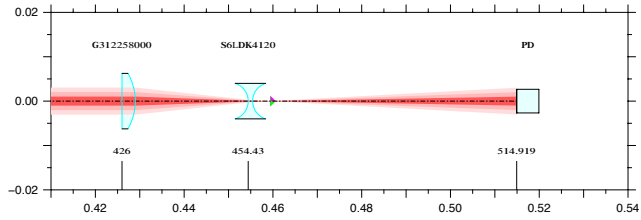
I will compute the LPS of a QPD and of a SEPD as described in Chapter 2. Therefore, I will obtain the curve $\text{LPS}(\varphi_{\text{TM}})$ for both types



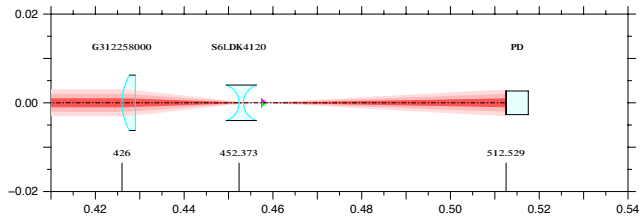
(a) TMIO-M1-EP426-01



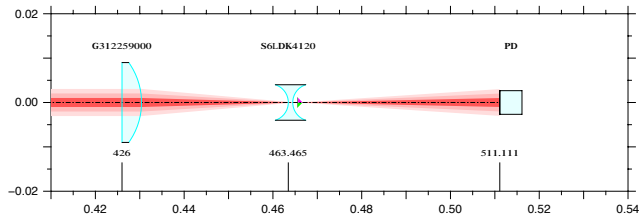
(b) TMIO-M1-EP426-02



(c) TMIO-M1-EP426-03



(d) TMIO-M1-EP426-04



(e) TMIO-M1-EP426-05

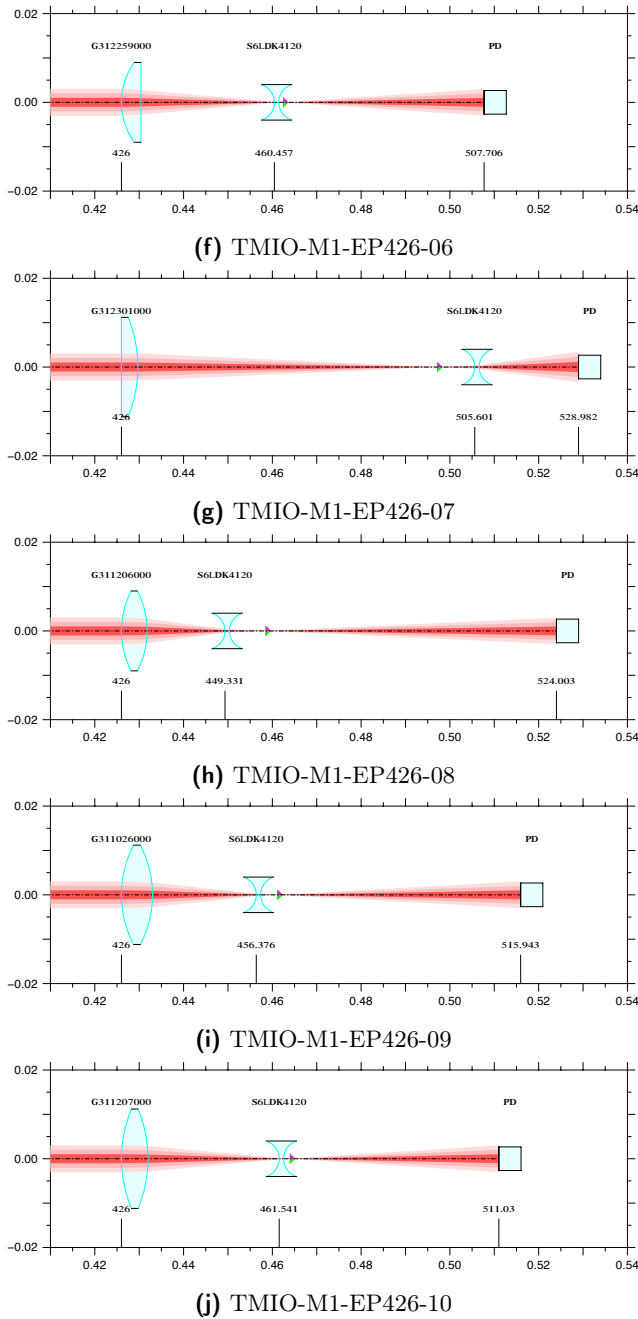


Figure 7.2.: The imaging optics systems for the test mass interferometer. The horizontal axis corresponds to the distance from the test mass (in meters). The vertical axis shows the transversal sizes of the components of optical systems (in meters). For simplicity the photodiode is represented as the glass plate with the diameter 5.33 mm. The labels on the vertical lines show the distances from the test mass to the front surface of the corresponding component in mm.

of photodiodes. The primary design goal of the imaging optics systems involves the slope of this curve $\partial(\text{LPS})/\partial\varphi_{\text{TM}}$. Since within this study I am only interested in the differences between the $\text{LPS}(\varphi_{\text{TM}})$ and $\partial(\text{LPS})/\partial\varphi_{\text{TM}}$ curves for different beam models and not in the concrete values of the slope of the curve, the comparison will only include the LPS signals. The conclusion on the impact of the beam model on the slope of the curve follows directly from the similar conclusion on the $\text{LPS}(\varphi_{\text{TM}})$ curve.

7.3.1. Aligned imaging optics systems

Let me first consider the case when the reference and measurement beams are both stigmatic Gaussian beams in fundamental mode before they are transformed by the imaging optics. If the lens system is perfectly aligned the reference beam impinges at every lens surface at a normal angle and thus stays a stigmatic Gaussian beam after propagation through the lenses. The measurement beam even in the aligned lens system impinges at the primary surface of the first lens at an oblique angle. Therefore, according to equation (4.38) and equation (4.39) after the propagation through the first lens the measurement beam becomes simple astigmatic. The plane, in which the measurement beam rotates (XZ plane in Figure 7.1), is also the plane of incidence of the measurement beam on the primary surface of the first lens. One of the principal axes of the simple astigmatic measurement beam behind the first lens lies in this plane. When this simple astigmatic beam impinges on the perfectly aligned second lens of the imaging optics system the plane of incidence on the second lens coincides with the plane of incidence on the first lens (XZ plane). Therefore, one of the principal axes of the simple astigmatic beam still lies in the plane of incidence. It means that the optical system the beam propagates through is orthogonal and the resulting measurement beam impinging on the photodiode is simple astigmatic.

With all three beam models the geometrical part of the beam tracing is identical. In the stigmatic beam model the non-normal incidence of the measurement beam on a lens surface will be neglected in the transformation of the q -parameter. However, the accumulated optical pathlength and the accumulated phase of the measurement beam will differ from those values for the reference beam and thus there will be a cross coupling of the test mass angular jitter into the pathlength readout.

With the simple astigmatic Gaussian beam model the non-normal incidence of the measurement beam on the lens surface is taken into account in the transformation of the q -parameters. Therefore, it is expected that the result obtained with the stigmatic beam model will differ from the result obtained with the simple astigmatic beam model, and the result obtained with the simple astigmatic beam model is more accurate.

General astigmatic beams are not produced by the perfectly aligned lens system. Therefore, the results obtained with the general astigmatic beam model have to be identical to those with the simple astigmatic beam model.

The simulation results for the ten perfectly aligned imaging optics systems for the test mass interferometer are given in Figure 7.4. They agree with the theoretical expectations provided above. In all graphs for both QPD and SEPD the LPS obtained

with the circular beam model is clearly different to the LPS obtained with both simple astigmatic and general astigmatic beam models. Both astigmatic models show very good agreement. Tiny differences that are hardly observable on the graphs result from numerical errors that can appear due to the fact that the general astigmatic beam model involves complex computations in the transformation of the radius of curvature tensor. It is noticeable that for all aligned setups the difference between the LPS obtained with the stigmatic beam model is smaller than the LPS obtained with both astigmatic models by about a factor of ten. Thus, the results obtained with the stigmatic beam model are too optimistic and cannot be regarded as accurate estimates of the LPS for the perfectly aligned lens systems.

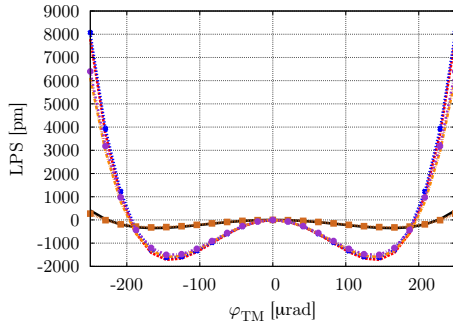
7.3.2. Transversal shift of the second lens

Perfectly aligned optical systems cannot be built in a real experiment. In order to predict realistic results with a simulation it is important to study the impact of possible misalignments. First I will introduce the single misalignment and discuss the theoretical expectations of its impact of the LPS. Then I will compare the theoretical expectations with the simulated results.

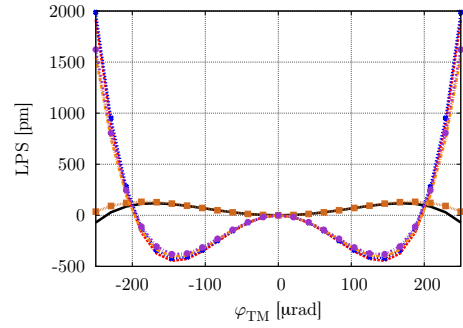
Within the comparison of the three beam models it is interesting to consider the optical systems that produce general astigmatic beams. In this case the results obtained with the simplified beam models (the circular and the simple astigmatic) are expected to differ from the results obtained with the general astigmatic beam. As it was shown above, a perfectly aligned optical system produces only simple astigmatic beams from initial stigmatic beams. In order to obtain an optical system that transforms a circular beam into a general astigmatic it is sufficient to introduce a single specific misalignment.

Let me consider the two lens optical system, where the first lens is perfectly aligned and the second lens is shifted from the optical axis orthogonally to the plane, where the measurement beam is rotated. For example, if the beam is tilted in XZ plane, I will consider the shift of the second lens along the Y axis. Behind the first lens, as before, the reference beam is stigmatic and the measurement beam is simple astigmatic. The plane of incidence of the measurement beam on the first lens is still the plane, where this beam is tilting (XZ plane). The reference beam impinges at a second lens at an oblique angle and thus is transformed into a simple astigmatic beam. For the measurement beam the plane of incidence on the second lens is not aligned with the plane of incidence on the first lens. When the second lens is shifted along the Y axis, the normal to the lens surface at the point of incidence does not lie in XZ plane. Thus, none of the principal axes of the beam ellipse lies in the plane of incidence on the second lens. Therefore, the measurement beam impinging on the photodiode in this case is a general astigmatic Gaussian beam.

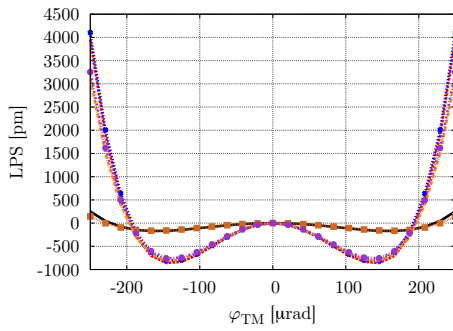
In the next step of the analysis I have shifted the second lens in all ten setups in 10 equidistant steps between $0\ \mu\text{m}$ and $10\ \mu\text{m}$ transversally to the plane of the measurement beam rotation. The measurement beam was tilted in XZ plane, the second lens was shifted along the Y axis. The results are shown in Figure 7.5 and Figure 7.6. The accumulated optical pathlength s_{ac} and the accumulated phase ϕ_{ac}



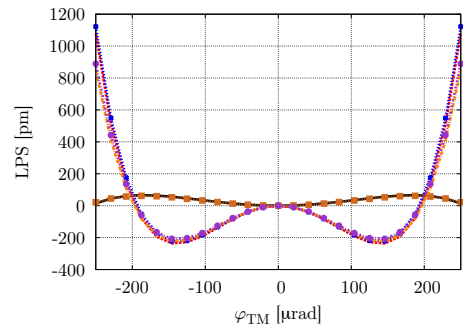
(a) TMIO-M1-EP426-01



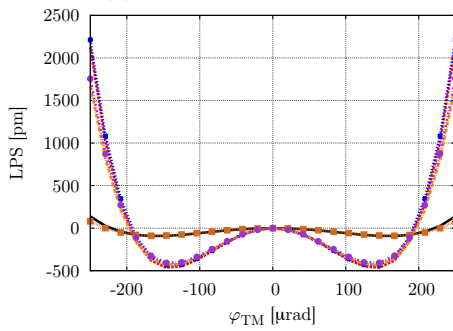
(b) TMIO-M1-EP426-02



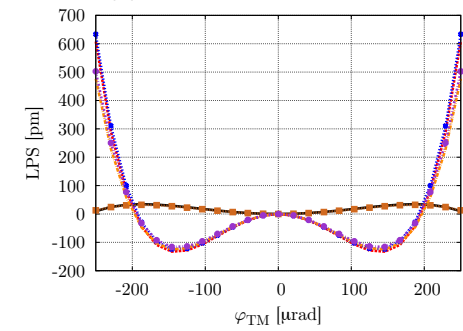
(c) TMIO-M1-EP426-03



(d) TMIO-M1-EP426-04



(e) TMIO-M1-EP426-05



(f) TMIO-M1-EP426-06

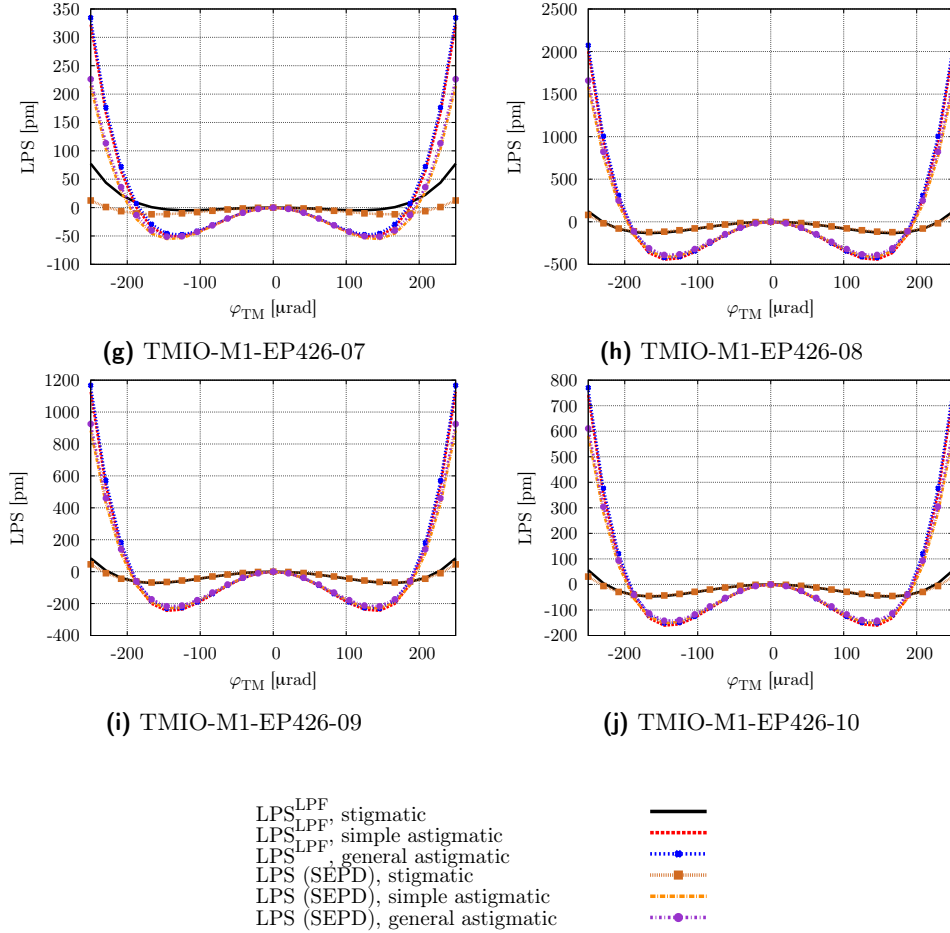
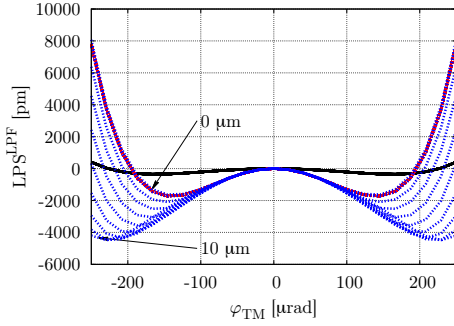
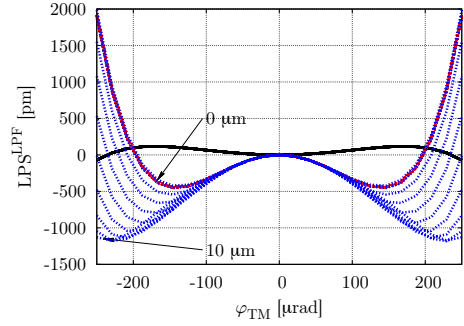


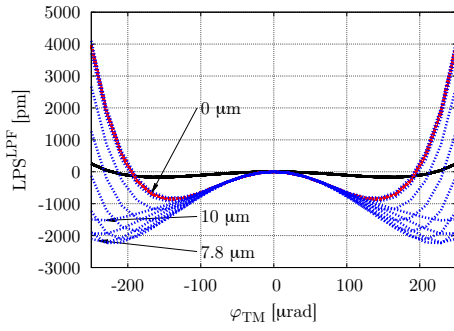
Figure 7.4.: The LPS for perfectly aligned imaging optics systems. The parameters of the lens systems are listed in Table 7.2. The parameters of the QPD are given in Table 7.1. The SEPD has the same diameter as the QPD. LPS^{LPF} is the pathlength signal on the QPD, LPS in the pathlength signal on SEPD. Angle φ_{TM} is the test mass angle or half the angle of the measurement beam.



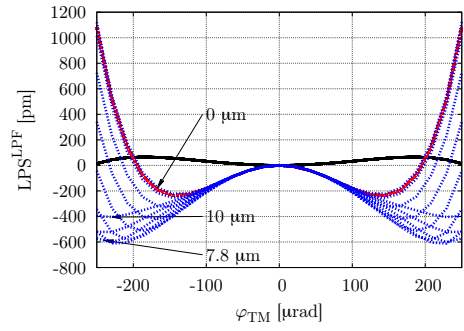
(a) TMIO-M1-EP426-01



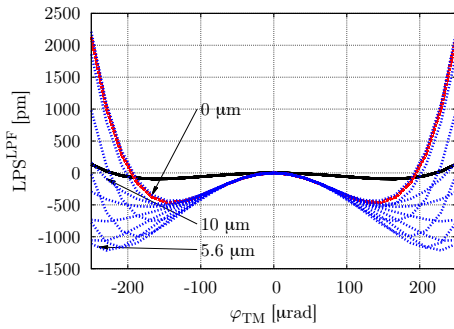
(b) TMIO-M1-EP426-02



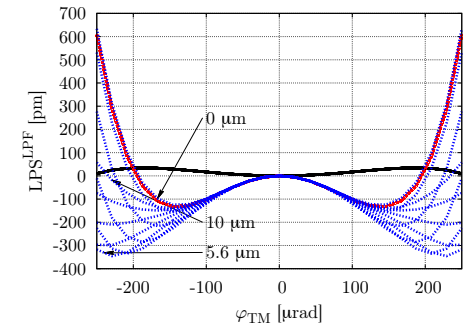
(c) TMIO-M1-EP426-03



(d) TMIO-M1-EP426-04



(e) TMIO-M1-EP426-05



(f) TMIO-M1-EP426-06

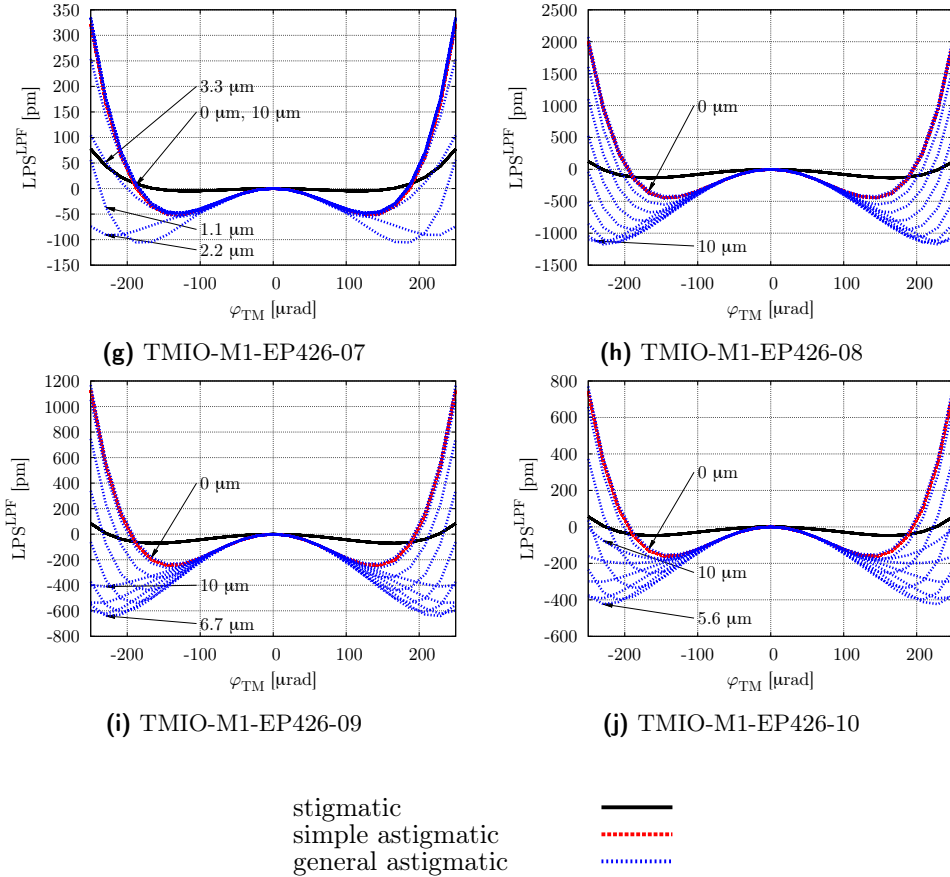
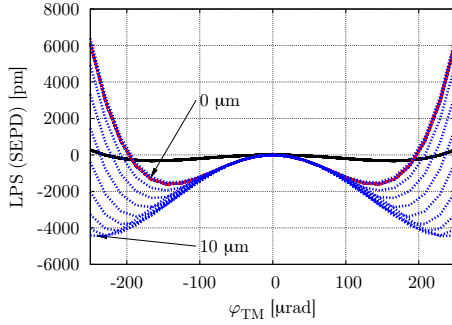
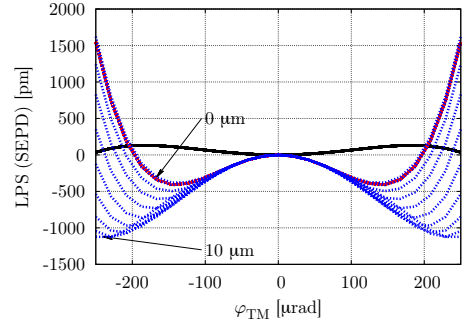


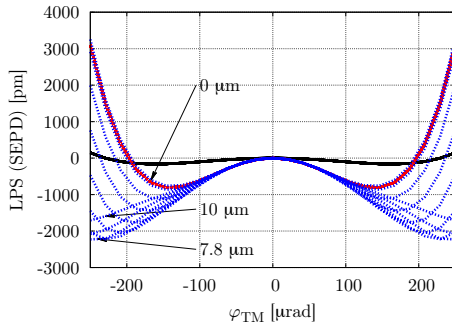
Figure 7.5.: The $LPS^{L,PF}$ on the QPD described in Table 7.1 for the imaging optics systems given in Table 7.2 with the second lens shifted orthogonally to the plane of the measurement beam tilt in 10 equidistant steps from $0 \mu\text{m}$ to $10 \mu\text{m}$. The measurement beam tilts in XZ plane, the second lens shifts along the Y axis. When the second lens is not shifted, the optical system is orthogonal and results obtained with the simple astigmatic model are identical to the results obtained with the general astigmatic model. Arrows show the offsets of the second lens.



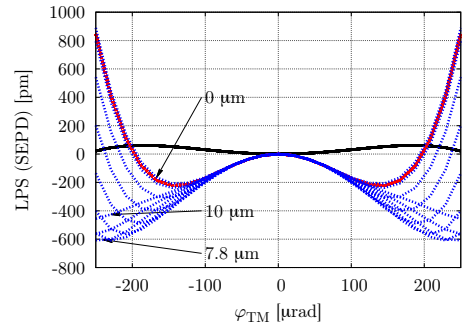
(a) TMIO-M1-EP426-01



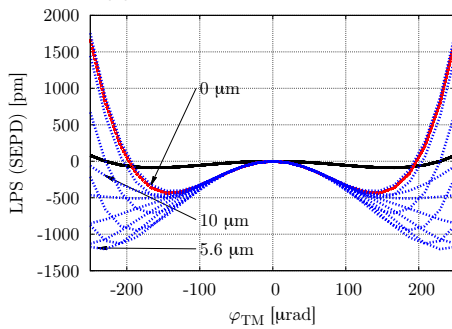
(b) TMIO-M1-EP426-02



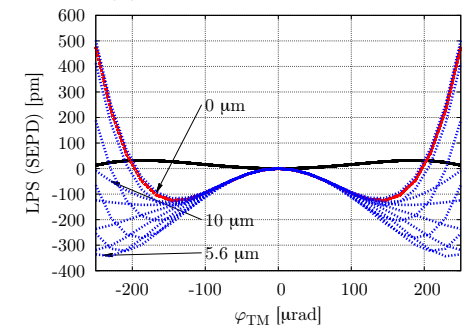
(c) TMIO-M1-EP426-03



(d) TMIO-M1-EP426-04



(e) TMIO-M1-EP426-05



(f) TMIO-M1-EP426-06

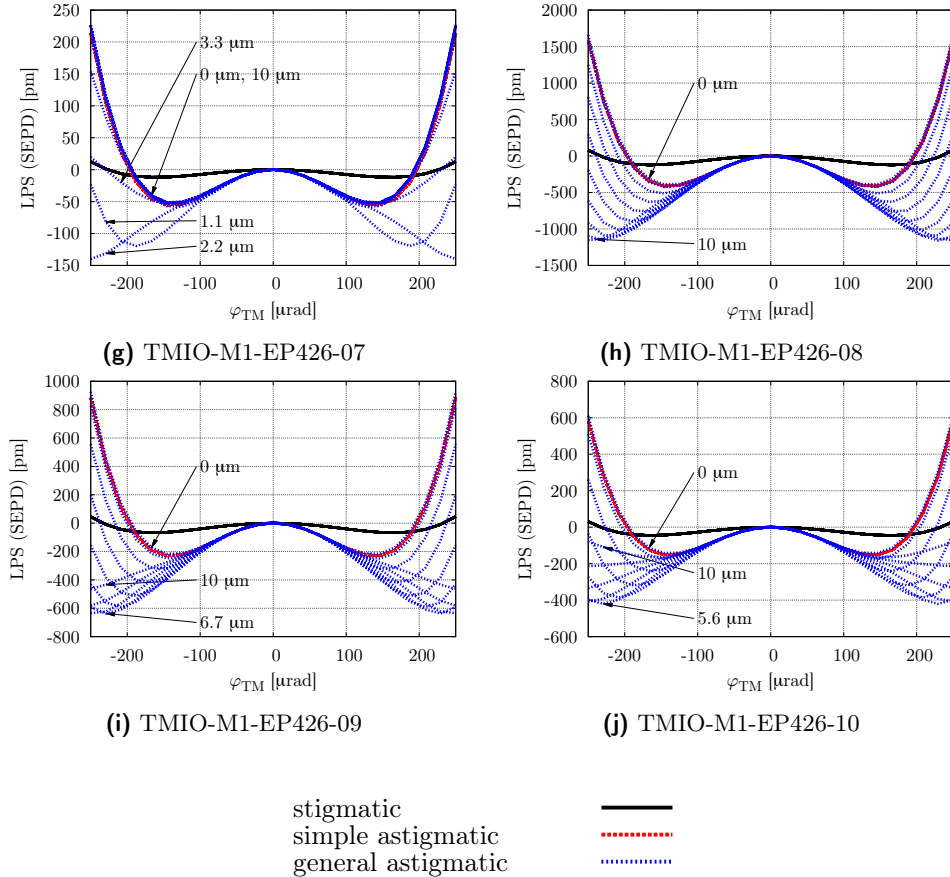


Figure 7.6.: The LPS on the SEPD with the diameter 5.33 mm for the imaging optics systems given in Table 7.2 with the second lens shifted orthogonally to the plane of the measurement beam tilt in 10 equidistant steps from 0 μm to 10 μm . The measurement beam tilts in XZ plane, the second lens shifts along the Y axis. When the second lens is not shifted, the optical system is orthogonal and results obtained with the simple astigmatic model are identical to the results obtained with the general astigmatic model. Arrows show the offsets of the second lens.

are computed identically in all three models. These values change as the second lens is shifted for both reference and measurement beams and thus their relative change is almost negligible and does not cause significant variations of the LPS curve. The q -parameter in the circular model is transformed as if the incidence on the second lens was normal and thus it does not change as the lens shifts from the optical axis. Within the simple astigmatic beam model the q -parameters are transformed as if the optical system stayed orthogonal. The two lens system is an orthogonal optical system only if the second lens is not shifted orthogonally to the plane of the measurement beam tilt. Thus, the q -parameters of the outgoing beam do not change as the lens shifts from the optical axis. Therefore, both stigmatic and simple astigmatic beam models show a very small response to this misalignment. The general astigmatic beam model, in contrary, shows a clear response of the LPS curve on the transversal misalignment of the second lens of the imaging optics system. When the second lens is not shifted from the optical axis, the results obtained with simple and general astigmatic beam models are identical, as expected. The interesting effect that can be observed on the graphs is that for all systems the LPS curve becomes less steep and thus has smaller slope when the second lens is shifted from the optical axis by some distance. For the imaging optics system TMIO-M1-EP426-07 we can also see that its LPS curve obtained with the general astigmatic beam model is relatively stable and for most values of the second lens shift this curve coincides with the curve obtained with the simple astigmatic beam model. Since the second lens in all ten setups is identical I cannot conclude that the LPS curve generally becomes less steep if some specific transversal misalignment of the second lens is introduced. However, it means that in some cases the cross coupling in the misaligned lens system can be smaller than in the aligned lens system.

7.3.3. Realistically misaligned imaging optics

Previously it was shown that in cases where the general astigmatic beam impinges on the photodiode using simplified model of the Gaussian beam in fundamental mode can cause considerable impact on the pathlength readout. However, so far I have only shown the setups, for which all parameters are well known. These estimates would be realistic if all parameters of the optical system were known to sub-micron accuracy. However, such an accuracy cannot be guaranteed so far. Thus, in order to estimate the LPS that will be obtained in the experiment I need to simulate a set of realistically misaligned imaging optics systems. When this set is sufficiently big it is possible to define a range, within which the LPS can lie in the experiment. If this range will differ for different beam models, it will mean that good estimates can only be found with the general astigmatic Gaussian beam model as the most general model that avoids many simplifications. In case if the range is similar for all models it is relevant to conclude that within the current measurement uncertainties the beam model choice does not have a considerable impact.

In order to produce the set of realistically misaligned setups I have varied the positions of lenses and photodiode in longitudinal and both transversal directions within a 10 μm range. For the waist position of both reference and measurement

beams the uncertainty was set to one tens of the Rayleigh range of the beam (see [PD2]). Before entering the imaging optics system both beams are not necessarily ideally circular. The fibers are normally cut at 8° angle [32]. The ellipticity of the beam coming out from the fiber is then $1/\cos 8^\circ \approx 1.01$. Then this beam goes through the fiber outcoupler, which can alter the beam ellipticity. For the upper limit of the beam ellipticity I have chosen the best result that has been achieved in the experimental investigation of the general astigmatic beam (Chapter 6). The first improved beam with the waist radii of $213 \mu\text{m}$ and $218 \mu\text{m}$ has the ellipticity of $218/213 \approx 1.02$. This value was used as the uncertainty in the simulation. All the uncertainties that were implemented in the simulation are summarized in Table 7.3 and Table 7.4.

Table 7.3.: The uncertainties of the parameters of the imaging optics systems in the test mass interferometer.

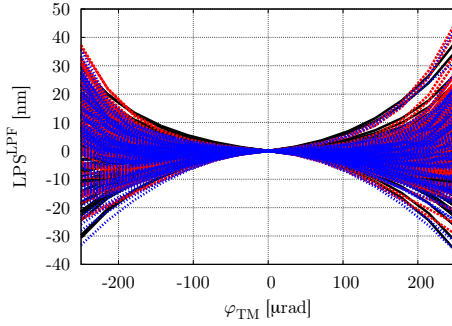
	x [mm]	y [mm]	z [mm]
Lens 1	$\pm 10 \mu\text{m}$	$\pm 10 \mu\text{m}$	$\pm 10 \mu\text{m}$
Lens 2	$\pm 10 \mu\text{m}$	$\pm 10 \mu\text{m}$	$\pm 10 \mu\text{m}$
Photodiode	$\pm 10 \mu\text{m}$	$\pm 10 \mu\text{m}$	$\pm 10 \mu\text{m}$

Table 7.4.: The uncertainties of the beam parameters in the test mass interferometer.

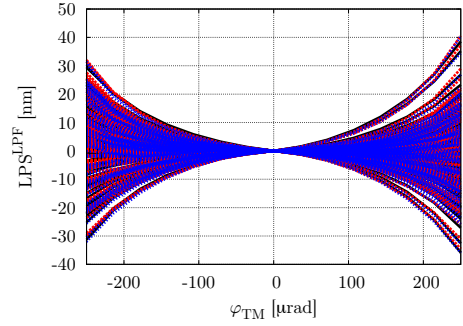
Waist position	$\pm 0.1 z_R \approx 295 \text{ mm}$
Ellipticity	$1/1.02 \dots 1.02$

For each of the ten imaging optics systems 100 realistically misaligned setups have been generated. The parameters of each setup have been chosen randomly and independently from each other within corresponding ranges of uncertainty. I have used the randomizer with the uniform distribution, which means that all values within the uncertainty range was considered to have equal probabilities. Then for each realistically misaligned setup the LPS curves both with QPD and SEPD were produced. As a result for each of the ten imaging optics systems described in Table 7.2 100 realistic LPS curves have been generated with each of the three beam models. The results are shown in Figure 7.7 and Figure 7.8. On these graphs one can see that with the current ranges of uncertainties of the parameters of the imaging optics systems and both reference and measurement beams the ranges of the LPS variations are identical for all three beam models. Thus, within the current measurement uncertainties using a simplified beam model does not introduce significant changes in the main science signal. Therefore, in this case it is sufficient to work with the stigmatic or the simple astigmatic beam models.

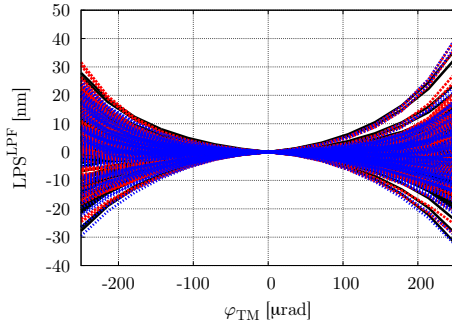
The curves in Figure 7.7 and Figure 7.8 have a maximum slope of $100\text{-}350 \text{ pm}/\mu\text{rad}$, which is above the requirement given in Table 7.1. The cross-coupling can be reduced in the experiment for example by realigning the photodiode longitudinally. In this chapter I have also shown that transversal misalignment of lenses can decrease the



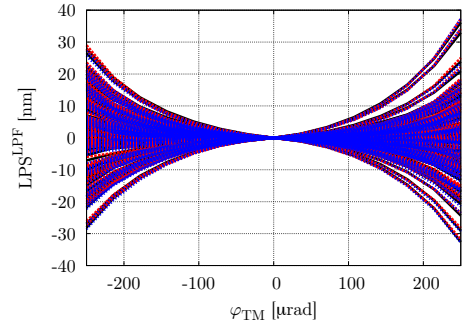
(a) TMIO-M1-EP426-01



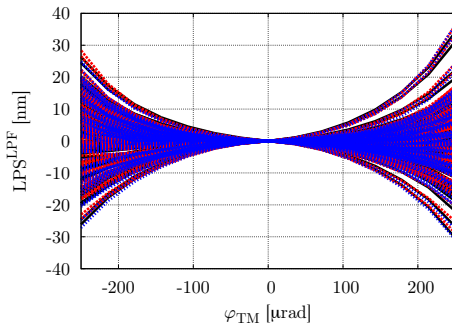
(b) TMIO-M1-EP426-02



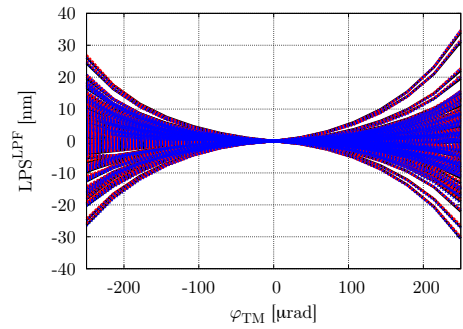
(c) TMIO-M1-EP426-03



(d) TMIO-M1-EP426-04



(e) TMIO-M1-EP426-05



(f) TMIO-M1-EP426-06

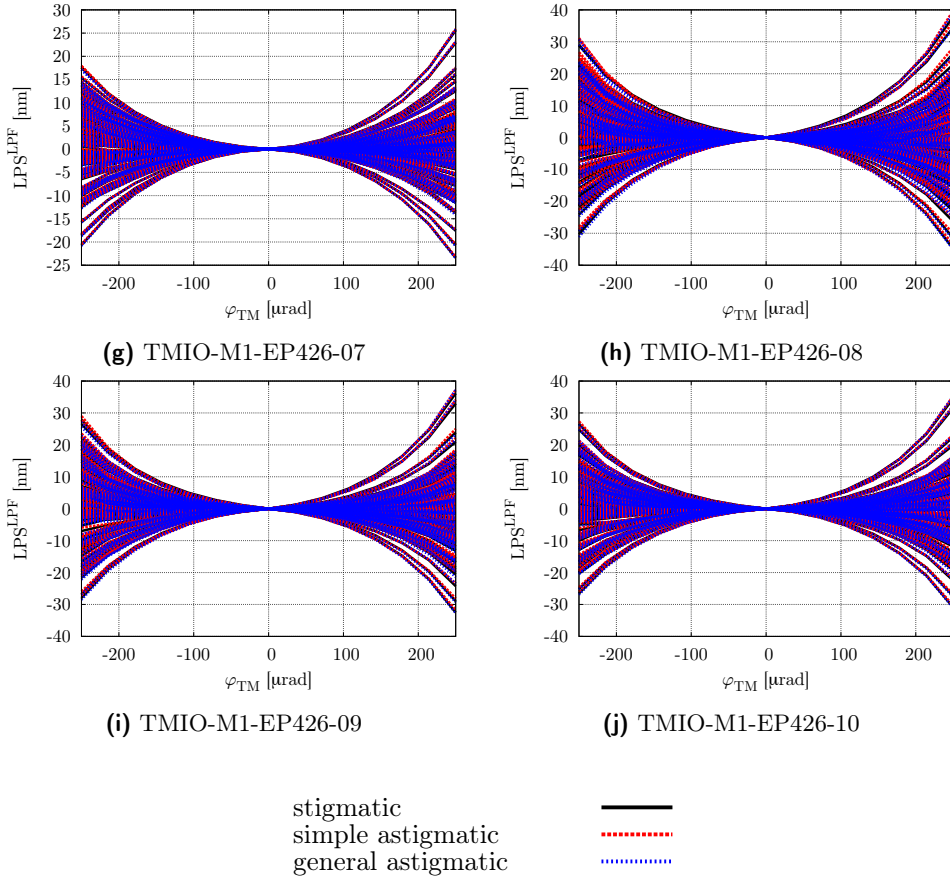
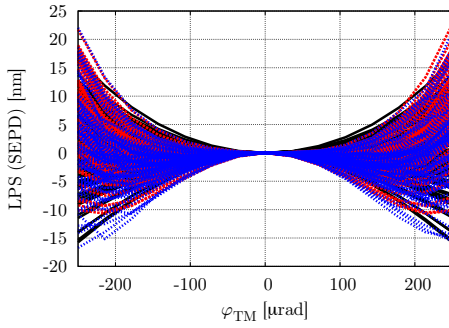
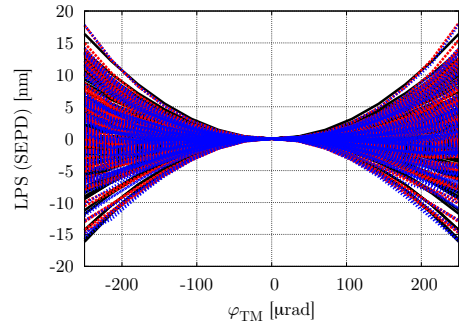


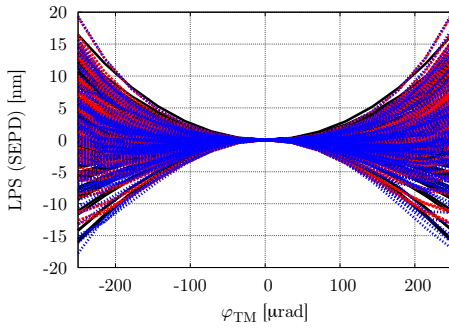
Figure 7.7.: The LPS^{LPF} on the QPD described in Table 7.1 for 100 realistically misaligned variations of each of the imaging optics systems given in Table 7.2.



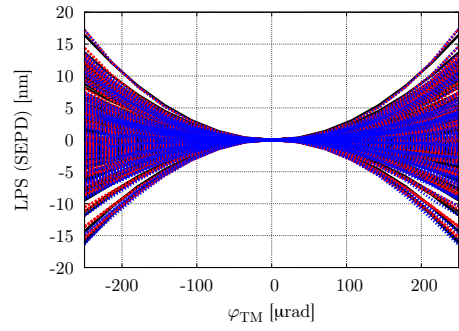
(a) TMIO-M1-EP426-01



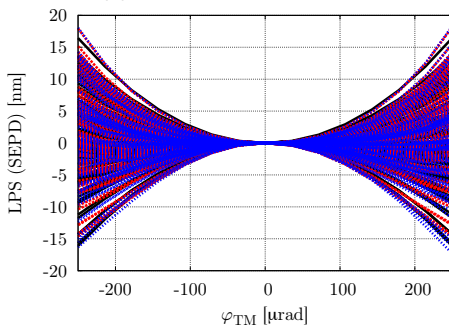
(b) TMIO-M1-EP426-02



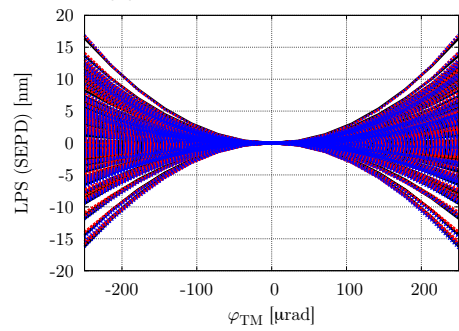
(c) TMIO-M1-EP426-03



(d) TMIO-M1-EP426-04



(e) TMIO-M1-EP426-05



(f) TMIO-M1-EP426-06

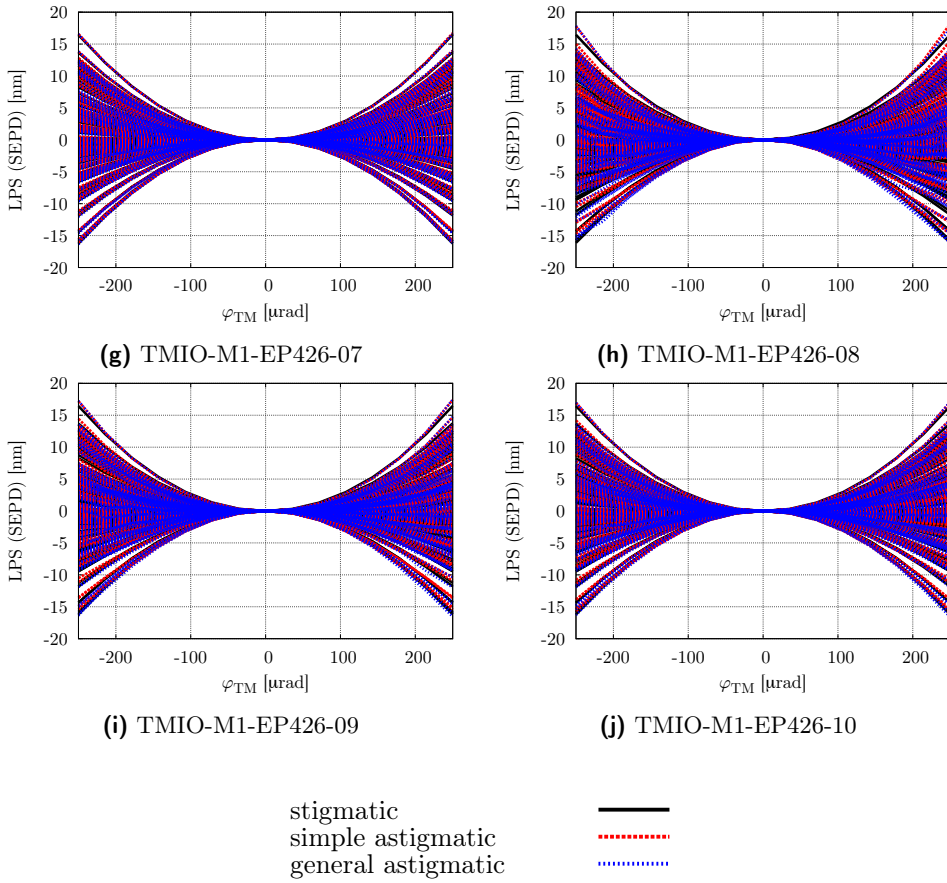


Figure 7.8.: The LPS on the SEPD with the diameter 5.33 mm for 100 realistically misaligned variations of each of the imaging optics systems given in Table 7.2.

slope of the LPS curve. The exact procedure that will lead to sufficient amount of the cross-coupling of the test mass angular jitter into the pathlength signal is out of the scope of this investigation.

It should be noted that for each particular misaligned optical system the results obtained with different beam models might be considerably different. For example, Figure 7.9 shows the LPS for a single instance of the realistically misaligned setup TMIO-M1-EP426-01 with the parameters given in Table 7.5. The difference between the results obtained with each of the three models is clearly visible. This is not surprising. If we look at the specifications of this setup given in Table 7.5, we can see that both beams in this setup are simple astigmatic before they are transformed by the first lens. Since the first lens is misaligned in both transversal directions, even for the reference beam none of its principal axes lies in plane on incidence on the first lens. Thus, both the reference and the measurement beams are transformed into general astigmatic beams already at the first lens. This setup is not symmetrical around the optical axis in the plane of rotation of measurement beam (XZ plane). Thus, the curves are not symmetrical for positive and negative values of the test mass angle. It is interesting to note that the type of curve, obtained with the general astigmatic model on the SEPD, has changed with respect to the fourth order curves that we observed for example in Figure 7.5 and Figure 7.6. This change can be explained by the complex configuration of general astigmatic beams that can couple into the pathlength signal.

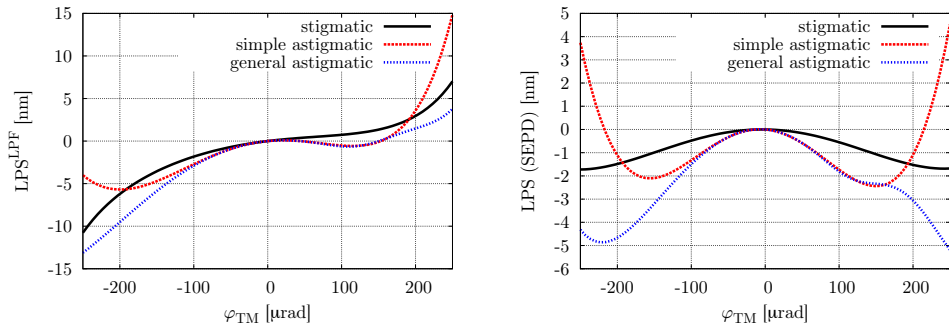


Figure 7.9.: The LPS for QPD (on the left) and SEPD (on the right) for the single instance of the realistically misaligned imaging optics system TMIO-M1-EP426-01 described in Table 7.5.

7.4. Conclusion

In this chapter I have investigated the impact of the beam model choice on the pathlength readout in case when the imaging system that consists of two spherical lenses is used. The absence of a systematic difference between the results obtained with the different beam models for realistically misaligned setups allows the efficient use

Table 7.5.: The parameters of the single instance of the realistically misaligned imaging optics system TMIO-M1-EP426-01.

	z [mm]	x [μm]	y [μm]
Lens 1	425.998	-6.43564	6.23762
Lens 2	448.356	-1.88119	-3.46535
Photodiode	523.577	-2.27723	1.48515
	w_{01} [mm]	w_{02} [mm]	z_0 [mm]
Reference beam	1	0.995686	-143.246
Measurement beam	1	0.989412	-78.9316

of simplified beam models within the current uncertainties of the parameters of the optical systems. This conclusion can be applied quite generally to the systems of the spherical lenses, which do not produce strongly elliptical beams. However, it does not mean that simplified beam models are applicable for all types of optical simulations. In this chapter I have shown that analyzing the particular instances of the lens systems with the simplified beam models can lead to wrong conclusions. For example, the results for the perfectly aligned imaging optics systems show significantly smaller cross coupling of the test mass angular jitter with the circular beam model than with the astigmatic models. The use of stigmatic and simple astigmatic beam models results in very little response of the LPS curve on the transversal misalignment of the second lens of the system, while the use of more accurate general astigmatic beam model results in clear changes of pathlength readout. Therefore, it is preferable to use the general astigmatic beam model in all cases, where the optical system beam propagates through is non-orthogonal.

Summary and outlook

In this thesis I have presented the procedure of simulating laser interferometers with three models of Gaussian beams in fundamental mode. The most general and the most complex model is the general astigmatic Gaussian beam model. It can be used to transform an arbitrary Gaussian beam in fundamental mode impinging at an oblique angle at a surface that can be approximated by a second order equation at the point of incidence. The stigmatic and the simple astigmatic Gaussian beam models are the simplifications of the general astigmatic model. The simple astigmatic beam model can be used to transform circular and simple astigmatic beams incident at an elliptical surface at an oblique angle. However, this transformation will only be accurate if both one of the principal axes of the beam ellipse and one of the principal axes of the surface lie in the plane of incidence. Within the stigmatic beam model for each transformation of the beam at a surface it is assumed that the incidence is normal and the surface is planar or spherical.

All three models make use of the geometrical part of the ray tracing given in Chapter 2. As the beam propagates through the optical system it accumulates phase. Due to the independence of the geometrical part from the choice of the beam model accumulated phase is also identical for all models of Gaussian beams in fundamental mode. The difference between the models comprises the propagation and transformation of q -parameters, which results in different evolution of the wavefront and the intensity pattern along the propagation.

The interferometer signals are computed following the same procedure suggested in Chapter 2 for each of the three models. This procedure involves computation of the complex amplitude of the electric field, which is different for each type of Gaussian beams in fundamental mode.

The circular beam model is relatively well-known and thus well-tested. The sim-

ple astigmatic beam model can be split up into two circular beam representations and thus does not introduce particularly novel phenomena. The general astigmatic beam model is the most complex and appears in the least number of publications. In order to have a complete model I had to comprise fragmented information from different sources and derive several key equations. The resulting model was verified by an experiment. In experiment several configurations of cylindrical lenses were used. Each configuration consisted of the two lenses, oriented at an oblique angle with respect to each other in the plane, orthogonal to the beam axis. The stigmatic or simple astigmatic beam is transformed into a general astigmatic beam by such a configuration. The evolution of the intensity ellipse of the resulting general astigmatic beam, obtained in the experiment and in the simulation, was compared. A very good agreement between the simulation and the experiment was achieved. It is planned to perform the similar comparison of the evolution of the wavefront.

The main motivation to study different models of Gaussian beams in fundamental mode was the question that arose while designing imaging optics systems for LISA. We knew that in the aligned system of two spherical lens the tilted measurement beam can be transformed into a simple astigmatic one. Later we found out that in a misaligned system it can even become general astigmatic. Using a simplified beam model can affect the simulation results for the main science signal. In order to understand how big can be the impact of the simplifications I have studied all three models and used them in the simulations of the cross coupling of the test mass angular jitter into the longitudinal pathlength signal. The ranges of uncertainty of the longitudinal pathlength signals are identical for all three models with the current alignment possibilities. Thus, within the current measurement uncertainties it is sufficient to use simplified model to estimate the cross coupling of the test mass angular jitter into the pathlength readout. However, for the single instance of the misaligned imaging optics system that consists of two spherical lens the results obtained with the different models can be clearly different with respect to each other. The analysis of the impact of the specific misalignment can also show different results depending on the beam model choice. Therefore, it is preferable to use the general astigmatic beam model for the optical simulations of non-orthogonal optical systems.

The study of different beam models provided in this thesis enables a precise understanding of the circumstances, under which one type of Gaussian beam in fundamental mode can be transformed into another. With this knowledge one can make a well-motivated choices of the appropriate beam model for each particular investigation. Having accurate beam models in the simulation tool allows precise evaluation of various effects. With the general astigmatic beam model we are not limited to spherical and planar surfaces. Using second order approximation at the point of incidence, we can simulate beam transformations at a large variety of surfaces.

Curvature matrix of second order surface

The curvature matrix of a surface is used in transformation of general astigmatic beam via reflection or refraction (equations (5.64), (5.65)). This appendix will be dedicated to the derivation of a curvature matrix at some point on a second order surface. The derivation of the curvature matrix of ellipsoidal surface can equally well be used for cylindrical surfaces. The case of spherical surface will be considered separately. Thus I will cover several common types of surfaces, used in interferometers, including spherical and cylindrical lenses.

A.1. Curvature matrix of ellipsoidal surface

The ellipsoidal surface (see Figure A.1) can be described using the following expression in its nominal coordinate system $(\hat{s}_1, \hat{s}_2, \hat{s})$, related to the center of the ellipsoid O :

$$f(\mathbf{x}, z) = x_1^2 c_1^2 + x_2^2 c_2^2 + z^2 c^2 - 1 = 0. \quad (\text{A.1})$$

In principal coordinate system $(\hat{s}_1, \hat{s}_2, \hat{s})$ each of the three unity vectors is aligned with one of the principal semi-axes of ellipsoid. Here $\mathbf{x} = (x_1, x_2, z)$ is the vector in coordinate system $(\hat{s}_1, \hat{s}_2, \hat{s})$, where of transversal coordinates x_1 and x_2 correspond to unity vectors \hat{s}_1, \hat{s}_2 , coordinate z corresponds to \hat{s} . Values $1/c_1, 1/c_2$ and $1/c$ are the principal semi-axes of ellipsoid; c_1, c_2 and c are its principal curvatures.

Equation (A.1) can be rewritten as:

$$f(\mathbf{x}) = \mathbf{x}^T A \mathbf{x} - 1 = 0, \quad (\text{A.2})$$

where

$$A = \begin{pmatrix} c_1^2 & 0 & 0 \\ 0 & c_2^2 & 0 \\ 0 & 0 & c^2 \end{pmatrix} \quad (\text{A.3})$$

In order to derive the curvature matrix at some arbitrary point on a surface O' , we need to rewrite equation (A.1) in the local coordinate system $(\hat{d}_1, \hat{d}_2, \hat{n})$. This coordinate system is related to the point O' , unity vector \hat{n} is a local normal vector to the surface at the point of interest O' . Unity vectors \hat{d}_1 and \hat{d}_2 are the arbitrary vectors in the plane, tangential to the surface at the point O' , chosen such as the local coordinate system is orthonormal.

Assume \mathbf{x}' is a vector (x'_1, x'_2, z') in a local coordinate system $(\hat{d}_1, \hat{d}_2, \hat{n})$. To transform the principal coordinate system of the surface into local coordinate system we need to find the parameters of the affine transformation:

$$\mathbf{x}' = M\mathbf{x} + \mathbf{t} \quad (\text{A.4})$$

In the center of ellipsoid O this equation becomes:

$$\mathbf{x}' = \mathbf{t}. \quad (\text{A.5})$$

Since the point O in local coordinate system $(\hat{d}_1, \hat{d}_2, \hat{n})$ can be described by vector $\vec{O'O}$, the elements of vector \mathbf{t} can be found as the projections of a vector $\vec{O'O}$ on vectors $\hat{d}_1, \hat{d}_2, \hat{n}$.

If we take $\mathbf{x} = \mathbf{s}$ and $\mathbf{x}' = \mathbf{n}$ in equation (A.4), we can obtain rotation matrix M using for example algorithm [38]. Then

the transversal vectors of the local coordinate system can be found from:

$$\hat{d}_i = \hat{s}_i M, \quad i = 1, 2. \quad (\text{A.6})$$

Taking into account the fact that rotation matrix M satisfies expression $M^{-1} = M^T$, we can find the coordinate vector \mathbf{x} from equation (A.4):

$$\mathbf{x} = M^T(\mathbf{x}' - \mathbf{t}). \quad (\text{A.7})$$

Substituting this expression into equation (A.2), we obtain the equation of surface in local coordinate system:

$$f(\mathbf{x}') = (M^T(\mathbf{x}' - \mathbf{t}))^T A (M^T(\mathbf{x}' - \mathbf{t})) - 1 = 0, \quad (\text{A.8})$$

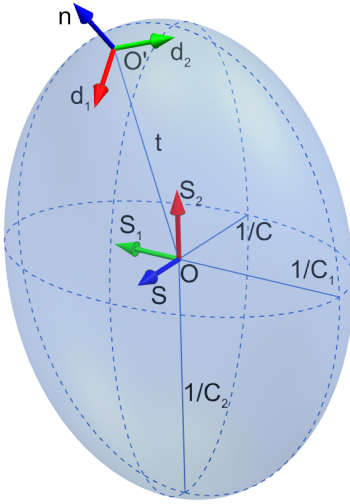


Figure A.1.: Coordinate transformation for an ellipsoidal surface.

which is equivalent to

$$f(\mathbf{x}') = (\mathbf{x}' - \mathbf{t})^T A' (\mathbf{x}' - \mathbf{t}) - 1 = 0, \quad (\text{A.9})$$

where

$$A' = MAM^T. \quad (\text{A.10})$$

Since matrix A is diagonal and matrix M is a rotation matrix, matrix A' is symmetric.

After equation (A.1) is rewritten in the local coordinate system, we can obtain the expression for coordinate z' , aligned with the surface normal \hat{n} . Assuming that the curvature $c \neq 0$ (otherwise the surface would be flat at the point of incidence) we can now derive the equation for z' from equation (A.8) :

$$z' = t_3 - \frac{a'_{13}\bar{x}_1 + a'_{23}\bar{x}_2}{a'_{33}} \pm \frac{1}{a'_{33}} \sqrt{(a'_{13}\bar{x}_1 + a'_{23}\bar{x}_2)^2 - a'_{33}(a'_{11}(x_1'^2 - t_1) + 2a'_{12}\bar{x}_1\bar{x}_2 + a'_{22}\bar{x}_2^2 - 1)} \quad (\text{A.11})$$

Here a'_{ij} with $i, j = 1, 2, 3$ are elements of matrix A' , $\bar{x}_i = x'_i - t_i$ with $i = 1, 2$, t_i with $i = 1, 2, 3$ are the elements of vector \mathbf{t} .

Finding second order derivative of the obtained expression with respect to coordinates x'_1 and x'_2 will give the required curvature matrix.

$$C = \begin{pmatrix} \frac{\partial^2 z'_1}{\partial x_1'^2} & \frac{\partial^2 z'_1}{\partial x'_1 \partial x'_2} \\ \frac{\partial^2 z'_1}{\partial x'_2 \partial x'_1} & \frac{\partial^2 z'_1}{\partial x_2'^2} \end{pmatrix} = \pm \frac{1}{b} \begin{pmatrix} a'_{11}a'_{33} - a'_{13}{}^2 + gt_2^2 & a'_{12}a'_{33} - a'_{13}a'_{23} - gt_1t_2 \\ a'_{12}a'_{33} - a'_{13}a'_{23} - gt_1t_2 & a'_{22}a'_{33} - a'_{23}{}^2 + gt_1^2 \end{pmatrix}, \quad (\text{A.12})$$

where

$$b = [(a'_{13}t_1 + a'_{23}t_2)^2 - a'_{33}(a'_{11}t_1^2 + 2a'_{12}t_1t_2 + a'_{22}t_2^2 - 1)]^{3/2}, \quad (\text{A.13})$$

$$g = a'_{11}a'_{23}{}^2 + a'_{22}a'_{13}{}^2 + a'_{33}a'_{12}{}^2 - 2a'_{12}a'_{13}a'_{23} - a'_{11}a'_{22}a'_{33}.$$

Equation (A.12) provides the required expression for the curvature matrix at an arbitrary point on an ellipsoidal surface. Even though it was derived for ellipsoidal surfaces, nothing stops us from having zero curvature in one of the directions \hat{s}_1 or \hat{s}_2 . Then equation (A.12) will provide the curvature matrix for cylindrical surface. Negative curvatures can also be treated by changing the sign of the curvature matrix. Therefore the described case is general for any 2nd-order surface in 3D.

A.2. Curvature matrix of spherical surface

In this section I will derive the curvature matrix of a spherical surface as a special case of ellipsoidal surface. For this type of surfaces the matrix A given in equation (A.3) is defined as

$$c^2 E, \quad (\text{A.14})$$

where E is a unity matrix. The principal curvatures of spherical surface in its principal coordinate system are identical in all three directions. Then equation (A.10) becomes:

$$A' = M(c^2 E)M^T = c^2 M M^T = c^2 M M^{-1} = c^2 E = A. \quad (\text{A.15})$$

Since normal vector \hat{n} for spherical surface is always aligned along the radius of a sphere, $t_1 = t_2 = 0$, $t_3 = 1/c$. Substituting these values into equation (A.12) we obtain:

$$\begin{aligned} b &= c^3, \\ g &= -c^6. \end{aligned} \quad (\text{A.16})$$

Then from equation (5.55) the curvature matrix at any point on a spherical surface is independent on the choice of the coordinate system $(\hat{d}_1, \hat{d}_2, \hat{n})$:

$$C = \pm \frac{1}{c^3} \begin{pmatrix} c^4 & 0 \\ 0 & c^4 \end{pmatrix} = \pm \begin{pmatrix} c & 0 \\ 0 & c. \end{pmatrix} \quad (\text{A.17})$$

Algorithm of the optimal setup search

This appendix is dedicated to the simulation for the optimal setup search that was used in experimental verification of the general astigmatic Gaussian beam model. This simulation searches through the variety of possible configurations of the two cylindrical lenses that transform the initial circular or simple astigmatic Gaussian beam into general astigmatic. The goal is to find a configuration that produces general astigmatic beam with the clearly observable rotation of the intensity ellipse according to criteria from Chapter 6.

I will start this chapter with the overview of the possible two lens configurations. Then I will present the algorithm for the optimal setup search. In the end I will put the code listing of the simulation that can be used together with our in-house software IfoCad P4.

B.1. Possible two lens configurations

In our study we had three cylindrical lenses available. It does not seem to be many. However, a large variety of different two lens setups producing different general astigmatic beams can be built using these lenses.

Two or three lenses are plano-convex. Thus each of them can be put in the setup either facing the incoming beam with the plane surface or with the convex surface. Taking into account that we only have one sample of each lens types, it is possible to combine our lenses into 16 different configurations (see Table B.1).

In order to produce the general astigmatic beam the transversal relative angle $\Delta\alpha$ between two cylindrical lenses can take any value between 0° and 90° (not including edges). Implementing relative angle $\Delta\alpha$ of more than 90° does not add new possibilities, since the intensity ellipse evolution in this case will be identical to the one for

Table B.1.: Possible combinations of two cylindrical lenses.

	Lens1 ($a = 1$)	Lens1 ($a = -1$)	Lens2 ($a = 1$)	Lens2 ($a = -1$)	Lens3 ($a = 0$)
Lens1 ($a = 1$)	✗	✗	✓	✓	✓
Lens1 ($a = -1$)	✗	✗	✓	✓	✓
Lens2 ($a = 1$)	✓	✓	✗	✗	✓
Lens2 ($a = -1$)	✓	✓	✗	✗	✓
Lens3 ($a = 0$)	✓	✓	✓	✓	✗

$\Delta\alpha - 90^\circ$, just mirrored. We can look at different relative angles in steps of 5° starting with 5° and ending with 85° . Such step size should be sufficient to look at all important possibilities on the one hand and avoid too many similar computations of the other hand. The angle of orientation of the first lens in the transversal plane can be set to zero, then angle of the second lens is identical to the relative orientation of both lenses $\alpha_2 = \Delta\alpha$.

Another parameter that should be varied in the optimal setup search is the distance between the two lenses Δz . It is hard to set the limits for this parameter since it can be almost arbitrary. We decided to restrict ourselves to the distances between 3 cm and 20 cm since such distances are convenient to be implemented in the experiment. It was chosen to vary the distance between two lenses in 5 steps. Such choice again allows to evaluate all interesting possibilities avoiding too many computations. The position of the first lens was set to $z_1 = 1$ cm. The position of the second lens was varied according to the variations of distance between the two lenses.

We could include even more parameters in this investigation. For instance, we could vary the angles of both lenses separately. The suggested variations already produce $16 \times 17 \times 5 = 1360$ possibilities, which is already impossible to explore manually and hard enough to explore in the simulation. It is also not necessary to add more possibilities. as it is shown in chapter 6, the suggested approach allows to find a really good lens configuration with a very clearly observable rotation of the intensity ellipse.

B.2. Algorithm description

The simulation starts with constructing the list of all available lenses (see Figure B.1). If the lens is asymmetric (for example, plano-convex), it is added twice in the list: once with the positive asymmetry parameter (in case of plano-convex lens planar surface faces the incoming beam, $a = 1$) and once with the negative asymmetry parameter (in case of plano-convex lens convex surface faces the incoming beam, $a = -1$).

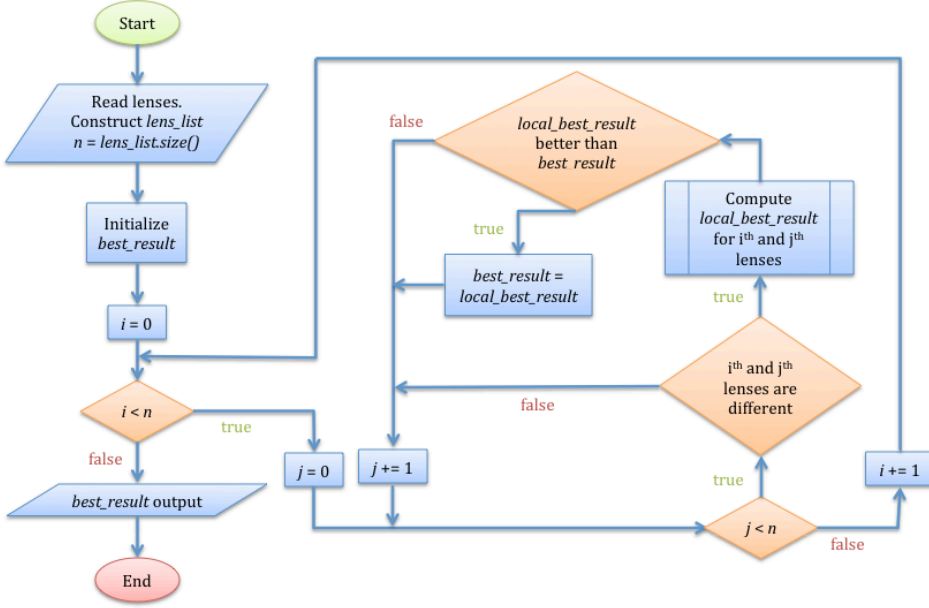


Figure B.1.: The flowchart of the algorithm of the optimal setup search.

Then for each pair of different lenses from the list several distances between lenses (in our case from 3 cm to 20 cm in 5 equidistant steps) and several angles of the second lens (in our case from 5° to 85° in 17 equidistant steps) are tried out (see Figure B.2).

For each particular lens configuration the initial simple astigmatic beam is traced through the setup. After the second lens it transforms into general astigmatic beam. This beam is propagated over some specific distance (in our case 25 cm) behind the second lens. Along this propagation several values are computed (see Figure B.3):

1. total change of the intensity ellipse angle over the propagation distance ($|\Delta\varphi_w|$);
2. maximum slope of the intensity ellipse angle evolution over the propagation distance ($|\partial\varphi_w/\partial z|_{\max}$);
3. minimum flattening of the intensity ellipse over the propagation distance (F_{\min});
4. distance behind the second lens, where spot size requirement is violated ($z_w > 1.25$).

Using these values, each setup (*new_result*) is compared to the so far found best setup (*best_result*) as described below.

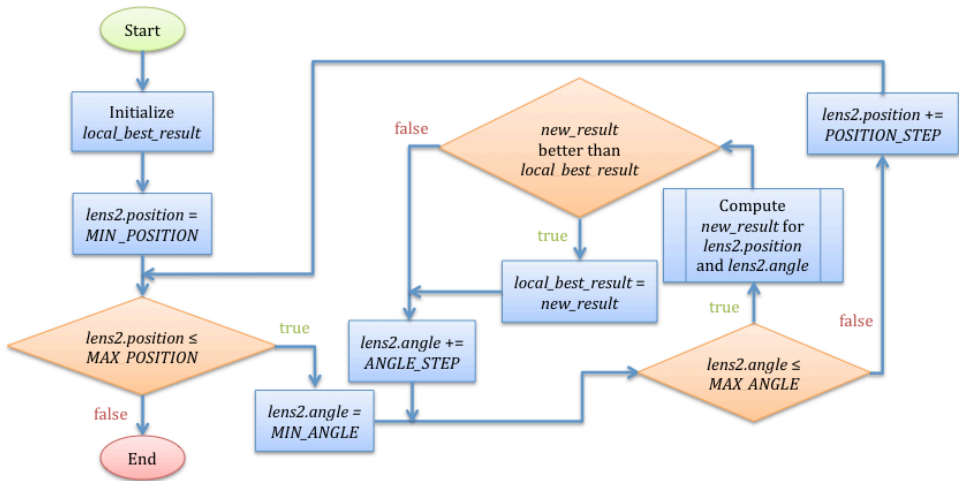


Figure B.2.: The flowchart of the algorithm of the local best result search with the two specific cylindrical lenses.

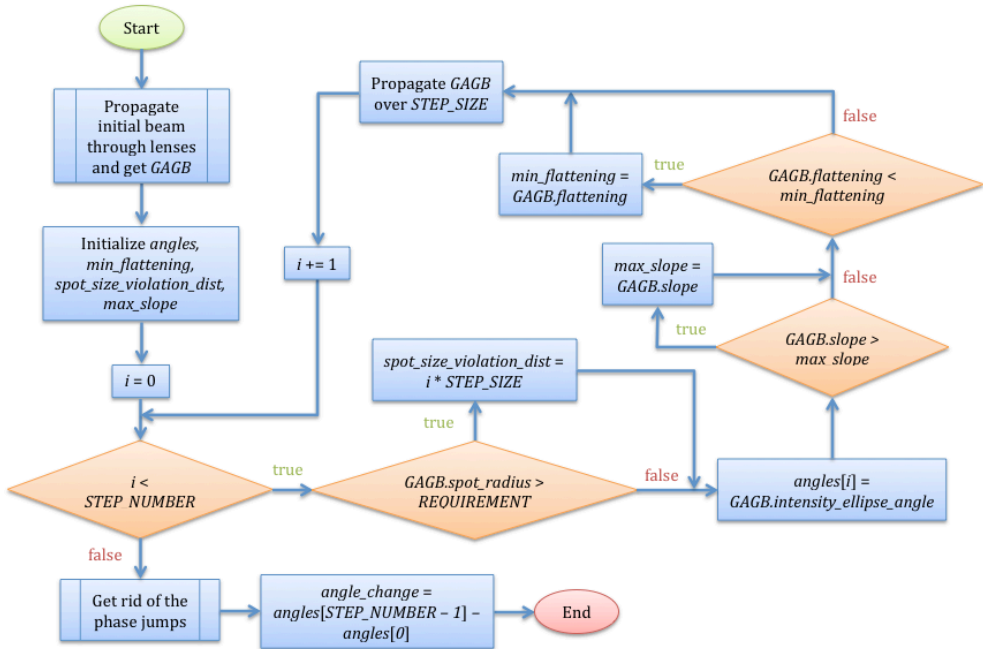


Figure B.3.: The flowchart of the algorithm of the local best result search with the specific configuration of the two cylindrical lenses.

1. First for each of the four parameters their normalized difference is computed:

$$\begin{aligned}
\Delta(F_{\min}) &= \frac{F_{\min}(new_result) - F_{\min}(best_result)}{F_{\min}(best_result)} \\
\Delta(|\Delta\varphi_w|) &= \frac{|\Delta\varphi_w(new_result)| - |\Delta\varphi_w(best_result)|}{|\Delta\varphi_w(best_result)|} \\
\Delta\left(\left|\frac{\partial\varphi_w}{\partial z}\right|_{\max}\right) &= -\frac{\left|\frac{\partial\varphi_w}{\partial z}\right|_{\max}(new_result) - \left|\frac{\partial\varphi_w}{\partial z}\right|_{\max}(best_result)}{\left|\frac{\partial\varphi_w}{\partial z}\right|_{\max}(best_result)} \\
\Delta(z_{w>1.25}) &= \frac{z_{w>1.25}(new_result) - z_{w>1.25}(best_result)}{z_{w>1.25}(best_result)}
\end{aligned} \tag{B.1}$$

2. Then the weighted sum of the found normalized differences is found:

$$\begin{aligned}
\Delta &= w(F_{\min})\Delta(F_{\min}) + w(|\Delta\varphi_w|)\Delta(|\Delta\varphi_w|) + \\
&\quad w\left(\left|\frac{\partial\varphi_w}{\partial z}\right|_{\max}\right)\Delta\left(\left|\frac{\partial\varphi_w}{\partial z}\right|_{\max}\right) + w(z_{w>1.25})\Delta(z_{w>1.25})
\end{aligned} \tag{B.2}$$

Initially all parameters are equally important and have weights of 0.25. But as soon as some parameter for both *new_result* and *best_result* becomes "better" than some fixed sufficient value, it's weight drops by a factor of 10. For fl_{\min} the value of 0.33 (major semi-axes is 1.5 times bigger than minor semi-axes in every point) is considered to be sufficient, slope of no more than $1^\circ/\text{mm}$ and angle change of at least 100° are also sufficient. We aim for having beam smaller than 1.25 at all propagation distance and we don't look at the points further than propagation distance, therefore propagation distance is maximum possible value for $z_{w>1.25}$. If both for new and for best result this is the case, this parameter doesn't count anyway. Otherwise it doesn't make sense to drop it's weight.

3. If the resulted sum is positive, *new_result* becomes *best_result*.

This algorithm allows to find an optimal setup through a set of comparisons between the performances of different setups.

B.3. Code listing

code/gagb_max_effect_cyl.cpp

```

1 /**
2  The simulation is searching for the setup with 2 cylindrical
3  lenses , that produces the most significant general astigmatic
4  effect. Ideally it finds a setup with the biggest intensity
5  ellipse angle change over some fixed propagation distance ,
6  smallest slope of this change (or rotation "speed")
7  and biggest intensity ellipse flattening
8  (f = 1 - spot_rad_2 / spot_rad_1).
9  If it's not possible , the closest to the "best" setup will be

```

```

10 found.
11 To fit into the CCD-camera beam shouldn't be larger than some
12 fixed value. This is also taken into account.
13 All results are listed in a table.
14 Future investigation can be performed using separate program.
15 */
16
17 #include <fstream>
18 #include <sstream>
19 #include <iostream>
20 #include <iomanip>
21
22 /* IFOCAD files */
23 #include "../.../source/beams/ga_gbeam.h"
24 #include "../.../source/tracing/beam_tracing.h"
25
26 /* local files */
27 #include "phase_jumps.h"
28 #include "cylindrical_lenses.h"
29
30 //=====Result structure=====
31 /**
32  * This structure is used to represent the result of the beam
33  * propagation through the 2-lens setup.
34  * It contains
35  * - the parameters of the setup (lenses and their relative
36  * position) - sufficient data to reconstruct the setup if needed;
37  * - the key values for setup comparison (minimum flattening,
38  * maximum slope, angle change and distance, where spot size
39  * requirement is violated).
40  */
41 struct Result
42 {
43     // Index of the first lens in the lens list
44     unsigned int lens1;
45     // Index of the second lens in the lens list
46     unsigned int lens2;
47     // Angle of the second lens
48     double lens2_ang;
49     // Distance between the 2 lenses
50     double lens2_dist;
51     // Minimum flattening of the intensity ellipse over the
52     // propagation distance
53     double min_flattening;
54     // Maximum slope of the intensity ellipse angle curve over the
55     // propagation distance
56     double max_slope;
57     // Angle change over the propagation distance
58     double angle_change;
59     // Distance behind the second lens, where spot size requirement
60     // is violated
61     double spot_size_violation_dist;
62 };
63 //=====Function declarations=====
64 /**
65  * Initialises result with unrealistically "bad" ("worse" than

```

```

66 * anything that can be produced by real lenses) parameters.
67 */
68 void init_result (Result &result);
69 /**
70 * Returns true if new_result is "better" than prev_best_result.
71 * 4 parameters are taken into account:
72 * - minimum flattening (ellipticity) over propagation distance;
73 * - maximum slope [angle / distance] over propagation distance;
74 * - angle change over propagation distance;
75 * - distance, where spot size starts to violate the requirement.
76 * For each parameter normalized difference between new_result
77 * and prev_best_result is computed. If the weighted sum of 4
78 * normalized differences is positive, the new result is "better".
79 */
80 bool compare_results(const Result &new_result, const Result
81                    &prev_best_result);
82 /**
83 * Copies to_copy to result.
84 */
85 void copy_result(Result &result, const Result &to_copy);
86 /**
87 * Computes best result for the setup containing lens1 as the first
88 * lens and lens2 as the second lens. The first lens always stays at
89 * 1 cm and 0 degree angle. The distance between lenses is varied
90 * between LENS1_LENS2_MIN_DISTANCE and LENS1_LENS2_MAX_DISTANCE
91 * in NUMBER_DISTANCE_STEP steps. The angle of the second lens is
92 * varied between LENS2_MIN_ANGLE and LENS2_MAX_ANGLE in
93 * NUMBER_ANGLE_STEP steps.
94 */
95 void get_result_for_lens1_lens2(Beamsplitter lens1, Beamsplitter
96                                lens2, Result &best_result);
97 /**
98 * Computes result for the specific setup containing lens1 and lens2
99 * with fixed distance between lenses and angle of the second lens.
100 */
101 void get_result_for_setup(Beamsplitter &lens1, Beamsplitter &lens2,
102                           Result &result);
103 /**
104 * Propagates GAGB and computes phase jump, angle change, distance
105 * where spot size requirement is violated, minimum flattening and
106 * maximum slope.
107 */
108 void propagate_and_get_results(GA_GBeam beam, bool &inc, double
109                               &added, double &angle, double &spot_size_violation_dist,
110                               double &min_flattening, double &max_slope);
111 /**
112 *  $f = 1 - \text{spot\_rad\_2} / \text{spot\_rad\_1}$ , where  $\text{spot\_rad\_2} \leq \text{spot\_rad\_1}$ 
113 * http://en.wikipedia.org/wiki/Flattening
114 * http://www.gmat.unsw.edu.au/snap/gps/clynch\_pdfs/ellipsequ.pdf
115 */
116 double flattening(double spot_rad_1, double spot_rad_2);
117 /**
118 * Computes the absolute value of the slope of the intensity ellipse
119 * angle at a current beam position.
120 */
121 double angle_slope_abs(GA_GBeam beam);

```

```

122 /**
123  * Prints out the found best setup.
124  */
125 void print_best_result_to_file(const std::string &file_name,
126     const std::vector<lens> &lens_list, const Result &best_result);
127 //=====Constants=====
128
129 // Beam parameters
130 static const double WAIST_X_RAD = 295 * UM;
131 static const double WAIST_Y_RAD = 253 * UM;
132 static const double WAIST_X_POS = 0.82 * MM;
133 static const double WAIST_Y_POS = 1.01 * MM;
134 static const double BEAM_ANGLE = 0 * DEGREE;
135
136 // Lens positions
137 static const double LENS1_POSITION = 10;
138 static const double LENS1_LENS2_MIN_DISTANCE = 30;
139 static const double LENS1_LENS2_MAX_DISTANCE = 200;
140 static const int NUMBER_DISTANCE_STEP = 5;
141
142 // Second lens angle
143 static const double LENS2_MIN_ANGLE = 5 * DEGREE;
144 static const double LENS2_MAX_ANGLE = M_PI / 2 - 5 * DEGREE;
145 static const int NUMBER_ANGLE_STEP = 17;
146
147 // Propagation distance behind the second lens (after GAGB appears)
148 static const double PROPAGATION_DISTANCE = 250;
149 static const int NUMBER_PROPAGATION_STEP = 10;
150
151 // Spot size requirements
152 static const double MAX_SPOT_RADIUS = 2.5 / 2.0;
153
154 // Const for angle slope derivation
155 static const double DIST_CHANGE_SLOPE = 1.0;
156
157 // Values that are used in comparison of the results
158 enum { MIN_FL, MAX_SL, ANG_CH, SP_S_DIST, COMPARE_NUM };
159
160 // Weights of parameters
161 static const double WEIGHTS[] = { 0.25, 0.25, 0.25, 0.25 };
162
163 // Sufficient parameter values
164 static const double SUFFICIENT_FLATTENING = 0.33;
165 static const double SUFFICIENT_SLOPE = DEGREE;
166 static const double SUFFICIENT_ANG_CHANGE = 100 * DEGREE;
167
168 // Constant, by which weight is reduced after value becomes
169 // sufficient
170 static const double REDUCE_CONST = 10.0;
171
172 // CCD camera parameters
173 static const double CCD_LONG_OFFSET = 7.2;
174 static const double CCD_ANG_OFFSET = 0.0;
175
176 static const Direction_3d X_AXIS = Direction_3d(1, 0, 0);
177

```



```

178 //=====Implementation=====
179
180 double angle_slope_abs(GA_GBeam beam)
181 {
182     // In case if phase jump happens between ang_0 and ang_dif, the
183     // slope will be too high. But the phase jump can't happen in
184     // both positive and negative direction of propagation, since
185     // DIST_CHANGE_SLOPE is too small for both phase jumps to happen
186     // within (-DIST_CHANGE_SLOPE; DIST_CHANGE_SLOPE). Therefore to
187     // avoid taking phase jump into account we will compute slopes
188     // in both directions and return the smallest.
189
190     // Angle at the current beam origin
191     double ang_0 = beam.intensity_angle();
192
193     // Propagation in positive direction
194     beam.propagate(DIST_CHANGE_SLOPE);
195     double ang_dif_1 = beam.intensity_angle();
196     double ang_change_1 = fabs(ang_dif_1 - ang_0);
197
198     // Propagation in negative direction
199     beam.propagate(-2 * DIST_CHANGE_SLOPE);
200     double ang_dif_2 = beam.intensity_angle();
201     double ang_change_2 = fabs(ang_dif_2 - ang_0);
202
203     // Choosing the smaller slope
204     if (ang_change_1 < ang_change_2)
205         return ang_change_1 / DIST_CHANGE_SLOPE;
206     else
207         return ang_change_2 / DIST_CHANGE_SLOPE;
208 }
209
210 bool compare_results(const Result &new_result, const Result
211                    &prev_best_result)
212 {
213     std::vector<double> compare_res;
214     compare_res.resize(COMPARE_NUM, false);
215
216     compare_res[MIN_FL] = new_result.min_flattening -
217     prev_best_result.min_flattening;
218     if (fabs(prev_best_result.min_flattening) > DBL_EPSILON)
219         compare_res[MIN_FL] /= prev_best_result.min_flattening;
220
221     if (prev_best_result.max_slope == INFINITY)
222         compare_res[MAX_SL] = new_result.max_slope;
223     else
224         compare_res[MAX_SL] = 1.0 - new_result.max_slope /
225         prev_best_result.max_slope;
226
227     compare_res[ANG_CH] = fabs(new_result.angle_change) -
228     fabs(prev_best_result.angle_change);
229     if (fabs(prev_best_result.angle_change) < DBL_EPSILON)
230         compare_res[ANG_CH] /= M_PI;
231     else
232         compare_res[ANG_CH] /= fabs(prev_best_result.angle_change);
233

```

```

234     compare_res[SP_S_DIST] = new_result.spot_size_violation_dist -
235     prev_best_result.spot_size_violation_dist;
236     if (fabs(prev_best_result.spot_size_violation_dist) <
237         DBL_EPSILON)
238         compare_res[SP_S_DIST] /= PROPAGATION_DISTANCE;
239     else
240         compare_res[SP_S_DIST] /=
241         prev_best_result.spot_size_violation_dist;
242
243     compare_res[MIN_FL] *= WEIGHTS[MIN_FL];
244     if (new_result.min_flattening > SUFFICIENT_FLATTENING &&
245         prev_best_result.min_flattening > SUFFICIENT_FLATTENING)
246         compare_res[MIN_FL] /= REDUCE_CONST;
247
248     compare_res[MAX_SL] *= WEIGHTS[MAX_SL];
249     if (new_result.max_slope < SUFFICIENT_SLOPE &&
250         prev_best_result.max_slope < SUFFICIENT_SLOPE)
251         compare_res[MAX_SL] /= REDUCE_CONST;
252
253     compare_res[ANG_CH] *= WEIGHTS[ANG_CH];
254     if (fabs(new_result.angle_change) > SUFFICIENT_ANG_CHANGE &&
255         fabs(prev_best_result.angle_change) > SUFFICIENT_ANG_CHANGE)
256         compare_res[ANG_CH] /= REDUCE_CONST;
257
258     compare_res[SP_S_DIST] *= WEIGHTS[SP_S_DIST];
259
260     double res = compare_res[MIN_FL] + compare_res[MAX_SL] +
261                 compare_res[ANG_CH] + compare_res[SP_S_DIST];
262
263     return res > 0;
264 }
265
266 void copy_result(Result &result, const Result &to_copy)
267 {
268     result.angle_change = to_copy.angle_change;
269     result.min_flattening = to_copy.min_flattening;
270     result.max_slope = to_copy.max_slope;
271     result.lens1 = to_copy.lens1;
272     result.lens2 = to_copy.lens2;
273     result.lens2_ang = to_copy.lens2_ang;
274     result.lens2_dist = to_copy.lens2_dist;
275     result.spot_size_violation_dist =
276     to_copy.spot_size_violation_dist;
277 }
278
279 double flattening(double spot_rad_1, double spot_rad_2)
280 {
281     double ratio = spot_rad_2 / spot_rad_1;
282     if (ratio > 1.0)
283         ratio = 1.0 / ratio;
284     return 1.0 - ratio;
285 }
286
287 void get_result_for_lens1_lens2(Beamsplitter lens1, Beamsplitter
288                                lens2, Result &best_result)
289 {

```

```

290     init_result(best_result);
291
292     Result result;
293     result.lens1 = best_result.lens1;
294     result.lens2 = best_result.lens2;
295
296     double current_lens2_position = LENS1_POSITION +
297     lens1.thickness() + LENS1_LENS2_MIN_DISTANCE;
298     double dist_step_size = (LENS1_LENS2_MAX_DISTANCE -
299     LENS1_LENS2_MIN_DISTANCE) / (NUMBER_DISTANCE_STEP - 1);
300
301     double ang_step_size = (LENS2_MAX_ANGLE - LENS2_MIN_ANGLE) /
302     (NUMBER_ANGLE_STEP - 1);
303
304     lens1.set_center_xyz(LENS1_POSITION, 0, 0);
305
306     for (int i = 0; i < NUMBER_DISTANCE_STEP; i++)
307     {
308         lens2.set_center_xyz(current_lens2_position, 0, 0);
309         lens2.set_nv(Direction_3d(-1, 0, 0), Direction_3d(0, 1, 0));
310         double current_lens2_angle = LENS2_MIN_ANGLE;
311         lens2.rotate_3d(X_AXIS, LENS2_MIN_ANGLE);
312         for (int j = 0; j < NUMBER_ANGLE_STEP; j++)
313         {
314             std::cout << std::setw(8) << lens1.name()
315             << std::setw(8) << lens2.name() << std::fixed
316             << std::setw(8) << std::setprecision(1)
317             << current_lens2_position << std::setw(8)
318             << current_lens2_angle / DEGREE;
319
320             result.lens2_ang = current_lens2_angle;
321             result.lens2_dist = current_lens2_position -
322             LENS1_POSITION - lens1.thickness();
323
324             get_result_for_setup(lens1, lens2, result);
325             if (compare_results(result, best_result))
326                 copy_result(best_result, result);
327             current_lens2_angle += ang_step_size;
328             lens2.rotate_3d(X_AXIS, ang_step_size);
329         }
330         current_lens2_position += dist_step_size;
331     }
332 }
333
334 void get_result_for_setup(Beamsplitter &lens1, Beamsplitter &lens2,
335                          Result &result)
336 {
337     GA_GBeam beam;
338     beam.set_origin_xyz(0.0, 0.0, 0.0);
339     beam.set_SA_waist_rad(WAIST_X_RAD, beam.origin().x() -
340     WAIST_X_POS, WAIST_Y_RAD, beam.origin().y() -
341     WAIST_Y_POS, BEAM_ANGLE);
342
343     beam.set_basis(Direction_3d(0, 1, 0));
344     refract_front(lens1, beam);
345     refract_front(lens2, beam);

```

```

346     beam.propagate(CCD_LONG_OFFSET - lens2.thickness());
347
348     double intensity_angle_1 = beam.intensity_angle() + CCD_ANG_OFFSET;
349     double flattening_begin = flattening(beam.spot_rad_1(),
350                                         beam.spot_rad_2());
351
352     std::cout << std::setw(12) << std::fixed << std::setprecision(5)
353     << intensity_angle_1 / DEGREE;
354
355     bool inc;
356     double added;
357     double intensity_angle_2;
358
359     result.min_flattening = flattening_begin;
360     result.max_slope = angle_slope_abs(beam);
361
362     propagate_and_get_results(beam, inc, added, intensity_angle_2,
363     result.spot_size_violation_dist, result.min_flattening,
364     result.max_slope);
365
366     result.angle_change = intensity_angle_2 - intensity_angle_1;
367     std::cout << std::setw(12) << std::setprecision(5)
368     << intensity_angle_2 / DEGREE << std::setprecision(6)
369     << std::setw(12) << added << std::setw(12)
370     << result.angle_change / DEGREE << std::setprecision(4)
371     << std::setw(8) << result.min_flattening << std::setw(8)
372     << result.max_slope << std::setprecision(2)
373     << std::setw(8) << result.spot_size_violation_dist / CM
374     << std::endl;
375 }
376
377 void init_result (Result &result)
378 {
379     result.lens2_ang = 0.0;
380     result.lens2_dist = LENS1_LENS2_MIN_DISTANCE;
381     result.min_flattening = 0.0;
382     result.max_slope = INFINITY;
383     result.angle_change = 0.0;
384     result.spot_size_violation_dist = 0.0;
385 }
386
387 void propagate_and_get_results(GA_GBeam beam, bool &inc,
388 double &added, double &angle, double &spot_size_violation_dist,
389 double &min_flattening, double &max_slope)
390 {
391     double step_size = PROPAGATION_DISTANCE /
392     (NUMBER_PROPAGATION_STEP - 1);
393     std::vector<double> angles;
394     spot_size_violation_dist = PROPAGATION_DISTANCE;
395     bool violated = false;
396     double flatten, slope;
397     for (int i = 0; i < NUMBER_PROPAGATION_STEP; i++)
398     {
399         angles.push_back(beam.intensity_angle() + CCD_ANG_OFFSET);
400         flatten = flattening(beam.spot_rad_1(), beam.spot_rad_2());
401         if (flatten < min_flattening)

```

```

402     min_flattening = flatten;
403     if (!violated)
404         if (beam.spot_rad_1() > MAX_SPOT_RADIUS ||
405             beam.spot_rad_2() > MAX_SPOT_RADIUS)
406             {
407                 spot_size_violation_dist = i * step_size;
408                 violated = true;
409             }
410     slope = angle_slope_abs(beam);
411     if (slope > max_slope)
412         max_slope = slope;
413     beam.propagate(step_size);
414 }
415 added = get_rid_of_phase_jumps(angles, inc);
416 angle = angles[NUMBER_PROPAGATION_STEP - 1];
417 }
418
419 void print_best_result_to_file(const std::string &file_name,
420                             const std::vector<lens> &lens_list, const Result &best_result)
421 {
422     std::ofstream result_file;
423     if (!result_file.good())
424         return;
425     result_file.open(file_name.c_str(), std::fstream::out);
426     if (result_file.fail())
427         return;
428
429     result_file << "# LENSES" << std::endl;
430
431     result_file << "#" << std::setw(19) << "Lens name"
432     << std::setw(15) << "Height [mm]" << std::setw(15)
433     << "Width [mm]" << std::setw(15) << "Thickness [mm]"
434     << std::setw(10) << "f [mm]" << std::setw(5) << "a"
435     << std::setw(12) << "n" << std::endl;
436
437     result_file << std::setw(20)
438     << lens_list[best_result.lens1].name << std::setw(15)
439     << lens_list[best_result.lens1].height << std::setw(15)
440     << lens_list[best_result.lens1].width << std::setw(15)
441     << lens_list[best_result.lens1].thickness << std::setw(10)
442     << lens_list[best_result.lens1].f << std::setw(5)
443     << lens_list[best_result.lens1].a << std::setw(12)
444     << lens_list[best_result.lens1].n << std::endl;
445
446     result_file << std::setw(20)
447     << lens_list[best_result.lens2].name << std::setw(15)
448     << lens_list[best_result.lens2].height << std::setw(15)
449     << lens_list[best_result.lens2].width << std::setw(15)
450     << lens_list[best_result.lens2].thickness << std::setw(10)
451     << lens_list[best_result.lens2].f << std::setw(5)
452     << lens_list[best_result.lens2].a << std::setw(12)
453     << lens_list[best_result.lens2].n << std::endl;
454
455     result_file << std::endl;
456
457     result_file << "#" << std::setw(15) << "Long.Pos. [mm]"

```

```

458     << std::setw(15) << "Angle [deg]" << std::endl;
459
460     result_file << std::setw(16) << LENS1_POSITION << std::setw(15)
461     << 0 << std::endl;
462
463     result_file << std::setw(16) << LENS1_POSITION +
464     lens_list[best_result.lens1].thickness + best_result.lens2_dist
465     << std::setw(15) << best_result.lens2_ang / DEGREE << std::endl;
466
467     result_file << std::endl << "# BEAM" << std::endl;
468
469     result_file << "#" << std::setw(18) << "waist_x [mm]"
470     << std::setw(18) << "waist_pos_x [mm]" << std::setw(18)
471     << "waist_y [mm]" << std::setw(18) << "waist_pos_y [mm]"
472     << std::setw(15) << "angle [deg]" << std::endl;
473
474     result_file << std::setw(19) << WAIST_X_RAD << std::setw(18)
475     << WAIST_X_POS << std::setw(18) << WAIST_Y_RAD << std::setw(18)
476     << WAIST_Y_POS << std::setw(15) << BEAM_ANGLE / DEGREE
477     << std::endl;
478
479     result_file << std::endl << "#" << std::setw(36)
480     << "CCD_long_offset [mm]" << std::setw(36) << "CCD_ang_offset [deg]"
481     << std::endl;
482
483     result_file << std::setw(36) << CCD_LONG_OFFSET << std::setw(36)
484     << CCD_ANG_OFFSET << std::endl;
485
486     result_file.close();
487 }
488
489 int main()
490 {
491     std::vector<lens> lens_list;
492     read_lenses("available_catalog.txt", lens_list);
493
494     Beamsplitter lens1, lens2;
495
496     std::cout << std::setfill(' ') << std::setw(8) << "LENS1"
497     << std::setw(8) << "LENS2" << std::setw(8) << "L2_z"
498     << std::setw(8) << "L2_ang" << std::setw(12) << "b0_ang"
499     << std::setw(12) << "b_end_ang" << std::setw(12) << "phase_jump"
500     << std::setw(12) << "ang_change" << std::setw(8) << "min_fl"
501     << std::setw(8) << "max_sl" << std::setw(8) << "sz_viol"
502     << std::endl;
503
504     Result best_result, result;
505     init_result(best_result);
506
507     for (unsigned int i = 0; i < lens_list.size(); i++)
508     {
509         make_lens(lens_list, i, lens1);
510         for (unsigned j = 0; j < lens_list.size(); j++)
511         {
512             if (lens_list[i].name != lens_list[j].name)
513                 {

```

```

514         make_lens(lens_list , j , lens2);
515         result.lens1 = i;
516         result.lens2 = j;
517         std::cout << "Asymmetry parameters: a1 = "
518         << lens_list[i].a << ", a2 = " << lens_list[j].a
519         << std::endl;
520         get_result_for_lens1_lens2(lens1 , lens2 , result);
521         if (compare_results(result , best_result))
522             copy_result(best_result , result);
523     }
524 }
525 }
526
527 std::cout << "Best result is: " <<
528 lens_list[best_result.lens1].name << " (a = "
529 << lens_list[best_result.lens1].a << ") and "
530 << lens_list[best_result.lens2].name << " (a = "
531 << lens_list[best_result.lens2].a
532 << ") with distance between lenses " << best_result.lens2_dist
533 << " mm, second lens angle " << best_result.lens2_ang / DEGREE
534 << " degree, minimum intensity ellipse flattening over "
535 << PROPAGATION_DISTANCE / CM << " cm "
536 << best_result.min_flattening << ", angle change over "
537 << PROPAGATION_DISTANCE / CM << " cm "
538 << best_result.angle_change / DEGREE
539 << " degree with maximum slope "
540 << best_result.max_slope / DEGREE << " [deg / mm]";
541
542 if (fabs(best_result.spot_size_violation_dist -
543         PROPAGATION_DISTANCE) < DBL_EPSILON)
544     std::cout << ", spot size requirement is not violated over "
545     << PROPAGATION_DISTANCE / CM << " cm " << std::endl;
546 else
547     std::cout << ", spot size requirement is violated at "
548     << best_result.spot_size_violation_dist << " mm"
549     << std::endl;
550
551 print_best_result_to_file("result/best_result.txt", lens_list ,
552                          best_result);
553
554 return 0;
555 }

```

code/cylindrical_lenses.h

```

1 #ifndef CYLINDRICAL_LENSSES_H
2 #define CYLINDRICAL_LENSSES_H
3
4 #include <vector>
5
6 /* IFOCAD files */
7 #include "../source/components/beamsplitter.h"
8
9 //=====lens structure=====
10 struct lens
11 {

```

```

12     std::string name;
13     double height;
14     double width;
15     double thickness;
16     double a;           // Asymmetry parameter
17     double f;           // focal length
18     double n;           // Refractive index
19 };
20 //=====Function declarations=====
21 /**
22  * Constructs a list of lenses from catalog. If lens is not
23  * symmetric ( $a < 0$ , for example for plano-convex lenses), it is
24  * added twice (with  $a$  and  $-a$ ).
25  */
26 void read_lenses(const std::string &file_name, std::vector<lens>
27                 &lens_list);
28 /**
29  * Creates an object of Beamsplitter class from the  $i$ -element of a
30  * lens_list.
31  */
32 void make_lens(const std::vector<lens> &lens_list, int i,
33               Beamsplitter &new_lens);
34 //=====
35 #endif // CYLINDRICAL_LENSES_H

```

code/cylindrical_lenses.cpp

```

1 #include "cylindrical_lenses.h"
2
3 #include <fstream>
4
5 void read_lenses(const std::string &file_name, std::vector<lens>
6                 &lens_list)
7 {
8     std::ifstream linos_file;
9     if (!linos_file.good())
10        return;
11     linos_file.open(file_name.c_str(), std::fstream::in);
12     if (linos_file.fail())
13        return;
14     std::string line;
15     size_t line_count = 0, lens_count = 0;
16     lens current_lens;
17     while (!linos_file.eof())
18     {
19         std::getline(linos_file, line);
20         if (line.empty() || line[0] == '#')
21             continue;
22         std::stringstream ss(line, std::stringstream::in);
23         ss >> current_lens.name >> current_lens.height
24         >> current_lens.width >> current_lens.thickness
25         >> current_lens.f >> current_lens.a >> current_lens.n;
26         if (!ss.good())
27             continue;
28         ++line_count;
29         lens_list.push_back(current_lens);

```



```

30     ++lens_count;
31     if (current_lens.a)
32     {
33         current_lens.a = -current_lens.a;
34         lens_list.push_back(current_lens);
35         ++lens_count;
36     }
37 }
38 }
39
40 void make_lens(const std::vector<lens> &lens_list, int i,
41              Beamsplitter &new_lens)
42 {
43     new_lens.set_size(lens_list[i].width, lens_list[i].height);
44     new_lens.set_thickness(lens_list[i].thickness);
45     Material m;
46     m.set_n(lens_list[i].n);
47     new_lens.set_substrate(m);
48     new_lens.set_focal_length(lens_list[i].f, lens_list[i].a,
49                             CYLINDRICAL_LENS);
50     new_lens.set_name(lens_list[i].name);
51 }

```

code/phase_jumps.h

```

1  #ifndef PHASE_JUMPS_H
2  #define PHASE_JUMPS_H
3
4  #include <vector>
5
6  //=====Function declarations=====
7  /**
8   * Returns true if elements in the array are mostly in "increasing"
9   * order, false for "decreasing"
10  */
11 bool increasing(const std::vector<double> &angles);
12 /**
13  * Gets rid of the "phase jumps" - places in array, where major
14  * order (increasing or decreasing) is changed to the opposite.
15  * Therefore adds or subtracts PI/2 for all elements, starting with
16  * the one that brakes the order. Returns the biggest value that was
17  * added or subtracted from the elements of array (for phase ellipse
18  * and intensity ellipse angles shouldn't be more than +/- PI)
19  */
20 double get_rid_of_phase_jumps(std::vector<double> &angles,
21                              bool &inc);
22 double get_rid_of_phase_jumps(std::vector<double> &angles);
23
24 //=====Implementation=====
25
26 bool increasing(const std::vector<double> &angles)
27 {
28     bool inc = true;
29     int increasing_count = 0;
30     int decreasing_count = 0;
31     for (unsigned int i = 0; i < angles.size() - 1; i++)

```

```

32     {
33         if (angles[i] < angles[i + 1])
34             increasing_count += 1;
35         else
36             decreasing_count += 1;
37     }
38     inc = increasing_count > decreasing_count;
39     return inc;
40 }
41
42 double get_rid_of_phase_jumps(std::vector<double> &angles,
43                               bool &inc)
44 {
45     inc = increasing(angles);
46     double added = 0;
47     double to_add = 0;
48     for (unsigned int i = 0; i < angles.size() - 1; i++)
49     {
50         if (inc && (angles[i + 1] < angles[i]) &&
51             fabs(angles[i + 1] - angles[i]) > 1e-10)
52         {
53             to_add = M_PI / 2.0;
54             added += M_PI / 2.0;
55         }
56         if ((!inc) && (angles[i + 1] > angles[i]) &&
57             fabs(angles[i + 1] - angles[i]) > 1e-10)
58         {
59             to_add = -M_PI / 2.0;
60             added -= M_PI / 2.0;
61         }
62         if (fabs(to_add) > DBL_EPSILON)
63         {
64             for (unsigned int j = i + 1; j < angles.size(); j++)
65                 angles[j] += to_add;
66             to_add = 0.0;
67         }
68     }
69     return added;
70 }
71
72 double get_rid_of_phase_jumps(std::vector<double> &angles)
73 {
74     bool inc;
75     return get_rid_of_phase_jumps(angles, inc);
76 }
77
78 #endif // PHASE_JUMPS_H

```

- ABCD-law, 33
- Accumulated optical pathlength, 22
- Accumulated phase, 22
- Angle of orientation
 - intensity ellipse, 45, 46
 - phase ellipse, 45, 46
- Angular frequency
 - beam, 9
 - heterodyne, 9
- Asymmetry parameter, 60
- Beam
 - measurement, 8
 - power, 8
 - propagation factor, 59
 - radius, 20, 30, 46
 - reference, 8
- Beam tracing, 5, 6
- CCD camera, 63
- Complex amplitude
 - of electric field, 9
 - general astigmatic Gaussian beam, 40
 - simple astigmatic Gaussian beam, 28
 - stigmatic Gaussian beam, 18
 - of heterodyne power, 11
- Complex envelope, 18, 28
- Complex phase, 33, 44
- Complex radius of curvature tensor, 41
- Coordinate system
 - beam principal, 6, 29
 - beam-fixed, 6
- Coordinate transformation matrix, 54
- Curvature matrix of a surface, 52
- Cylindrical lens, 60
- Divergence, 21
- Electric field, 9
- Ellipticity, 78
- Euler-Poisson integral, 29
- Flattening, 78
- Gaussian beam in fundamental mode,
 - 2
 - general astigmatic, 2, 39
 - simple astigmatic, 2, 27
 - stigmatic (circular), 2, 17
- Gouy phase shift
 - general astigmatic Gaussian beam, 41
 - jumps, 23
 - simple astigmatic Gaussian beam, 28
 - stigmatic Gaussian beam, 22
- Helmholz equation, 18

- paraxial, 18
- Imaging optics, 94
- Impedance of the medium, 9
- Intensity ellipse matrix, 44
- Interferometer
 - heterodyne, 8, 12
 - homodyne, 8, 13
- Interferometer signals, 8
 - contrast, 5, 10, 11, 13
 - differential power sensing (DPS), 5, 12
 - differential wavefront sensing (DWS), 5, 12
 - longitudinal pathlength (LPS), 5, 11, 12, 97
- Lensmaker's equation, 60
- LISA mission, 2
 - optical bench (LISA OB), 2
- Optical intensity, 8
 - contrast, 10
 - general astigmatic Gaussian beam, 44
 - mean, 10
 - simple astigmatic Gaussian beam, 30
 - stigmatic Gaussian beam, 20
- Optical system
 - non-orthogonal, 14
 - orthogonal, 14, 27, 35
 - rotationally symmetric, 14, 17
- Phase
 - general astigmatic Gaussian beam, 44
 - simple astigmatic Gaussian beam, 30
 - stigmatic Gaussian beam, 22
- Phase ellipse matrix, 44
- Photocurrent, 8
- Photodiode
 - quadrant (QPD), 5, 8, 12
 - responsivity, 8
 - single element (SEPD), 8, 11
- Plane of incidence, 3
- Power
 - mean, 10, 11
 - sensed, 8, 10
- Propagation
 - general astigmatic Gaussian beam, 43
 - simple astigmatic Gaussian beam, 31
 - stigmatic Gaussian beam, 24
- q-parameter, 19, 28
- Radius of curvature of wavefront, 23, 30, 47
- Ray, 6
- Rayleigh range, 20
- Reflection law, 7
 - general astigmatic Gaussian beam, 50
 - simple astigmatic Gaussian beam, 36
 - stigmatic Gaussian beam, 25
- Refraction law, 7
 - general astigmatic Gaussian beam, 50
 - simple astigmatic Gaussian beam, 37
 - stigmatic Gaussian beam, 25
- Rotation matrix, 41
- Snell's law, 7
- Spot radius, 20, 30, 46
- Waist, 20

Bibliography

- [1] A. Maria, “Introduction to modelling and simulation,” in *Proceedings of the 1997 Winter Simulation Conference*, 1997, pp. 7–13. doi:10.1109/WSC.1997.640371
- [2] R. McHaney, *Understanding computer simulation*. Ventus Publishing ApS, 2009. <http://bookboon.com/en/textbooks/it-programming/understanding>
- [3] G. Petrone and G. Cammarata, *Modelling and simulation*. I-Tech Education and Publishing, 2008. doi:10.5772/79
- [4] V. Ferrari, J. Miller, and L. Rezzolla, Eds., *Gravitational Waves: A Challenge to Theoretical Astrophysics*, ser. ICTP Lecture Notes Series, vol. 3, May 2001.
- [5] LISA International Science Team, “LISA. Unveiling a hidden Universe,” European Space Agency, Tech. Rep., Feb. 2011. <http://sci.esa.int/science-e/www/object/index.cfm?fobjectid=48364>
- [6] G. Wanner, “Complex optical systems in space: numerical modelling of the heterodyne interferometry of LISA Pathfinder and LISA,” Ph.D. dissertation, Leibniz Universität Hannover, 2010. <http://edok01.tib.uni-hannover.de/edoks/e01dh11/660137038.pdf>
- [7] J. Alda, “Laser and Gaussian beam propagation and transformation,” in *Encyclopedia of Optical Engineering*. Marcel Dekker, 2003, pp. 999–1013.
- [8] J. A. Arnaud and H. Kogelnik, “Gaussian light beams with general astigmatism,” *Applied Optics*, vol. 8, no. 8, pp. 1687–1694, Aug. 1969. doi:10.1364/AO.8.001687
- [9] G. A. Massey and A. E. Siegman, “Reflection and refraction of gaussian light beams at tilted ellipsoidal surfaces,” *Applied Optics*, vol. 8, no. 5, pp. 975–978, May 1969.

- [10] “OptoCad: Tracing Gaussian TEM00 beams through an optical set-up,” <http://home.rzg.mpg.de/~ros/optocad.html>.
- [11] A. Rohani, A. A. Shishegar, and S. Safavi-Naeini, “A fast Gaussian beam tracing method for reflection and refraction of general vectorial astigmatic Gaussian beams from general curved surfaces,” *Optics Communications*, vol. 232, pp. 1–10, Mar. 2004. doi:10.1016/j.optcom.2003.11.044
- [12] G. Heinzel, V. Wand, A. Garcia, O. Jennrich, C. Braxmaier, D. Robertson, K. Middleton, D. Hoyland, A. Rüdiger, R. Schilling, U. Johann, and K. Danzmann, “The LTP interferometer and phasemeter,” *Classical and Quantum Gravity*, vol. 21, no. 5, pp. S581–S587, Mar. 2004. doi:10.1088/0264-9381/21/5/029
- [13] D. Schaddock, B. Ware, P. Halverson, and B. Klipstein, “Overview of the LISA Phasemeter,” in *Laser Interferometer Space Antenna*, ser. AIP Conference Proceedings, vol. 873, 2006, pp. 654–660.
- [14] I. Bykov, J. J. E. Delgado, A. F. G. Marin, G. Heinzel, and K. Danzmann, “LISA phasemeter development: advanced prototyping,” in *Journal of Physics: Conference Series*, vol. 154, 2009. doi:10.1088/1742-6596/154/1/012017
- [15] E. Morrison, B. J. Meers, D. I. Robertson, and H. Ward, “Automatic alignment of optical inteferometers,” *Applied Optics*, vol. 33, no. 22, pp. 5041–5049, Aug. 1994.
- [16] E. Hecht, *Optics*, 3rd ed. Addison Wesley Longman, Inc., 1998.
- [17] B. E. A. Saleh and M. C. Teich, *Fundamentals of Photonics*, 2nd ed. John Wiley & Sons, Inc, 2007.
- [18] H. Kogelnik and T. Li, “Laser beams and resonators,” *Applied Optics*, vol. 5, no. 10, pp. 1550–1567, Oct. 1966. doi:10.1364/AO.5.001550
- [19] J. Alda, S. Wang, and E. Bernabeu, “Analytical expression for the complex radius of curvature tensor Q for generalized gaussian beams,” *Optics Communications*, vol. 80, no. 5, 6, pp. 350–352, Jan. 1991. doi:10.1016/0030-4018(91)90421-9
- [20] A. E. Siegman, *Lasers*. University Science Books, 1986.
- [21] G. Heinzel, *IFOCAD: A framework of C subroutines to plan and optimize the geometry of laser interferometers*, Space interferometry Group, AEI Hannover, 2012, <http://www.lisa.aei-hannover.de/ifocad/>.
- [22] J. Alda, D. Vazquez, and E. Bernabeu, “Wavefront and amplitude profile for astigmatic beams in semiconductor lasers: analytical and graphical treatment,” *Journal of optics (Paris)*, vol. 19, no. 5, 6, pp. 201–206, 1988. doi:10.1088/0150-536X/19/5-6/002
- [23] R. K. Luneberg, *Mathematical theory of optics*. University of California press, Berkeley and Los Angeles, 1964.

-
- [24] A. Rohani, “A fast hybrid method based on a Gaussian beam tracing scheme for photonic structures,” Master’s thesis, University of Waterloo, Waterloo, Ontario, Canada, 2002.
- [25] A. Rohani, “A fast hybrid method for analysis and design of photonic structures,” Ph.D. dissertation, University of Waterloo, Waterloo, Ontario, Canada, 2006. <http://etd.uwaterloo.ca/etd/aroahani2006.pdf>
- [26] A. B. Plachenov, V. N. Kudashov, and A. M. Radin, “Simple formula for a Gaussian beam with general astigmatism in a homogeneous medium,” *Physical Optics*, vol. 106, no. 6, pp. 910–912, 2009. doi:10.1134/S0030400X09060204
- [27] J. Serna and G. Nemes, “Decoupling of coherent Gaussian beams with general astigmatism,” *Optics Letters*, vol. 18, no. 21, pp. 1774–1776, Nov. 1993. doi:10.1364/OL.18.001774
- [28] G. A. Deschamps, “Ray techniques in electromagnetics,” in *Proceedings of the IEEE*, vol. 60, no. 9, Sep. 1972, pp. 1022–1035, invited paper. doi:10.1109/PROC.1972.8850
- [29] G. J. James, *Geometrical theory of diffraction for electromagnetic waves*, 3rd ed. Peter Peregrinus Ltd., 1986.
- [30] D. Schmelzer, “Experimental investigation of general astigmatic Gaussian beams and comparison to simulation,” bachelor thesis, Leibniz Universität Hannover, 2012.
- [31] “Coherent,” <http://www.coherent.com>.
- [32] “Schäfter und Kirchhoff,” <http://www.sukhamburg.com>.
- [33] “Dataray,” <http://www.dataray.com>.
- [34] N. Hodgson and H. Weber, *Optical resonators. Fundamentals, advanced concepts and applications*. Springer, 1997.
- [35] J. Primot, “Theoretical description of Shack-Hartmann wave-front sensor,” *Optics Communications*, vol. 222, pp. 81–92, Jul. 2003. doi:10.1016/S0030-4018(03)01565-7
- [36] “Qioptiq,” <http://www.qioptiq.com/>.
- [37] “Sill Optics,” <http://www.silloptics.de/>.
- [38] T. Möller and J. F. Hughes, “Efficiently building a matrix to rotate one vector to another,” *Journal of graphics tools*, vol. 4, no. 4, 2000. <http://cs.brown.edu/~jfh/papers/Moller-EBA-1999/paper.pdf>

- P1** L. d’Arcio, J. Bogenstahl, M. Dehne, C. Diekmann, E. D. Fitzsimons, R. Fleddermann, **E. Granova**, G. Heinzl, H. Hogenhuis, C. J. Killow, M. Perreur-Lloyd, J. Pijenburg, D. I. Robertson, A. Shoda, A. Sohmer, A. Taylor, M. Tröbs, G. Wanner, H. Ward, and D. Weise, **Optical bench development for LISA**, *ICSO conference series*, (2010)
- P2** G. Wanner, G. Heinzl, **E. Kochkina**, C. Mahrtdt, B. Sheard, S. Schuster, K. Danzmann, **Methods for simulating the readout of lengths and angles in laser interferometers with Gaussian beams**, *Optics Communications*, (2012), doi:10.1016/j.optcom.2012.07.123
- P3** M. Tröbs, L. d’Arcio, S. Barke, J. Bogenstahl, I. Bykov, M. Dehne, C. Diekmann, E. D. Fitzsimons, R. Fleddermann, O. Gerberding, J.-S. Hennig, F. G. Hey, H. Hogenhuis, C. J. Killow, **E. Kochkina**, J. Kullmann, M. Lieser, S. Lucarelli, M. Perreur-Lloyd, J. Pijenburg, D. I. Robertson, A. Shoda, A. Sohmer, A. Taylor, G. Wanner, H. Ward, D. Weise, G. Heinzl, K. Danzmann, **Testing the LISA optical bench**, *ICSO conference series*, (2012)
- P4** **E. Kochkina**, G. Heinzl, G. Wanner, V. Müller, C. Mahrtdt, B. Sheard, S. Schuster, K. Danzmann, **Simulating and optimizing laser interferometers**, *9th LISA Symposium, Paris ASP Conference Series*, Vol. 467, (2013), <http://www.apc.univ-paris7.fr/~beckmann/Proceedings/Kochkina.pdf>
- P5** **E. Kochkina**, G. Wanner, D. Schmelzer, M. Tröbs, G. Heinzl, **Modeling of the general astigmatic Gaussian beam and its propagation through 3D optical systems**, submitted to *Applied Optics*

- PD1** M. Tröbs, J. Bogenstahl, M. Dehne, C. Diekmann, **E. Granova**, A. Shoda, G. Wanner, G. Heinzl, **Test of interferometry concept**, LOB-AEI-TN-005.1, Issue 1.3 (April 20, 2011)
- PD2** J. Bogenstahl, C. Diekmann, **E. Granova**, T. Schwarze, M. Tröbs, G. Wanner, **Optical Bench EBB Design Definition File – Opto-Electronics & Alternative Beam Compressors**, LOB-AEI-TN-008.1-08, Issue 0.8 (June 29, 2011)
- PD3** J. Burkhardt, M. Kersten, T. Villegeorges, D. Weise, **Analyses and Specifications for OB Detailed Design**, LOB-TN-007-05-ASD, Issue 0.5 (Sept 14, 2011)

Curriculum Vitae

Personal Details

Name: Evgenia Kochkina, née Granova
Nationality: Russian Federation
Date of birth: 10th of May 1987
Place of birth: Voronezh (USSR)
Family status: Married, no children

University Education

01/2010 - present Doctoral studies in Physics, Albert Einstein Institute (AEI),
Hannover.
09/2004 - 07/2009 Applied Mathematics, Informatics and Mechanics studies,
Voronezh State University.
Graduated with diploma.

Education

09/2001 - 06/2004 Gymnasium Named After Basov, Voronezh.
*Graduated with certificate of (complete) secondary general
education.*
09/1993 - 06/2001 School 30, Voronezh.

Working experience

09/2008 - 11/2009 Software engineer in Radix-Tools Inc., Voronezh.